THE EVOLUTION OF ENERGETIC PARTICLES AND THE EMITTED RADIATION IN SOLAR FLARES

EDWARD TSANG LU

NSG·
~~[illegible]~~ -7092

CSSA-ASTRO-89-08
June 1989

A Dissertation Submitted to the Department of Applied Physics
and the Committee on Graduate Studies of Stanford University
in Partial Fulfillment of the Requirements for the Degree of
Doctor of Philosophy

National Aeronautics and Space Administration Grant NSG 7092
National Science Foundation Grant ATM 8705084

The Evolution of Energetic Particles and the Emitted Radiation in Solar Flares

The evolution of accelerated particle distributions in a magnetized plasma and the resulting radiation are calculated, and the results are applied to solar flares. To study the radiation on timescales of order the particle lifetimes, the evolution of the particle distribution is determined by use of the Fokker-Planck equation including Coulomb collisions and magnetic mirroring. Analytic solutions to the equation are obtained for limiting cases such as homogeneous injection in a homogeneous plasma, and for small pitch angle. These analytic solutions are then used to place constraints on flare parameters such as density, loop length, and the injection timescale for very short impulsive solar flares. For general particle distributions in arbitrary magnetic field and background density, the equation is solved numerically. Over longer timescales, the variation with X-ray spectral index of the observed ratio of microwave to hard X-ray peak fluxes is shown to be consistent with the nonthermal thick target beam model, while multithermal and thin target models have difficulty matching the observations. The relative timing of microwaves and X-rays during individual flares is then investigated. The observation that the microwaves are observed to peak ~ 2 s later than hard X-rays is interpreted as being due to an excess of microwave flux above that predicted by the simple thick target model. We discuss a number of possible sources for this excess microwave flux including a flattening in the electron spectrum above hard X-ray energies, thermal synchrotron emission, and trapping of electrons by converging magnetic field. Over shorter timescales, the Fokker-Planck equation is solved numerically to calculate the temporal evolution of microwaves and X-rays from nonthermal thick target models. It is shown that magnetic trapping will not account for the observed correlation of microwaves $\sim .25$ seconds behind X-rays in flares with rapid time variation, and thus higher energy electrons must be accelerated later than lower energy electrons.

II III

ACKNOWLEDGEMENTS

This thesis describes work done from 1984 to 1989 at Stanford University in collaboration with Vahé Petrosian. The work described in chapters 2 and 4 was also done in collaboration with Russell Hamilton. This thesis of course would not have been possible were it not for a number of people including:

my family: Mom, Dad, Lisa and Rick

my thesis advisor: Vahé Petrosian

my cohorts: Russ Hamilton and Jim McTiernan

our boss: Mary Oshima

our funding: NASA grant NSG7092 and NSF grant ATM8705084

This thesis has been possible both because of and in spite of a number of other people including (in no particular order):

Doug, Paul, Jeanne, Don, Kianoosh, Derrick, Rahim, Tony, Dave, Jim, Louise, Lynn, Nicole, Siobhan, Salman, Ann, Peter, Art, Bob, Gethyn, Dave, Julie, Jeff, Marc, Lizzo, Leo, Joaana, Melanie, Claudio, Jeff, Todd, Rick, Leslie, Sarah, Phil, Dave, Dave, Lynn, Kathy, Susan, Joakim, Ray, Taeil, Peter, Amri, Jeff, Russ, Rich, Carrie, Betty, Lynn, Klaus, Dieter, Rick, Jordan, the Jerks, Anita, Holly, Elaina, Cindy, Amy, Tom, Randy, Susie, John, Scott, Dave, Mary, Dave, Bud, Emmy, the Palo Alto Flying Club, Kevin, Laura, Janet, John, Carmen, Jeff, Susanne, the Gunn High School wrestling team, Christina, Raji, Saroja, Heidi, Jan, Matt, Johnny, Hillary, Karen, Chris, Ann, Jibran, Ghassan, Hong, Glenn, Judy, Audrey, George, Ashley, Don, Jim, Marc, Bob, Dana, Chris, Molly, Keith, Greg, Tamara, John, Eve, Elise, Monica, Dallas, Andy, Yan Ling, John, Holly, Mike, Bernard, Ed, Tom, Julia, Steve, Bill, Misa, Greg, Lynn, Mark, Jim, Mike, Diane, Ed, Nick, Paula, and everyone else.

TABLE OF CONTENTS

CHAPTER 1. INTRODUCTION

The general goal of this research is to see what can be learned about astrophysical objects from the time dependence of their emission. Many astrophysical objects display transient behavior and as we shall see, much information is contained in the temporal structure of the emitted radiation. Such a study is particularly warranted in light of the development of new detectors with higher time resolution.

The general problem which must be addressed is how a distribution of accelerated particles evolves in a magnetized plasma, and given that, how the resulting radiation signature evolves. The situation of a magnetized plasma with a nonthermal population of energetic particles is very common in astrophysics, occuring in such diverse areas as solar flares, cosmic rays, astrophysical jets, neutron star atmospheres, planetary and stellar magnetospheres etc.

This thesis will concentrate on the temporal evolution of the emission from solar flares, since there is a large amount of observational data with good time resolution. Solar flares are large, explosive releases of energy on the surface of the sun. The total energy released in a large flare can be greater than 10^{32} ergs, a large fraction of which is in the form of energetic particles. Electrons and protons can be accelerated to energies exceeding 10 MeV and 1 GeV respectively. Solar flares have been observed for over a century, and although much is known about them, the detailed physics is still not well understood (see the review article by Dennis, 1988). Among the principle goals of solar flare research is the understanding of the acceleration mechanism. Since it is impossible to make in-situ measurements of the accelerated particle distribution, we must rely on observations of the radiation emitted by the accelerated particles or on the few particles which escape to the vicinity of the Earth. One avenue which offers hope of providing a greater understanding of flares is the study of the time dependence of the emission. Flare emission is observed to vary over timescales ranging from $\lesssim 100$ ms to hours. This thesis will be concerned mainly with the microwave and hard X-ray emission from flares, because they provide the most direct diagnostics of the electrons with energies from ~ 25 keV to ~ 1 MeV, which constitute the majority of the energy budget in accelerated particles. In addition, there is a large amount of data available in X-rays and microwaves with high time resolution (see e.g. Kiplinger et al 1983, Kaufmann et al 1983).

It is generally agreed that the bulk of the hard x-ray emission from the impulsive phase of solar flares is due to thick target bremsstrahlung emission from non-thermal electrons. In these models, electrons are accelerated in the corona and stream downwards along magnetic field lines towards the chromosphere where they lose most of their energy through Coulomb collisions with the background plasma particles. The microwave emission on the other hand is due to synchrotron emission by the energetic electrons in the magnetic field structure of the flare. Until recently, the time resolution of observing instruments has been longer than the typical interaction timescale of the electrons. Short timescale variations were therefore lost in the time integration of the instruments. Consequently, most of the previous calculations of flare emission have assumed steady state conditions (e.g. Brown 1973, Leach and Petrosian 1981, McTiernan and Petrosian 1989). In order to study the emission on such timescales of order the particle propagation and collisional times, we must be able to describe the evolution of the particle distribution due to its interaction with the background plasma.

In the limit where the change in particle momentum due to individual scatterings is small compared to the particle momentum, the evolution of the particle distribution can be described by a Fokker-Planck equation. The form of this equation is described in chapter 2. We will use the Fokker-Planck equation to calculate the distribution of nonthermal electrons in a magnetized plasma, and from this determine the bremsstrahlung and synchrotron emission.

In chapter 3, analytic solutions to the Fokker-Planck equation are derived. These solutions are however only valid in the limiting cases of constant plasma density, or beams of particles moving nearly parallel to the magnetic field. We apply these solutions to the study of very short timescale X-ray bursts from flares. These bursts show spectral softening on timescales of tenths of a second which is of order the propagation time for electrons in a magnetic loop.

In order to describe the evolution of an electron distribution with electrons moving at large pitch angles in an arbitrary magnetic field and plasma density distribution, we must turn to a numerical solution. In chapter 4 we outline the numerical solution of the Fokker-Planck equation. We will use this numerical code in chapter 6 to study the relative timing of microwaves and X-rays on timescales ~ 0.1 s.

We then turn our attention to the relative strengths of the microwave and X-ray emission. Over timescales $\gtrsim 1$ s which is larger than the collisional and propagation times, we need not solve the time dependent kinetic equation, but can instead rely upon steady state relations. In chapter 5, we derive relations for the steady state emission of microwaves and X-rays from flares, and place constraints upon the geometry of the flaring region based upon a statistical study of the peak microwave and X-ray emission from flares. These analytic relations will also be used in chapter 6 to describe the evolution of X-ray and microwave emission during individual flares on timescales of order 1 s. We show that the most likely model for X-ray and microwave emission is the nonthermal thick target model.

However, one observation which does not seem to agree with the simplest form of this model is the relative timing of the microwave and hard X-ray radiation. Although the microwaves and hard X-rays exhibit a very similar time structure, indicating a common origin for both, the microwave time profile seems to lag behind the X-ray time profile for most impulsive flares. In chapter 6 we use the steady state relations developed in chapter 5 along with the numerical code described in chapter 4 to study the relative timing of microwaves and X-rays over timescales ranging from tenths of a second to several seconds. From this we place constraints upon various solar flare physical parameters and on the acceleration mechanism responsible for solar flares. Chapter 7 provides a summary.

CHAPTER 2. THE FOKKER-PLANCK EQUATION

In this chapter we describe the Fokker-Planck equation for the transport and evolution of particles in a magnetized plasma. From the solutions to this equation the evolution of the emitted bremmstrahlung and synchrotron radiation can be calculated. Some of the physical processes which affect the particle distribution are magnetic mirroring, Coulomb scattering, wave-particle interactions, synchrotron emission, and direct electric fields. The physical parameters of the plasma such as density and magnetic field strength, and the energy of the particles determine which of these mechanisms need be considered (see e.g. Harding, Petrosian, and Teegarden 1986, Table 2.1). Some areas which could be studied using this method include evolution of radiation spectra from solar flares, development of plasma instabilities, and particle acceleration (both stochastic and direct). In this chapter, we give the general form of the Fokker-Planck equation and the relevent coefficients for the above mentioned processes. Analytic and numerical solutions to this equation for a distribution of electrons evolving in a magnetized plasma including just Coulomb collisions and magnetic mirroring are presented in chapters 3 and 4.

2.1 The Equation

In many astrophysical plasmas, the gyroradius of the particles about the magnetic field is many orders of magnitude less than other length scales in the problem. Thus, the charged particles are essentially tied to the magnetic field lines so that only one spatial variable giving the position along the field line is needed. The distribution function in momentum space can then be specified by two independent components of momentum, or equivalently by the energy and the cosine of the pitch angle of the particle with respect to the magnetic field. The particle distribution function $f(E, \mu, s, t)$ is then a function of four variables, the particle kinetic energy E in units of mc^2, the pitch angle cosine μ, the position

s, and the time t. In the limit where the change in particle momentum due to individual scatterings is much less than the original momentum, we can make use of the Fokker-Planck expansion of the Boltzmann collision integral in the continuity equation for f (see e.g. Lifshitz and Pitaevskii 1981). The Fokker-Planck equation can be written in the form

$$\begin{aligned} 0 =& \frac{\partial f}{\partial t} + \mu c\beta \frac{\partial f}{\partial s} + \frac{\partial}{\partial \mu}(\dot{\mu} f) + \frac{\partial}{\partial E}(\dot{E} f) - \frac{\partial}{\partial \mu}(D_{\mu\mu}\frac{\partial f}{\partial \mu}) - \frac{\partial}{\partial E}(D_{EE}\frac{\partial f}{\partial E}) - \\ & \frac{\partial}{\partial E}(D_{E\mu}\frac{\partial f}{\partial \mu}) - \frac{\partial}{\partial \mu}(D_{E\mu}\frac{\partial f}{\partial E}) + S(E,\mu,s,t) \end{aligned} \tag{2.1}$$

where $S(E,\mu,s,t)$ is a source term. The coefficients $\dot{E}$ and $\dot{\mu}$ are the systematic changes in energy and pitch angle cosine due to external forces, radiation, and scattering while the diffusion coefficients D arise only due to scattering processes. Note that D is defined differently than the usual Fokker-Planck coefficients.

In this section we give the forms of $\dot{E}$, $\dot{\mu}$, and D for electrons under the influence of Coulomb collisions, plasma wave scattering, synchrotron radiation, magnetic field variation, and external forces. These terms are summarized in Tables 2.1 and 2.2. Note that all of these terms in some form have been published elsewhere. We give them here simply as a useful reference.

Coulomb Collisions: We assume the background plasma to be fully ionized hydrogen with $kT/mc^2 \ll E$. Here $\ln\Lambda \approx 20$ is the Coulomb logarithm, n is the background particle density, and r_0 is the classical electron radius. Leach and Petrosian (1981), and McTiernan and Petrosian (1989) discuss the effect other plasma compositions and of partially ionized plasmas. The D_{EE} and $D_{E\mu}$ terms are missing because we assume the background plasma to be cold, so that there is no upscattering in energy.

Bremsstrahlung: For bremsstrahlung emission, the energy of the emitted photons is often of order the energy of the electrons, so that the change in particle momentum in individual scatterings is comparable to the original momentum.

The Fokker-Planck equation is not valid in this case (Blumenthal and Gould 1970). Instead one must use the full Boltzmann equation to describe such a situation. However, the ratio of bremsstrahlung to Coulomb energy loss rates is $\dot{E}_{\mathrm{brem}}/\dot{E}_{\mathrm{Coul}} \approx 10^{-4}(\ln\Lambda/20)EZ_i$, where Z_i is the charge of the ions in the plasma. In a hydrogen plasma this ratio is less than unity for $E \lesssim 10^3$. For such energies, however, processes which do not conserve particle number, such as pair creation, also become important so that equation (1) is no longer valid. We therefore limit our discussion to $E \ll 10^3$ and ignore the bremmstrahlung process.

Magnetic Mirroring: This term arises due to inhomogeneities in the magnetic field B and is calculated using the adiabatic invariance of flux through particle orbits (see e.g. Leach and Petrosian 1981).

Synchrotron: Here we assume classical synchrotron emission so that there are no diffusion terms (see e.g. Petrosian 1985).

Inverse Compton: Inverse Compton scattering is qualitatively similar to synchrotron emission since synchrotron emission is just scattering off the virtual photons of the magnetic field. Apart from geometric factors of order unity and factors involving μ, the ratio of energy loss rates due to inverse Compton scattering to that due to synchrotron radiation is equal to the ratio of the photon energy density to the magnetic field energy density $B^2/8\pi$ (see e.g. Melrose 1980). The inverse Compton pitch angle diffusion coefficients do not have a simple pitch angle dependence, but have energy dependence similar to that of synchrotron emission.

External Forces: An example of an external force is a direct electric field. Since we assume the electrons to be tied to the field lines, only the component of the force parallel to the magnetic field $F_{\|}$ need be considered. We ignore cross field diffusion due to the perpendicular component of the force.

Plasma Turbulence: The diffusion rates due to the scattering by Alfvén waves (magnetic fluctuations) and Langmuir waves (electrostatic fluctuations) are given in the tables. We do not consider the generation of these waves, but relate the changes in the distribution to the spectrum of turbulence present in the plasma. We do not give the rates from scattering off of other plasma waves such as whistlers. We note, however, that the diffusion coefficients for whistlers have the same energy and pitch angle dependence as the Alfvén wave terms to first order in the phase velocity of the wave divided by the particle velocity. The rates tabulated for Alfvén wave turbulence are those found by Schlickeiser (1989a, 1989b) for a cold plasma. Here $I^L(k)dk$ and $I^R(k)dk$ are the energy densities in left and right hand circularly polarized Alfvén waves in wave number interval dk. An important aspect of the interaction with Alfvén waves is that the ratio of the coefficients $D_{\mu\mu} : D_{E\mu} : D_{EE}$ is (ignoring phase space factors) $1 : v_A/v : v_A^2/v^2$ where v is the particle velocity and v_A is the Alfvén velocity. Thus, for $v_A << v$ the pitch angle diffusion is very much larger than diffusion in energy.

The expressions given for Langmuir turbulence assume an isotropic spectrum of waves. Here $W(k)d^3k$ is the differential energy density in Langmuir turbulence and ε_L is the total energy density with wave number greater than $\omega_p/c\beta$. For relativistic and mildly relativistic electrons, diffusion in energy is much larger than diffusion in pitch angle. This can lead to stochastic acceleration of the electrons when high levels of turbulence exist in the plasma.

An important physical situation of interest is the propagation and evolution of a distribution of accelerated electrons injected into a region of varying density and magnetic field, such as a solar flare loop, and undergoing magnetic mirroring and Coulomb collisions. These are the dominant processes for electrons of energy ~ 10 keV to ~ 1 MeV, under typical solar flare conditions of magnetic field strength ~ 100 to ~ 1000 Gauss, and plasma densities $\sim 10^9$ to $\sim 10^{14}$ cm^{-3}. In this case, we find for the Fokker-Planck equation (see Leach 1984, Lu and Petrosian 1988)

$$\begin{aligned}\frac{\lambda_0}{c\beta}\frac{\partial f}{\partial t} = & -\lambda_0 \mu \frac{\partial f}{\partial s} + \lambda_0 \frac{d \ln B}{ds}\frac{\partial}{\partial \mu}\left(\frac{(1-\mu^2)}{2} f\right) + \frac{1}{\beta}\frac{\partial}{\partial E}\left(\frac{f}{\beta}\right) + \\ & \frac{1}{\beta^4 \gamma^2}\frac{\partial}{\partial \mu}\left[(1-\mu^2)\frac{\partial f}{\partial \mu}\right] + \frac{\lambda_0}{c\beta} S(E,\mu,s,t). \qquad (2.2)\end{aligned}$$

Here $\lambda_0(s) \equiv (10^{24}\ \mathrm{cm})/n(s) \ln \Lambda$ where $n(s)$ is the background plasma density. The source term $S(E,\mu,s,t)$ takes into account the acceleration mechanism where the acceleration timescale is assumed to be much faster than the magnetic mirroring or collision timescales. Given the distribution of electrons in space s, energy E, and pitch angle cosine μ, at some initial time t_0, and given a source S, the distribution is found at any later time t. In the next two chapters we outline the analytic and numerical solution of equation (2.2).

Table 2.1 - Energy and Pitch Angle Rates of Change

Process	$\dot{E}$	$\dot{\mu}$
Coulomb Collisions	$-4\pi r_0^2 nc\ln\Lambda/\beta$	0
Synchrotron	$-\frac{2}{3}r_0^2B^2\gamma^2\beta^2(1-\mu^2)/mc$	$-\frac{2}{3}r_0^2B^2\mu(1-\mu^2)/mc\gamma$
External Force	$\beta\mu F_{\|}/mc$	$(1-\mu^2)F_{\|}/\gamma\beta mc$
Magnetic Mirroring	0	$-\frac{1}{2}\beta c(1-\mu^2)(d\ln B/ds)$
Alfvén Waves	$(1/\gamma\beta^2)(1+\beta^2)D_{EE}^{\mathrm{Alfven}}$	$(1/\gamma\beta^2)(1+\beta^2)D_{E\mu}^{\mathrm{Alfven}}$
Langmuir Waves	$(1/\gamma\beta^2)(1+\beta^2)D_{EE}^{\mathrm{Langmuir}}$	0

Table 2.2 - Diffusion Terms

Process	$D_{\mu\mu}$	D_{EE}	$D_{E\mu}$
Coulomb Collisions	$(4\pi r_0^2 nc\ln\Lambda/\beta^3\gamma^2)(1-\mu^2)$	0	0
Alfvén Waves	$(1-\mu v_A/v)^2 D_+(\mu) + (1+\mu v_A/v)^2 D_-(\mu)$	$\beta^4\gamma^2(v_A/v)^2(D_+(\mu)+D_-(\mu))$	$\beta^2\gamma(v_A/v)[(1-\mu v_A/v)D_+(\mu) - (1+\mu v_A/v)D_-(\mu)]$
Langmuir Waves	$(1-\mu^2)(ncr_0^2\varepsilon_L/2\beta^3\gamma^2)[(c^2/\omega_p^2) < k^{-1} > -(1/\beta^2) < k^{-3} >]$	$(ncr_0^2\varepsilon_L/\beta) < k^{-3} >$	0

For Alfvén Waves:

$$D_+(\mu) \equiv \frac{\pi}{2}\frac{\Omega^2}{\gamma^2 B^2}\frac{(1-\mu^2)}{|v\mu - v_A|}\left[I^L(k_-) + I^R(-k_-)\right]$$

$$D_-(\mu) \equiv \frac{\pi}{2}\frac{\Omega^2}{\gamma^2 B^2}\frac{(1-\mu^2)}{|v\mu + v_A|}\left[I^L(k_+) + I^R(-k_+)\right]$$

$$k_\pm \equiv \frac{\Omega}{\gamma(v\mu \pm v_A)}$$

$$v_A \equiv \frac{B}{(4\pi(m_p+m_e)n)^{1/2}}$$

$$\Omega = \frac{eB}{m_e c}$$

For Langmuir Waves:

$$< f(k) > \equiv \frac{4\pi\int_{\omega_p/c\beta}^{\infty} f(k)W(k)k^2dk}{\varepsilon_L}$$

$$\varepsilon_L \equiv 4\pi\int_{\omega_p/c\beta}^{\infty} W(k)k^2dk$$

$$\omega_p^2 \equiv \frac{4\pi ne^2}{m_e}$$

CHAPTER 3. ANALYTIC SOLUTIONS

3.1 - Introduction

In this chapter we develop analytic solutions to the time dependent Fokker-Planck equation (2.2), and apply these solutions to the study of short timescale hard X-ray bursts from flares. Recent observations from the hard x-ray burst spectrometer (HXRBS) on SMM have provided high time resolution spectral information on hard x-ray bursts (Kiplinger et al 1983). Figure 3.1 shows an example of a burst with a rise time of $\sim .25\,\mathrm{s}$ and a decay time of $\sim .4$ s reported by Kiplinger et al (1984). Over the course of a burst, the spectra show gradual softening on timescales of a tenths of a second and shorter (Kiplinger et al 1984, see also Kane and Anderson 1970). Since this time is of the order of the collisional timescale for particles, steady state treatments of the problem are not valid. Emslie (1983) considered the time dependent problem but did not include the full effect of scattering on the distribution of electrons. We therefore make use of equation (2.2) to describe the evolution of energetic electrons in a solar flare.

In section 3.2 we present analytic solutions for the case when the background plasma is of constant density, and for the case when the background plasma density is spatially varying but the electrons are moving with small pitch angles with respect to the magnetic field. In section 3.3 we assume a model for the x-ray burst region and use the solutions developed in section 3.2 to calculate the bremsstrahlung x-ray spectra produced as a function of time. We then compare these time dependent x-ray spectra to the observations, and from this place constraints on the length of the coronal magnetic loops and on the characteristics of the initial injection spectrum of the electrons. Section 3.4 provides a summary of the analytic results.

3.2 - Analytic Solutions

The Fokker-Planck equation (2.2) describing the evolution of a distribution $f(E, \mu, s, t)$ of electrons injected into a cold ionized hydrogen plasma with a magnetic field of strength B can be written

$$\frac{\lambda_0}{c\beta}\frac{\partial f}{\partial t} + \mu\frac{\partial f}{\partial \tau} = \frac{(1-\mu^2)}{2}\frac{dlnB}{d\tau}\frac{\partial f}{\partial \mu} + \frac{1}{\beta}\frac{\partial}{\partial E}(\frac{f}{\beta}) + \frac{1}{\beta^4\gamma^2}\frac{\partial}{\partial \mu}[(1-\mu^2)\frac{\partial f}{\partial \mu}]. + \frac{\lambda_0}{c\beta}S(E, \mu, s, t) \tag{3.1}$$

This is an extension of the steady state Fokker-Planck equation derived in Leach 1984, (see also Leach and Petrosian 1981), to which we have added the time evolution term $(\lambda_0/c\beta)\partial f/\partial t$ and the source term S representing the injected particle rate. Here we have defined the dimensionless column depth τ as $d\tau \equiv ds/\lambda_0 \equiv nds/N_0$, where $N_0 = (10^{24}\,\mathrm{cm}^{-2})(\ln\Lambda)^{-1}$. The length scale $\lambda_0 \equiv (10^{24}\,\mathrm{cm})(n_e/\,\mathrm{cm}^{-3})^{-1}(\ln\Lambda)^{-1}$, where n_e is the background electron number density and $\ln\Lambda \approx 20$ is the Coulomb logarithm. Note that λ_0 is in general a function of the spatial coordinate s.

From a given distribution $f(E, \mu, s, t)$, it is a straightforward matter to evaluate the bremsstrahlung spectrum $I(k, \theta, s, t)$ as a function of the angle of emission θ with respect to the local magnetic field, and the photon energy k (in units of m_ec^2) at each space and time point. However, the high time resolution x-ray observations are spatially unresolved and thus correspond to the x-ray flux integrated over the entire emission region, which we assume to be a closed magnetic loop. The spatially integrated x-ray spectrum in a direction Θ with respect to some fixed axis (such as the earth-sun axis) is then

$$I(k, t, \Theta) = \int_k^\infty dE \int_{-1}^1 d\mu \int_{-\infty}^\infty nc\beta f(E, \mu, t, s)\sigma(k, \Theta, E, \mu)ds, \tag{3.2}$$

where $\sigma(k, \Theta, E, \mu)$ is the bremmstrahlung cross section for emission of photons of energy k in the direction Θ by electons of energy E and pitch angle cosine μ.

In general, because of the complex geometry of the flaring loop, the angles θ, Θ, and μ are related in a complicated manner which is a function of position. At low energies (k, $E \ll 1$), σ is nearly isotropic so we can take σ out of the integrals over s and μ. As k and E increase, this approximation becomes less and less valid. However, at higher energies most of the emission will come from deeper regions of the chromosphere where the magnetic field is approximately straight. In this case Θ is independent of s so we can again take σ out of the integral over s. Then if we define an integrated electron flux

$$F(E,t,\mu) \equiv \int_{-\infty}^{\infty} c\beta f(E,\mu,s,t)d\tau = \frac{1}{N_0}\int_{-\infty}^{\infty} c\beta f(E,\mu,s,t)n(s)ds, \tag{3.3}$$

equation (3.2) becomes

$$I(k,t,\Theta) = N_0 \int_k^{\infty} dE \int_{-1}^{1} d\mu F(E,\mu,t)\sigma(k,\Theta,E,\mu). \tag{3.4}$$

If we integrate equation (3.4) over all directions of emission we obtain the total spectrum as a function of time.

$$I(k,t) = N_0 \int_k^{\infty} G(E,t)\sigma(k,E)dE \tag{3.5}$$

$$G(E,t) \equiv \int_{-1}^{1} F(E,\mu,t)d\mu \tag{3.6}$$

Here $\sigma(k,E)$ is the integrated (over angles) bremsstrahlung cross section. For non-relativistic energies the Bethe-Heitler cross section is used.

$$\sigma(k,E) = \frac{8}{3}\alpha r_0^2 \frac{m_e c^2}{kE} \ln\left(\frac{1+(1-k/E)^{1/2}}{1-(1-k/E)^{1/2}}\right) \tag{3.7}$$

Here α is the fine structure constant and r_0 is the classical electron radius. The spectrum in a particular direction may, however, be different than the total spectrum. In general for energies below 100 keV we expect the difference to be small (Petrosian 1973), especially if we consider the effect of the photospheric albedo (Bai and Ramaty 1978, Langer and Petrosian 1977) which tends to isotropize the emission. More importantly however, the time evolution of both the mean and directional spectra will be similar so that $I(k,t)$ will give us a good representation of the temporal evolution of the emission in a particular direction. For the purposes of this paper we are primarily concerned with the temporal evolution of the x-ray spectrum. A more detailed analysis would have to take into account the anisotropic emission, the photospheric albedo, and the geometry of the loop. Furthermore, we neglect the effects of plasma wave generation by the electron beam which could alter the spectral time variations we will consider.

With the approximations of equations (3.5) and (3.7) it can be shown that the logarithmic part of equation (3.7) has negligible effect on the spectra at the level of the existing observations (Brown 1971, Petrosian 1973). In this case a power law integrated flux $F(E) \propto E^{-\delta}$ will lead to a power law x-ray spectrum $I(k) \propto k^{-\delta-1}$. As we shall see, for an electron injection spectrum which is a power law, the integrated electron flux $G(E,t)$ will be an approximate power law so that the approximation $I(k,t) \propto G(k,t)/k$ is valid. Consequently, we shall use the electron spectrum $G(E,t)$ to distinguish between models. We have however tested the validity of this approximation by integrating equation (3.5) and found it to be within the accuracy needed for this analysis.

In other astrophysical situations, however, and for higher spatial and spectral resolution, knowledge of the spatial and angular dependance of the distribution function may be required. We therefore present first some general solutions explicitly showing the spatial and angular dependence of the electron distribution.

3.2.2 Homogeneous Case

1) General Solution: Here we assume the plasma density and magnetic field are constant so that λ_0 is constant and $d\ln B/ds = 0$. It is then useful to define the dimensionless time variable y,

$$y \equiv \frac{ct}{\lambda_0} \equiv \frac{t}{T}. \tag{3.8}$$

Integrating equation (3.1) over τ and making use of the fact that there are no particles at $\tau = \pm\infty$ we obtain

$$\frac{\partial F}{\partial y} = \beta\frac{\partial}{\partial E}\left(\frac{F}{\beta^2}\right) + \frac{1}{\beta^3\gamma^2}\frac{\partial}{\partial \mu}\left[(1-\mu^2)\frac{\partial F}{\partial \mu}\right] + \mathcal{F}(E,\mu,t). \tag{3.9}$$

Here $\mathcal{F}$ is the integral over all τ of $\beta S/c$. This equation also describes the situation where the same distribution of electrons is injected throughout an infinite and homogeneous plasma. We first assume instantaneous injection ($S \propto \delta(t)$) so that we can neglect the source term for $t \neq 0$ and solve the homogeneous equation.

Defining new variables $\phi \equiv F/\beta^2$, $d\tilde{\eta} \equiv \beta dE$, and $d\rho/d\tilde{\eta} \equiv 1/\beta^3\gamma^2$ so that

$$\tilde{\eta} = (E^2 + 2E)^{\frac{1}{2}} + \sin^{-1}\left(\frac{1}{E+1}\right), \tag{3.10}$$

and

$$\rho = \frac{1}{2}\ln\left(\frac{E}{E+2}\right), \tag{3.11}$$

equation (3.9) for $t \neq 0$ becomes

$$\frac{\partial \phi}{\partial y}\frac{\partial \tilde{\eta}}{\partial \rho} - \frac{\partial \phi}{\partial \rho} = \frac{\partial}{\partial \mu}\left[(1-\mu^2)\frac{\partial \phi}{\partial \mu}\right]. \tag{3.12}$$

The distribution ϕ is now separable and can be written in the form

$$\phi(\tilde{\eta},\mu,y) = \sum_{l=0}^{\infty} e^{l(l+1)\rho(\tilde{\eta})} Z_l(y+\tilde{\eta})P_l(\mu), \tag{3.13}$$

where $P_l(\mu)$ are the Legendre polynomials, and $Z_l(y+\tilde{\eta})$ are functions to be determined from the boundary condition of the distribution of electrons at injection.

In what follows we shall assume that the accelerated (or injected) electron flux distribution is separable in pitch angle and energy:

$$\mathcal{F}(E,\mu,y) = g(\tilde{\eta})h(\mu)\delta(y), \tag{3.14}$$

which is equivalent to the boundary condition $F(\tilde{\eta},\mu,y=0) = g(\tilde{\eta})h(\mu)$.

Equating the flux obtained from equation (3.13) at $y=0$ with the boundary condition from equation (3.14), and using the orthogonality of the $P_l(\mu)$ we obtain

$$Z_l(\tilde{\eta}) = \frac{2l+1}{2} e^{-l(l+1)\rho(\tilde{\eta})} \frac{g(\tilde{\eta})}{\beta^2(\tilde{\eta})} \int_{-1}^{1} P_l(\mu')h(\mu')d\mu'. \tag{3.15}$$

Inserting $Z_l(\tilde{\eta}+y)$ back into equation (3.13) gives

$$\begin{aligned} F_\delta(t,E,\mu) = {} & \frac{\beta^2(\tilde{\eta})}{\beta^2(\tilde{\eta}+y)} g(\tilde{\eta}+y)\times \\ & \sum_{l=0}^{\infty} \frac{2l+1}{2}\left[\int_{-1}^{1} P_l(\mu')h(\mu')d\mu'\right] e^{-l(l+1)[\rho(\tilde{\eta}+y)-\rho(\tilde{\eta})]} P_l(\mu) \end{aligned} \tag{3.16}$$

for the distribution of the flux of electrons at $t>0$ for a delta function injection at $t=0$ (as denoted by the δ subscript on F).

Note that the factor

$$e^{-l(l+1)[\rho(\tilde{\eta}+y)-\rho(\tilde{\eta})]} = \left[\left(\frac{E(\tilde{\eta}+y)}{E(\tilde{\eta})}\right)\left(\frac{E(\tilde{\eta})+2}{E(\tilde{\eta}+y)+2}\right)\right]^{-l(l+1)/2}$$

decreases rapidly with increasing l and time y so that only a limited number of terms need be considered in the sum as y increases.

As is evident, the distribution scales with time as $\tilde{\eta}+y$. In general, $g(\tilde{\eta})$ will be a rapidly decreasing function of $\tilde{\eta}$ such as a power law in energy. We can therefore identify $y=\tilde{\eta}$ as the stopping time for electrons of energy parameter $\tilde{\eta}$. For non-relativistic particles, $\tilde{\eta} \approx E^{3/2}$, so the stopping time will be proportional to $E^{3/2}$. This is as expected since the scattering cross section decreases as E^{-2} while the rate at which the electron travels through the plasma increases as $E^{1/2}$.

The general solution for an arbitrary injection time profile $\mathcal{F}(E,\mu,t) = g(\tilde{\eta})h(\mu)k(y)$ is found by convolving the solution for a delta function injection with $k(y)$

$$F(E,\mu,t) = \int_{-\infty}^{y} k(y')F_\delta(y-y')dy'. \tag{3.17}$$

2) The Small Pitch Angle Solution: In the limit of small pitch angle (electrons moving approximately parallel to the field lines, $\mu \approx 1$), the solution can be expressed in a more manageable form which involves an integral instead of an infinite series. This integral can be performed in closed form in certain cases. In addition, this solution can be extended to the inhomogeneous (τ dependent) case as described in the next part.

Let α be the sine of the pitch angle

$$\alpha \equiv (1-\mu^2)^{\frac{1}{2}} \approx \text{pitch angle} \ll 1 \tag{3.18}$$

To first order in α equation (3.9) becomes

$$\frac{\partial F}{\partial y} = \beta\frac{\partial}{\partial E}(\frac{F}{\beta^2}) + \frac{1}{\beta^3\gamma^2}\frac{1}{\alpha}\frac{\partial}{\partial\alpha}(\alpha\frac{\partial F}{\partial\alpha}). \tag{3.19}$$

Again we have assumed a delta function in time injection. This equation is similar to the spatially homogeneous but time independent equation solved by Leach and Petrosian (1981). Following the same procedure, we expand the pitch angle dependence in terms of the Bessel functions $J_0(\omega\alpha)$ instead of Legendre polynomials. The solution is otherwise similar to the solution of equation (3.9).

$$F_\delta(E,t,\mu) = \frac{\beta^2(\tilde{\eta})}{\beta^2(\tilde{\eta}+y)}g(\tilde{\eta}+y)\times$$
$$\int_0^\infty e^{-\omega^2[\rho(\tilde{\eta}+y)-\rho(\tilde{\eta})]}\left[\int_0^\infty J_0(\omega\alpha')h(\alpha')\alpha' d\alpha'\right]J_0(\omega\alpha)\omega d\omega \tag{3.20}$$

For an initial distribution which is gaussian in α,

$$h(\alpha) = \left(\frac{2}{\alpha_0^2}\right)e^{-\alpha^2/\alpha_0^2}, \tag{3.21}$$

the integrals in equation (3.20) can be solved to yield a pitch angle distribution which remains gaussian, but with a dispersion which increases in time.

$$F_\delta(t,E,\mu) = \frac{\beta^2(\tilde\eta)}{\beta^2(\tilde\eta+y)} g(\tilde\eta+y) \left(\frac{2}{\alpha_t^2}\right) e^{-\alpha^2/\alpha_t^2}. \tag{3.22}$$

$$\alpha_t^2 \equiv \alpha_0^2 + 4[\rho(\tilde\eta+y) - \rho(\tilde\eta)] \tag{3.23}$$

The small pitch angle approximation breaks down at non-relativistic energies for times $y \gtrsim E^{3/2}$ since electrons of energy E are scattered away from the small pitch angle regime in time of order $y \approx E^{3/2}$. We have compared the exact solution (3.16) and the approximate solution (3.22) for a gaussian pitch angle injection with $\alpha_0^2 \ll 1$. We find them to agree well (within $\sim$ 20%), for $\alpha \lesssim .2$, and for $y \lesssim E^{3/2}$ when the summation of Legendre Polynomials in equation (3.16) was truncated at $l = 12$.

The integration over μ of the exact solution equation (3.16) (or the solution (3.22)) is trivial and replaces the series in (3.16) (or the last two terms in (3.22)) with unity. Substituting this into equation (3.17) we obtain the general integrated time dependent electron spectrum $G(E,t)$ needed for the calculation of the bremsstrahlung spectrum.

$$G(E,t) = \int_{-\infty}^{y} \frac{\beta^2(\tilde\eta)}{\beta^2(\tilde\eta+y-y')} g(\tilde\eta+y-y') k(y') dy' \tag{3.24}$$

This result can also be obtained directly by noting that integration of equation (3.12) over $d\mu$ gives zero on the right hand side. Solving the resulting equation gives equation (3.24).

3.2.3 - Inhomogeneous Case

There is no analytic solution for the general homogeneous case but turns out that in the small pitch angle regime a solution is possible using a method similar to that used for the homogeneous case in the small pitch angle limit (albeit a a complicated one). This solution includes the effects of spatial variation of the background density and magnetic field (for a distribution integrated over pitch angle). Since λ_0 (or T) is now a function of τ, we no longer use the variable y. Making the T dependence explicit, the equation to be solved is

$$\frac{T(\tau)}{\beta}\frac{\partial f}{\partial t}+\frac{\partial f}{\partial \tau}=\frac{1}{\beta}\frac{\partial}{\partial E}\left(\frac{f}{\beta}\right)+\frac{1}{\beta^4\gamma^2}\frac{1}{\alpha}\frac{\partial}{\partial \alpha}\left(\alpha\frac{\partial f}{\partial \alpha}\right)+\frac{T(\tau)}{\beta}S. \tag{3.25}$$

Here we have assumed $d\ln B/ds = 0$.

1) Uniform Magnetic Field: With a similar change of variables which led to equations (3.10) to (3.12), equation (3.25), valid for small pitch angles, can be written as

$$T\frac{\partial \tilde{\eta}}{\partial \rho}\frac{\partial \phi}{\partial t}+\beta\frac{\partial \tilde{\eta}}{\partial \rho}\frac{\partial \phi}{\partial \tau}-\frac{\partial \phi}{\partial \rho}=\frac{1}{\alpha}\frac{\partial}{\partial \alpha}\left(\alpha\frac{\partial \phi}{\partial \alpha}\right), \tag{3.26}$$

where we have dropped the source term for $\tau \neq 0$. Solutions to this equation take the form

$$\phi=\int_0^\infty e^{\omega^2\rho(\tilde{\eta})}\Psi(\omega,t,\tilde{\eta},\tau)J_0(\omega\alpha)d\omega, \tag{3.27}$$

where the function $\Psi(\omega,t,\tilde{\eta},\tau)$ satisfies the equation

$$\frac{T}{\beta}\frac{\partial \Psi}{\partial t}+\frac{\partial \Psi}{\partial \tau}-\frac{\partial \Psi}{\partial \eta}=0, \tag{3.28}$$

and ϕ is now defined to be f/β. The variable η is defined such that

$$\frac{d\eta}{d\tilde{\eta}}\equiv\beta \tag{3.29}$$

$$\eta=\int\beta^2dE=\frac{E^2}{E+1} \tag{3.30}$$

Defining new variables x and z

$$x\equiv\frac{1}{2}(\tau-\eta), \tag{3.31}$$

$$z\equiv\frac{1}{2}(\tau+\eta), \tag{3.32}$$

and using the chain rule

$$\frac{\partial}{\partial\tau}=\frac{1}{2}\frac{\partial}{\partial x}+\frac{1}{2}\frac{\partial}{\partial z}, \tag{3.33}$$

$$\frac{\partial}{\partial\eta}=-\frac{1}{2}\frac{\partial}{\partial x}+\frac{1}{2}\frac{\partial}{\partial z}, \tag{3.34}$$

equation (3.28) becomes

$$\frac{T}{\beta}\frac{\partial\Psi}{\partial t}+\frac{\partial\Psi}{\partial x}=0. \tag{3.35}$$

Solutions to this equation take the general form

$$\Psi((x,z,t)=A\Big(t-\Omega(\eta,\tau)\Big)B(z) \tag{3.36}$$

$$\Omega(\eta,\tau)\equiv\int_{c(z)}^{x}\frac{T(z+x')}{\beta(z-x')}dx', \tag{3.37}$$

where the functions A, B, and c are determined by the initial conditions. The ω dependence of Ψ is suppressed here. We assume a separable initial distribution of electron flux injected at $\tau=0$ of the form

$$F(\eta,\alpha,\tau=0,t)=g(\eta)h(\alpha)k(t). \tag{3.38}$$

This is equivalent to setting the source term $S=g(\eta)h(\alpha)k(t)\delta(\tau)/cT(\tau)$. Noting that at $\tau=0$, x and z are equal to $-\frac{1}{2}\eta$ and $\frac{1}{2}\eta$ respectively, from equations (3.27), (3.36), and (3.37) we find

$$F(\tau=0)=\beta^2\int_0^\infty e^{\omega^2\rho(\eta)}A_\omega\Big(t-\Omega(\eta,\tau=0)\Big)B_\omega(\eta)J_0(\omega\alpha)d\omega \tag{3.39}$$

$$\Omega(\eta,\tau=0)=\int_{c(\frac{1}{2}\eta)}^{-\frac{1}{2}\eta}\frac{T(\frac{1}{2}\eta+x')}{\beta(\frac{1}{2}\eta-x')}dx'. \tag{3.40}$$

Next we multiply both sides by $J_0(\omega'\alpha)\alpha d\alpha$ and integrate over α using the relation

$$\int_0^\infty xJ_0(\omega x)J_0(\omega' x)dx=\frac{1}{\omega}\delta(\omega-\omega'). \tag{3.41}$$

Defining

$$H(\omega)\equiv\int_0^\infty J_0(\omega\alpha)h(\alpha)\alpha d\alpha, \tag{3.42}$$

we then find

$$g(\eta)k(t)H(\omega) = e^{\omega^2\rho(\eta)}A_\omega\Big(t - \Omega(\eta,\tau=0)\Big)B_\omega(\eta). \tag{3.43}$$

The function $\Omega(\eta,\tau=0)$ must be equal to zero for the solution to be a product of a function of t and a function of η. For this integral to be zero for arbitrary functions $T(\tau)$, the limits of integration must be equal. Thus we can identify

$$c(\frac{1}{2}\eta) = -\frac{1}{2}\eta, \tag{3.44}$$

$$B_\omega(\eta) = \frac{1}{\beta(\eta)}e^{-\omega^2\rho(\eta)}g(\eta)H(\omega), \tag{3.45}$$

$$A_\omega(t) = k(t), \tag{3.46}$$

$$\Omega(\eta,\tau) = \int_{-z}^{x}\frac{T(z+x')}{\beta(z-x')}dx'. \tag{3.47}$$

We can rewrite $\Omega(\eta,\tau)$ in a simpler form using the substitution

$$\tau' \equiv z + x', \tag{3.48}$$

$$d\tau' = ds'/\lambda_0(s'), \tag{3.49}$$

$$\Omega(\eta,\tau) = \int_{-z}^{x}\frac{T(z+x')}{\beta(z-x')}dx' = \int_0^s\frac{ds'}{c\beta(\eta+\tau-\tau(s'))}. \tag{3.50}$$

Reintroducing the τ dependence, the flux distribution function becomes

$$\begin{aligned} F(E,\mu,\mathrm{s},t) = &\frac{\beta^2(\eta)}{\beta^2(\eta+\tau)}g(\eta+\tau)k\Big(t-\Omega(\eta,\tau)\Big) \\ &\int_0^\infty e^{-\omega^2[\rho(\eta+\tau)-\rho(\eta)]}H(\omega)J_0(\omega\alpha)\omega d\omega. \end{aligned} \tag{3.51}$$

Integrating this over $d\mu = \alpha d\alpha$ gives

$$W(E,\tau,t) \equiv \beta\int_{-1}^{1}fd\mu = \frac{\beta^2(\eta)}{\beta^2(\eta+\tau)}g(\eta+\tau)k\Big(t-\Omega(\eta,\tau)\Big) \tag{3.52}$$

where we have made use of equation (3.41) with $\omega' = 0$.

2) Non-uniform Magnetic Field: The integrated over pitch angle solution with varying magnetic field follows directly from this. Integrating equation (3.1) over all μ gives

$$\frac{\lambda_0}{c\beta^2}\frac{\partial W}{\partial t} + B(\tau)\frac{\partial}{\partial\tau}\left[\frac{1}{B(\tau)}\int_{-1}^{1}\mu f d\mu\right] = \beta\frac{\partial}{\partial\eta}\Big(\frac{W}{\beta^2}\Big) \tag{3.53}$$

For small pitch angle we make the approximation

$$\int_{-1}^{1}\mu f d\mu \approx W(E,\tau,t)/\beta \tag{3.54}$$

which is correct to second order in α. We then find that $W/\beta^2 B$ then satisfies the same differential equation as Ψ (equation 3.28).

$$\frac{T}{\beta}\frac{\partial(W/\beta^2 B)}{\partial t} + \frac{\partial(W/\beta^2 B)}{\partial\tau} - \frac{\partial(W/\beta^2 B)}{\partial\eta} = 0 \tag{3.55}$$

We can then immediately write

$$W(E,\tau,t) = \frac{B(\tau)}{B(\tau=0)}\frac{\beta^2(\eta)}{\beta^2(\eta+\tau)}g(\eta+\tau)k(t-\Omega(\eta,\tau)) \tag{3.56}$$

For the constant magnetic field case we now assume injection at a point, $S \propto \delta(\tau)$, so we can ignore the source term for $\tau \neq 0$. We will handle the solution at $\tau = 0$ by introducing a boundary condition at $\tau = 0$ analagous to equation (3.14). We assume an injected particle flux distribution separable in E, μ, and t of $cT(\tau)S(E,\mu,t) = g(\eta)h(\alpha)k(t)\delta(\tau)$, corresponding to the boundary condition at $\tau = 0$ of $F(E,\mu,\tau=0,t) = g(\eta)h(\alpha)k(t)$. For $h(\alpha)$ a gaussian as in equation (3.21) the integral over ω in equation (3.51) can be performed to yield

$$F(E,\mu,\tau,t) = \frac{\beta^2(\eta)}{\beta^2(\eta+\tau)}g(\eta+\tau)k\Big(t-\Omega(\eta,\tau)\Big)\Big(\frac{2}{\alpha_\tau^2}\Big)e^{\left(\frac{-\alpha^2}{\alpha_\tau^2}\right)}, \tag{3.57}$$

where $\alpha_\tau^2 \equiv \alpha_0^2 + 4[\rho(\eta+\tau)-\rho(\eta)]$ similar to equation (3.23). The function $\Omega(\eta,\tau)$ has the simple physical interpretation of being the the time it takes for an electron having energy $E(\eta+\tau-\tau(s'))$ at s' to travel a distance s. This electron has energy E at s but started out with energy $E(\eta+\tau)$ at $s=0$. Thus, the whole distribution scales with energy as $E(\eta+\tau)$. However, since the Fokker-Planck equation is a statistical equation and does not follow individual electrons, this does not describe what actually happens to a single electron but rather what happens to the distribution. For extremely relativistic particles, $\beta \approx 1$, this integral reduces to

$$\Omega(\eta,\tau)=\int_0^s \frac{ds'}{c}=\frac{s}{c}. \tag{3.58}$$

Thus the solution has a time dependence $k(t-s/c)$ which means that the distribution propogates along the field lines with velocity c. This is just what is expected for small pitch angle relativistic particles. We caution here that for extremely relativistic particles the equation used by Leach (1984) and here for the small pitch angle regime needs corrections (McTiernan and Petrosian 1989).

The function $\Omega(\eta,\tau)$ can also be expressed in closed form for the case of constant background density, T=constant. The time dependence will then be of the form

$$k(t-(\lambda_0/c)[\tilde{\eta}(\eta+\tau)-\tilde{\eta}(\eta)]). \tag{3.59}$$

where $\tilde{\eta}(\eta)$ is the function $\tilde{\eta}$ defined in equation (3.10) written as a function of η defined in equation (3.30). This assertion can be readily proven by inserting equation (3.51) into equation (3.25). Note that just as for the homogeneous case the flux integrated over pitch angle can be carried out trivially. This is also possible for the case with non-uniform magnetic field as long as the pitch angle remains small. The spatial integration, however, cannot be done analytically.

3.3 - Comparison With Observations

Here we present the variation in time of the x-ray spectrum assuming that the injected electron flux is a separable function of time, pitch angle, and energy as in equation (3.14). Furthermore, as described in section 3.2, for the purposes of this paper we need only to consider the spatially and angularly integrated electron spectrum $G(E,t)$.

Figure 3.2 shows G(E,t) for the constant density case (equation 3.24), for a gaussian injection time profile $k(t) = \exp(-t^2/t_0^2)$, and an initial energy spectrum which is a power law $g(E) \propto E^{-\delta}$. The important aspect to note about this figure is that the spectrum hardens in time. As was pointed out by previous authors (Kane and Anderson 1970, Petrosian 1973), spectral hardening is expected in a constant density background because the stopping time for non-relativistic electrons is proportional to $E^{3/2}$. Again, this assumes the injected electron energy spectrum does not change in time. Since the function $G(E,t)$ becomes flatter in time, we can immediately conclude that the electrons are not collisionally stopped in the constant density corona. If there is no appreciable magnetic mirroring which traps the electrons in the corona so that the majority of electrons only traverse down the loop once, then an upper limit can be placed on the integrated column density of the loop in the corona from the acceleration region to the transition region, N_{tr}. The absence of hardening in the spectrum shown in figure 3.3 shows that most of the electrons with $E \gtrsim .06$ (i.e. $\gtrsim 30$ KeV) go through the corona and enter the chromosphere. Thus $\tau_{tr} < \eta(E = .06) = 3.4 \times 10^{-3}$ or

$$N_{tr} \equiv \int_{corona} n ds < 1.7 \times 10^{20} \mathrm{cm}^{-2} \tag{3.60}$$

For a coronal density $n = 10^{10}\mathrm{cm}^{-3}$, this constrains the coronal loop length to be less than 1.7×10^{10}cm (not a very stringent limit).

This observation also places a limit on the convergence of the magnetic field, $d\ln B/d\tau$. This is because a converging field will trap electrons in the uniform density corona and produce x-ray spectra which harden in time. Just how small $d\ln B/d\tau$ must be depends on the pitch angle distribution since the smaller the pitch angles, the greater must be the magnetic convergence to trap the particles.

Our analytic solution assumes constant B field so that for a quantitative limit on $d\ln B/ds$, one needs numerical solutions of the Fokker-Planck equation. However, neglecting collisions in the low density coronal portion of the loop, we can estimate that the ratio of the field at the transition region to that at the injection region $(B_{tr}/B_{inj}) < \alpha_0^{-2}$.

Another argument against the electrons being stopped in the corona is that the decay time of the burst is too long for reasonable values of density. In order to produce a burst decay time of order a few tenths of a second in a uniform background, the background density must exceed $10^{12}\,\mathrm{cm}^{-3}$. This would be an extremely high coronal density. In any case, this would also produce a spectrum which hardens markedly over the course of the burst, contrary to the observations.

It is possible to produce a spectrum which softens in time with a background density which increases with distance from the injection point. This is because the higher energy electrons penetrate to the denser plasma faster and can thus decay faster than the lower energy electrons (cf Petrosian 1973). This condition requires the solution of the inhomogeneous equation. We can analyze this situation if the injected electrons have small pitch angles. The x-ray spectral evolution was calculated using equation (3.57) for a model where the input spectrum integrated over pitch angles was

$$F(E, s=0, t) = E^{-\delta} \exp(-t^2/t_0^2) \tag{3.61}$$

The density n was taken to be

$$n = \begin{cases} n_0 & 0 < s < s_t \\ n_0 \exp(s/s_0) & s > s_t \end{cases} \tag{3.62}$$

with s_t the half length of the loop above the transition region and s_0 the scale height below the transition region. Figure 3.3 shows the spectral evolution of $G(k,t)/k$ for $n_0 = 10^{10}\,\mathrm{cm}^{-3}$, $s_0 = 10^7\,\mathrm{cm}$, $s_t = 1.4 \times 10^9\,\mathrm{cm}$, $\delta = 4.2$, and

$t_0 = .13$ sec. For comparison, measured spectra from the HXRBS (from Kiplinger et al 1984) are also plotted on the same graphs. The calculated spectra are time integrated over 128 ms intervals in order to match the time resolution of the HXRBS.

The value of n_0 does not have much effect on the spectra because s_t and n_0 are chosen so that few electrons are stopped in the corona, $\tau(s_t) \ll \eta$. We also find that the degree of spectral softening is not very sensitive to the injected spectral index δ for $3 < \delta < 5$.

Values of the scale height s_0 greater than $\sim 3 \times 10^8$ cm did not lead to rapid enough spectral softening to be consistent with the observations. Once s_0 is reduced much below this value the degree of spectral softening remains essentially unchanged because the electrons are stopped rapidly compared to the 128 ms integration time.

In general, the larger s_t is, the higher the degree of spectral softening. This is because the faster electrons can become more spread out from the slower electrons before they reach the exponentially increasing density region. Values of s_t smaller than $\sim 5 \times 10^8$ cm did not lead to sufficiently rapid spectral softening, therefore ruling out a simple exponential density profile ($s_t = 0$). Thus the coronal loop length must be longer than $\sim 5 \times 10^8$ cm, which excludes the possibility of acceleration occurring close to or below the transition region. We therefore have for the density profile parameters the following constraints: $s_0 < 3 \times 10^8$ cm and $s_t > 5 \times 10^8$ cm.

The value of the injection width t_0 has a large effect on the spectral evolution. The larger the value of t_0, the smaller the amount of spectral softening because new particles are still being injected as the earlier particles reach the higher density regions. Small values of t_0 ($\lesssim .1$ s) lead to very rapid spectral softening and rapid decay of the burst. With the assumption of small pitch angles, injection widths

$t_0 \lesssim .1$ s are incompatible with observations. If the injection width is less than $\sim .1$ s then large pitch angle electrons ($\sin^{-1} \alpha \gtrsim 30°$) are needed to spread the pulse out before it reaches the high density region ($s > s_t$). On the other hand, $t_0 \gtrsim .2$ s leads to a burst decay which is too slow. Thus, this model requires $.1\,\mathrm{s} \lesssim t_0 \lesssim .2$ s.

Figure 3.4 compares the calculated spectra with the data at point 4 for values of these parameters (t_0, s_0, and s_t) outside of the acceptable ranges. The other parameters were adjusted so that the calculated spectra fit the data at times 1 and 2. As is evident, the calculated spectra at point 4 no longer fit the data.

3.4 - Summary and Discussion

We have solved the kinetic equation for accelerated particles undergoing Coulomb collisions in a background magnetized plasma. For a homogeneous plasma we have found an exact analytic solution describing the evolution of the distribution of particles in energy and pitch angles (with respect to the magnetic field). For an inhomogenous plasma, analytic solutions are possible only for particles with small pitch angles (namely, beams collimated along the field lines). We then compared the bremsstrahlung x-ray spectrum from a short burst of accelerated electrons with the high temporal resolution hard x-ray solar flare spectra observed by HXRBS on SMM.

The observed softening with time of the x-ray spectra rules out the homogeneous solution, which means that electrons do not lose most of their energy in the uniform density coronal portion of the flaring loop. Most of the x-ray emission then occurs at the base of the loop below the transition region. Consequently, the decay time and the degree of spectral softening are primarily determined by the spread in arrival time of the electron beam at the base of the loop. The more the particles are spaced out when they reach the transition region, the longer the burst decay time; and the greater the spread in arrival times between high and low energy particles, the higher the degree of spectral softening. The particles are spread out by a combination of the time of flight difference from the acceleration region to the chromosphere, and the initial injection time width. The pitch angle, the energy, and the distance from the acceleration region to the transition region determine the time of flight to the transition region. Since the effect of collisions in the corona is small, the time of flight over the distance s_t is $s_t/c\beta\mu$. The difference in time of flight between electrons of different energies is therefore proportional to s_t. Thus, smaller s_t leads to less spectral softening . Therefore, injection of the accelerated particles near or below the transition region is ruled out for such bursts.

Furthermore, the larger the range of pitch angles, the smaller the injection time t_0 has to be in order to reproduce the observations. The small pitch angle assumption basically amounts to ignoring the difference in path length between particles of different pitch angles. Thus the time of flight difference from the acceleration region to the thick target is determined solely by the difference in particle energies. This is why our assumption of small pitch angle requires that t_0 be greater than .1 s. Otherwise, the decay of the burst would be too short. Kiplinger et al (1984) used the non-thermal beam model of Emslie (1983) to model the same burst. They assumed uniform pitch angle distribution over some range of pitch angles and a delta function in time input. Their model contains a range of large pitch angle electrons so it can accomodate a delta function in time input.

We have found that under the assumption that the pitch angles are small and that the injection distribution is seperable in time and energy, the flare parameters must satisfy the constraints given in Table 3.1.

Finally, we can make some order of magnitude arguments to show that injection times of this length are reasonable. Let the total burst energy in x-rays be E_x. If the burst energy is supplied by magnetic reconnection, then

$E_x = (B^2/8\pi)VY\epsilon$. Here B is the magnitude of the magnetic field, and V is the volume of the accelerating region. The efficiency with which magnetic energy is converted into that of accelerated particles is ϵ and the efficiency with which the particle energy is converted into x-rays is Y. Typically Y is of the order 10^{-6} (Petrosian 1973). The acceleration timescale will be of order $t_0 \sim L/v_A$ where $L \sim V^{1/3}$ is the characteristic length of the acceleration region and $v_A = B/(4\pi\rho)^{1/2}$ is the Alfven velocity. For typical flare parameters, we find for the energy in x-rays

$$E_x \sim 10^{20}\left(\frac{B}{100\,\mathrm{Gauss}}\right)^5\left(\frac{t_0}{.1\,\mathrm{s}}\right)^3\left(\frac{n}{10^9\,\mathrm{cm}^{-3}}\right)^{-3/2}\epsilon\,\mathrm{ergs} \qquad (3.63)$$

The observed energy in x-rays of the flare shown in figure 3.1 is of order 10^{19} ergs, in agreement with this order of magnitude estimate.

For a more exact analysis of the high time resolution observations, general solutions including spatial inhomogeneities and large pitch angles are needed. This will require numerical solutions of the full equation. However, as shown by Leach and Petrosian (1981) and here for the homogeneous case, the small pitch angle solution is a good representation of the general solution and gives acceptable results to much larger pitch angle then expected.

TABLE 3.1 - Limits On Model Parameters

Flare Parameter	Constraint
injection time t_0	$.1\,\mathrm{s} < t_0 < .2\,\mathrm{s}$
electron spectral index δ	$4.1 < \delta < 4.5$
distance to transition region s_t	$s_t > 5 \times 10^8\,\mathrm{cm}$
column depth to transition region N_{tr}	$N_{tr} < 1.7 \times 10^{20}\,\mathrm{cm}^{-2}$
scale height below transition region s_0	$s_0 < 3 \times 10^8\,\mathrm{cm}$
B field convergence	$B_{tr}/B_{inj} < \alpha_0^{-2}$

Chapter 3 Figure Captions

Figure 3.1: An example of a short timescale hard x-ray burst (27-496 keV) reported by Kiplinger et al (1984). The spectra at points 1 through 4 are given by the circles in figure 3.3.

Figure 3.2: Log$[G(k,t)/k]$ representing the expected bremsstrahlung spectrum vs photon energy k (equation 3.24) at different times for a homogeneous background. The injection spectrum is $k(t) = \exp(-t^2/t_0^2)$ and $g(E) \propto E^{-\delta}$. The injection width is $t_0 = .05\,\mathrm{s}$, the injected spectral index $\delta = 4.2$, and the background density is $10^{11}\,\mathrm{cm}^{-3}$. The curves from A to G represent the spectrum from consecutive 128 ms time intervals. Note the spectral hardening with time.

Figure 3.3: Log$[G(k,t)/k]$ vs k equation (3.52) integrated over τ at different times. The injection profile is given in equation (3.61) with $\delta = 4.2$, and $t_0 = .13\,\mathrm{s}$. The density profile is given in equation (3.62) with $n_0 = 10^{10}\,\mathrm{cm}^{-3}$, $s_0 = 10^7\,\mathrm{cm}$, and $s_t = 1.4 \times 10^9\,\mathrm{cm}$. Curves 1 through 4 are seperated in time by 128 ms and correspond to the points 1 through 4 on figure 3.1. The circles are the measured spectra from the HXRBS with $\pm 1\,\sigma$ uncertainties (from Kiplinger et al 1984).

Figure 3.4: The same as figure 3.3 except we show Graph 4 for values of t_0, s_t, and s_0 outside of the ranges specified in section 3.4 showing how the graphs no longer match the observations. The remaining parameters (which turn out to be very close to those in figure 3) were chosen so that graphs 1 and 2 matched the observations. i) $t_0 = .08\,\mathrm{s}$; ii) $t_0 = .22\,\mathrm{s}$; iii) $s_t = 3.5 \times 10^8\,\mathrm{cm}$; iv) $s_0 = 5 \times 10^8\,\mathrm{cm}$

Figure 3.1

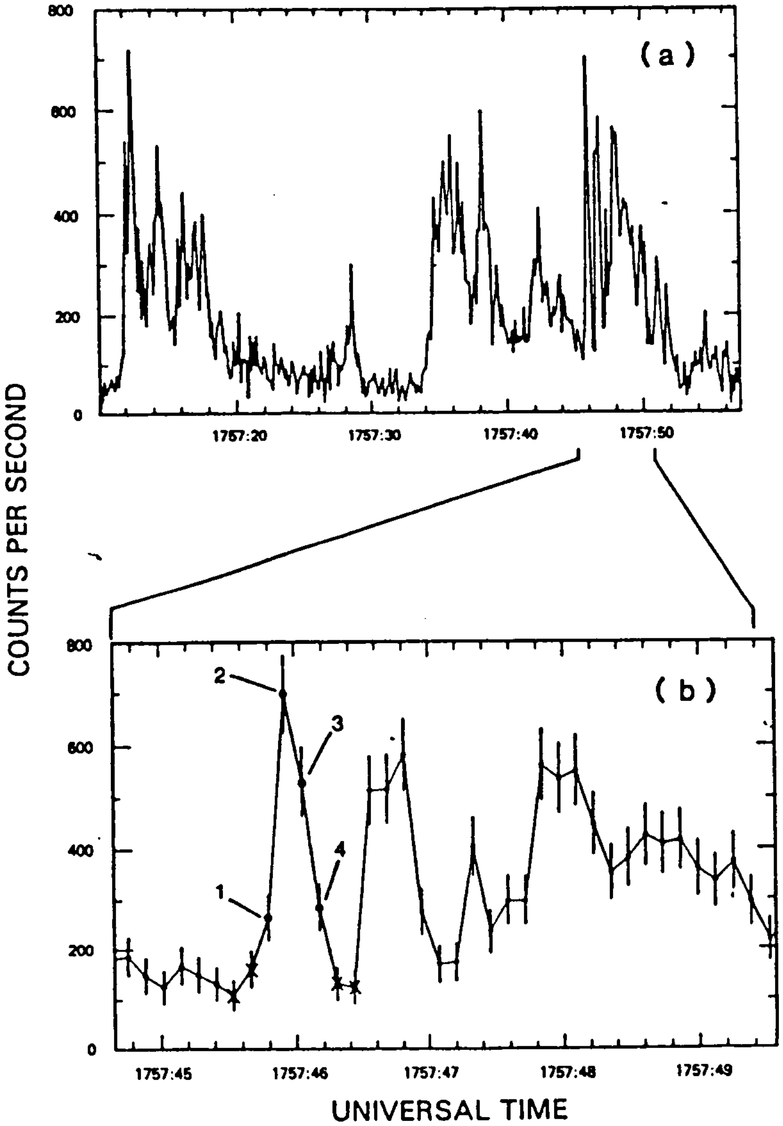
(a)
800
600
400
200
0
1757:20
1757:30
1757:40
1757:50
COUNTS PER SECOND
(b)
800
600
400
200
0
1
2
3
4
1757:45
1757:46
1757:47
1757:48
1757:49
UNIVERSAL TIME

Figure 3.2

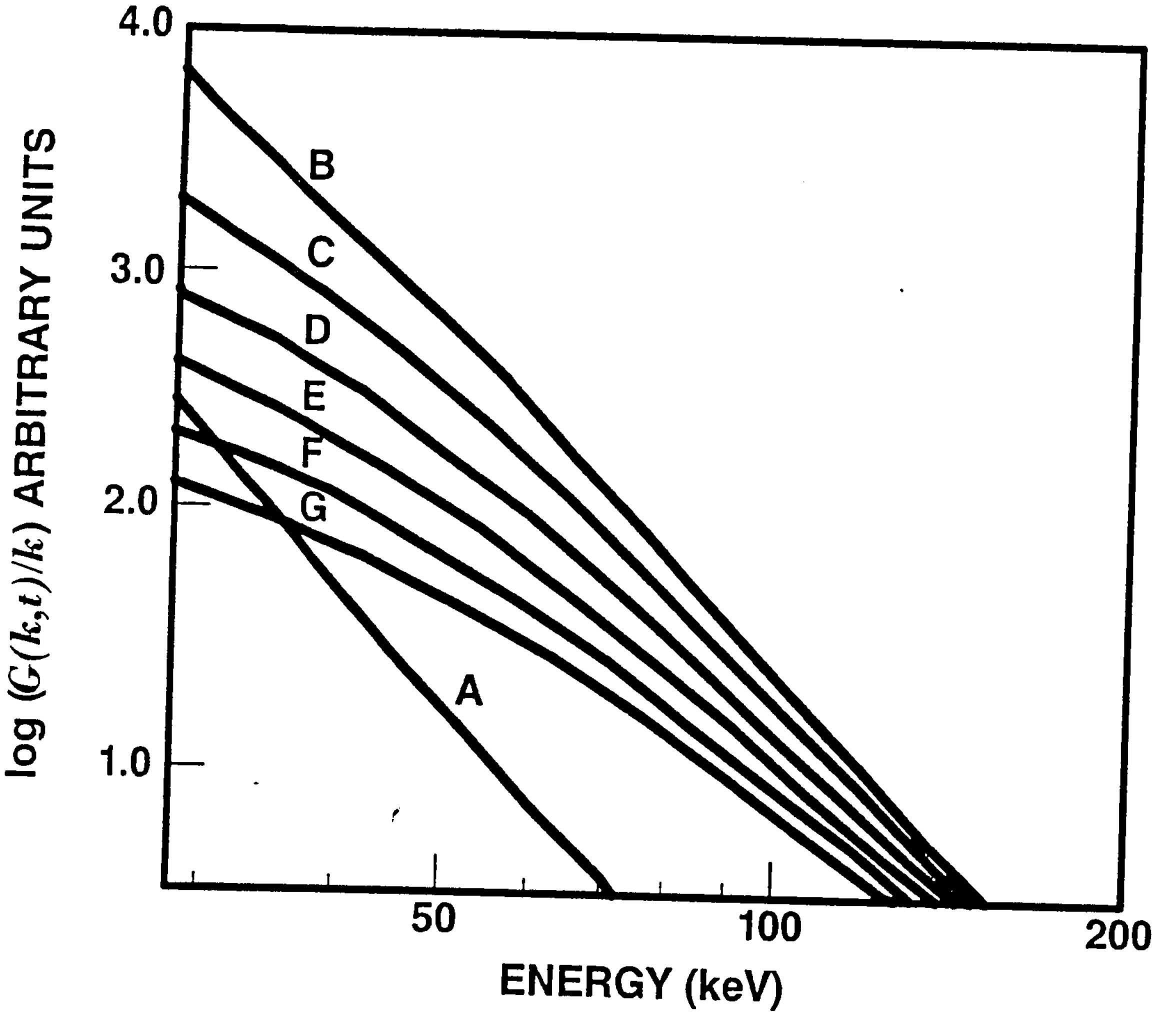
4.0
3.0
2.0
1.0
log ($\mathcal{G}(k,t)/k$) ARBITRARY UNITS
50
100
200
ENERGY (keV)
A
B
C
D
E
F
G

Figure 3.3

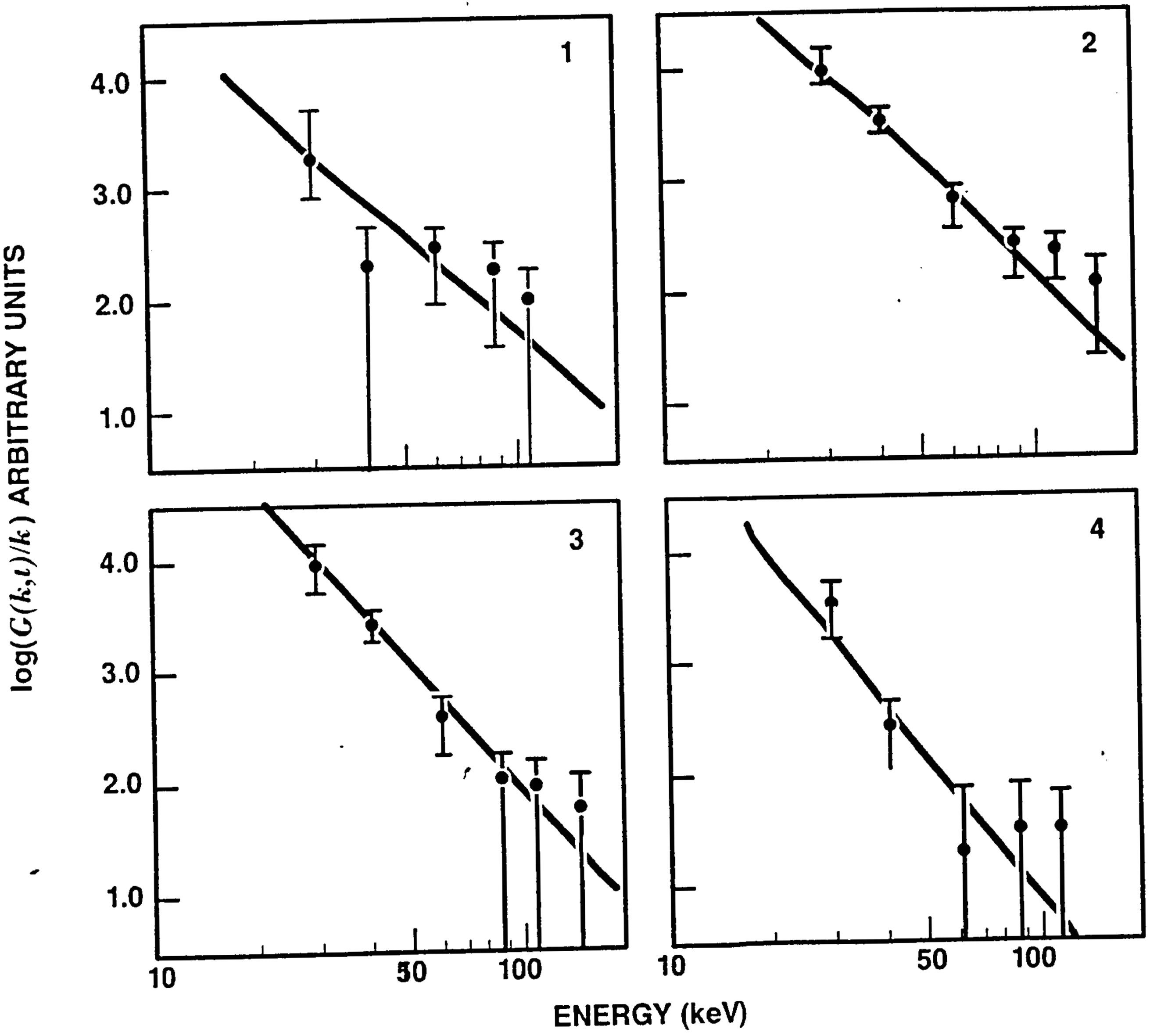

Figure 3.4

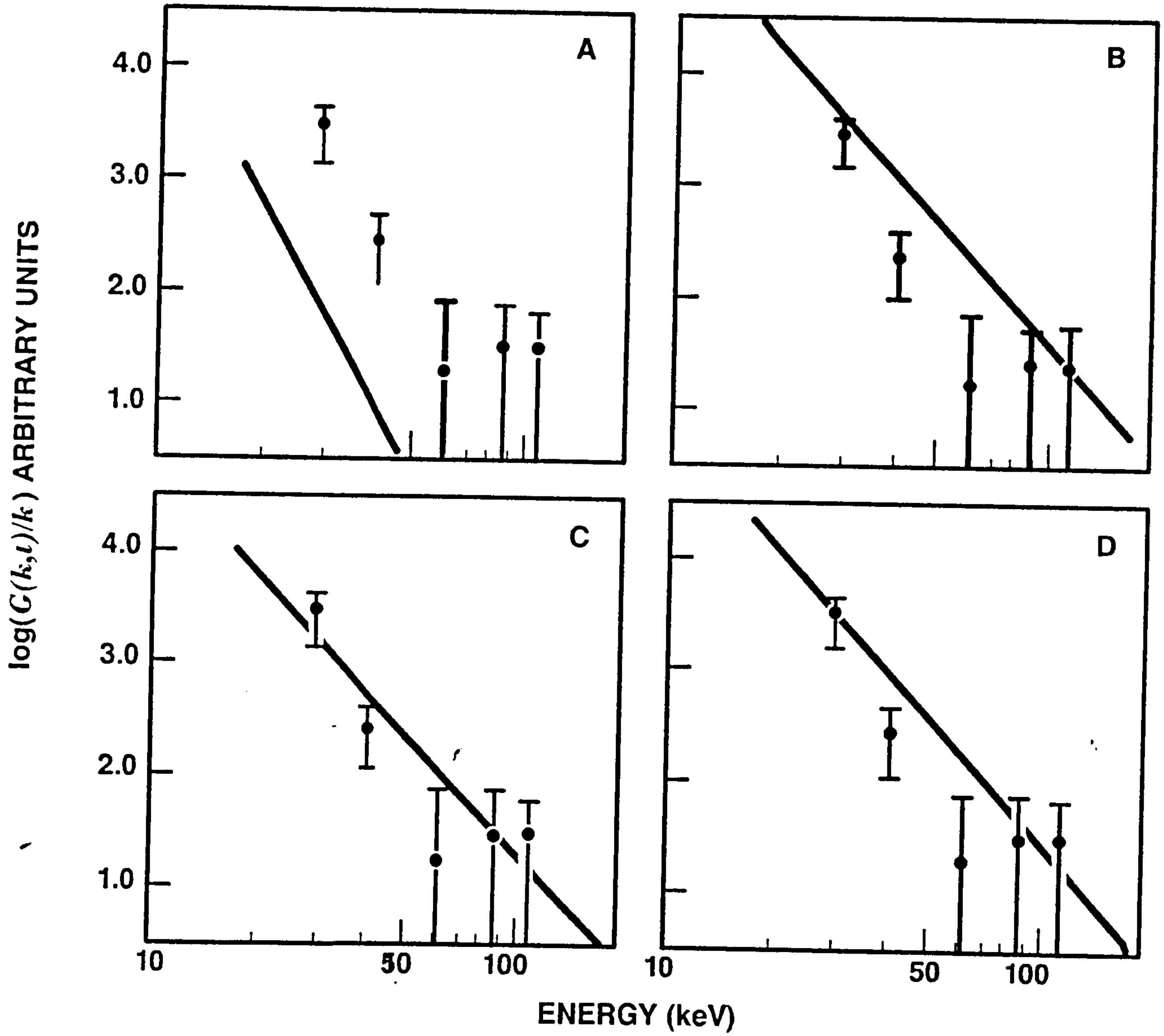

CHAPTER 4. NUMERICAL SOLUTIONS

4.1 - Introduction

In Chapter 3, analytic solutions were derived for the time dependent kinetic equation for electrons undergoing Coulomb collisions in a magnetized plasma. However, these solutions are only valid for simplified configurations such as constant plama density and magnetic field, or electrons moving with small pitch angle with respect to the magnetic field. To describe an inhomogeneous plasma and magnetic field with arbitrary electron angular distribution, we must turn to a numerical solution of the equation. In this chapter, we describe the numerical solution of the equation for a distribution of electrons evolving in a magnetized plasma including just Coulomb collisions and magnetic mirroring since these are the important processes for describing the evolution of the hard X-ray and microwave producing electrons in solar flares. The numerical solution including all of the terms is solved in an analagous manner. In part 4.2, we demonstrate the accuracy of the numerical scheme by comparisons with the analytic results of Chapter 3.

4.2 - Numerical Method

The problem we are confronted with is an initial value problem. There are a variety of techniques available for the numerical solution of such partial differential equations. We will use finite differencing, together with the powerful method of operator splitting (see Centrella and Wilson 1984, Hawley et al 1984). Finite differencing simply approximates the values of the derivatives of f in equation (2.2) evaluated on a fixed grid in E, μ, and s space. Operator splitting allows us to break up the right hand side of equation (2.2) into five terms and to deal with each term separately when advancing f in time. We therefore proceed as follows. Given the value of f at every point on the grid at time t, we use the finite difference approximations to the derivatives, along with operator splitting to calculate f at every point on the grid at time $t + \Delta t$. The process is then repeated to give f at $t + 2\Delta t$ and so on.

Operator splitting is a method of numerically solving a partial differential equation which contains a number of differential operators such as equation (2.2). Suppose a partial differential equation consists of k differential operators $\mathcal{D}_i$

$$\frac{\partial}{\partial t} U(x,t) = \sum_{i=1}^{k} \mathcal{D}_i U(x,t). \tag{4.1}$$

Furthermore, suppose the equations

$$\frac{\partial}{\partial t} U(x,t) = \mathcal{D}_i U(x,t) \tag{4.2}$$

have the known finite difference solutions

$$U(x, t + \Delta t) = D_i(\Delta t) U(x,t), \tag{4.3}$$

where $D_i(\Delta t)$ is the finite difference operator which advances the function U from time t to time $t+\Delta t$ for each individual differential operator $\mathcal{D}_i$. Then the solution of the full equation (4.1) is given by

$$U(x, t + \Delta t) = D_k(\Delta t) D_{k-1}(\Delta t) ... D_1(\Delta t) U(x,t). \tag{4.4}$$

In other words, we operate on $U(x,t)$ with $D_1(\Delta t)$, then operate on the result of this with $D_2(\Delta t)$, and so on for all the finite difference operators $D_k(\Delta t)$. This updates $U(x,t)$ to $U(x, t+\Delta t)$. Therefore, we need only to find the finite difference solutions for each operator in equation (4.1) to solve it completely. We then apply these operators cyclically to advance $U(x,t)$.

We view the right hand side of equation (2.2) as the sum of five distinct components; the position operator, the energy operator, the pitch angle scattering operator, the magnetic mirroring operator, and the source term. The addition of other terms to the equation to take into account other physical processes is thus straightforward. Next we give the finite difference schemes used to advance each term.

a) The Position, Energy and, Magnetic Mirror Terms

The form of the energy, position, and mirror operators is given by

$$\frac{\partial}{\partial t}U(x,t) = -A(x)\frac{\partial}{\partial x}U(x,t), \tag{4.5}$$

where $A(x)$ is some function of the general variable x. In addition to the standard requirements of accuracy and stability, we seek an explicit scheme to minimize the computation time. We use the Lax-Wendroff method, an explicit scheme which is second order accurate in time, to update the energy and position terms.

The method is based upon the Taylor series in time expansion of U. The time derivatives in the expansion are replaced using Equation (4.5) to give

$$U(x,t+\Delta t) = U(x,t) - \Delta t A(x)\frac{\partial U(x,t)}{\partial x} + \frac{(\Delta t)^2}{2}A(x)\frac{\partial}{\partial x}\left[A(x)\frac{\partial U(x,t)}{\partial x}\right]. \tag{4.6}$$

For the energy and mirroring terms, standard finite difference expressions are then used to replace the derivatives in equation (4.6) giving us the final form for the energy or mirroring update.

$$\begin{aligned} U_m^{n+1} &= U_m^n - \Delta t A_m\left(\frac{U_{m+1}^n - U_{m-1}^n}{x_{m+1} - x_{m-1}}\right) + \\ &\frac{(\Delta t)^2 A_m}{x_{m+1} - x_{m-1}}\left[A_{m+1/2}\left(\frac{U_{m+1}^n - U_m^n}{x_{m+1} - x_m}\right) - A_{m-1/2}\left(\frac{U_m^n - U_{m-1}^n}{x_m - x_{m-1}}\right)\right], \end{aligned} \tag{4.7}$$

where U_m^n is the value of $U(x_m, n\Delta t)$ at time $n\Delta t$ and grid point x_m, and $A_{m\pm1/2}$ are $A(x)$ evaluated at the half grid points, $(x_m + x_{m\pm1})/2$.

We handle the position term slightly differently however. Physically, equation (4.5) describes a distribution moving with velocity $A(x)$. Thus, for for $A_m > 0$, we expect the value of $U(x_m, t+\Delta t)$ to depend only on $U(x,t)$ for $x < x_m$, in other words on the upwind side. Note however that the approximation to the derivative with respect to x evaluated at x_m in the second term in equation (4.6) depends on U evaluated at both x_{m-1} and x_{m+1}. This makes the approximation accurate to second order in Δx. However, it also makes this numerical differencing scheme subject to transport errors. It can lead to large oscillations in $U(x)$ if $U(x)$ is a pulse which propagates a distance many times larger than the width of the pulse. We therefore approximate the first derivative as

$$\frac{\partial U(x_m,t)}{\partial x} = \begin{cases} \frac{U_m^n - U_{m-1}^n}{x_m - x_{m-1}} & A_m > 0 \\ \frac{U_{m+1}^n - U_m^n}{x_{m+1} - x_m} & A_m < 0 \end{cases} \tag{4.8}$$

This is known as upwind differencing. We still however retain the last term in equation (4.7), as this term takes the form of a diffusion operator which makes this differencing scheme stable. See Smith (1978) for a discussion of the accuracy of upwind differencing schemes.

The Lax-Wendroff scheme is numerically stable provided the familiar Courant-Friedrichs-Lewy condition

$$\frac{|A_m|\Delta t}{x_m - x_{m-1}} \leq 1 \tag{4.9}$$

is satisfied (see Press et al 1986). Strictly speaking, this stability criterion is only valid for constant A, but we will adopt it here as an estimate for the maximum Δt allowed. We will choose a value of Δt smaller than this limit by a factor of 4 to insure stability.

b) The Diffusive Pitch Angle Term

The pitch angle operator due to Coulomb scattering has the form of a diffusion term. By taking the outside derivative with respect to μ through the diffusion term in equation (2.2), the pitch angle terms can be written in the form

$$\frac{\partial}{\partial t}U(x,t) = B(x)\frac{\partial U(x,t)}{\partial x} + C(x)\frac{\partial^2 U(x,t)}{\partial x^2}. \tag{4.10}$$

To update these terms we use the Crank-Nicholson method, an implicit differencing scheme which is particularly well suited to solving diffusive initial value problems. The Crank-Nicholson method is second order accurate in time and is unconditionally stable (see Press et al 1986). We average the right hand side at times t and $t + \Delta t$ and obtain a coupled set of equations for $U(x, t + \Delta t)$.

$$\begin{aligned}\frac{U_m^{n+1} - U_m^n}{\Delta t} =& \frac{B_m}{2}\left[\frac{U_{m+1}^n - U_{m-1}^n}{x_{m+1} - x_{m-1}} + \frac{U_{m+1}^{n+1} - U_{m-1}^{n+1}}{x_{m+1} - x_{m-1}}\right] \\ &+ \frac{C_m}{x_{m+1} - x_{m-1}}\left[\left(\frac{U_{m+1}^n - U_m^n}{x_{m+1} - x_m} - \frac{U_m^n - U_{m-1}^n}{x_m - x_{m-1}}\right)\right. \\ &+ \left.\left(\frac{U_{m+1}^{n+1} - U_m^{n+1}}{x_{m+1} - x_m} - \frac{U_m^{n+1} - U_{m-1}^{n+1}}{x_m - x_{m-1}}\right)\right]. \qquad (4.11)\end{aligned}$$

Since the U_m^n are known, this equation can then be rewritten in the form of a tridiagonal matrix equation for U_m^{n+1}. It is then straightforward to solve this tridiagonal system of equations for U_m^{n+1} using a packaged routine.

c) Numerical Solution of the Full Equation

We have developed a computer code which solves equation (2.2) using the method outlined above. The main program is broken down into a number of subroutines so that modifications can be performed relatively easily. There are five subroutines which implement the finite difference operators $D_i(\Delta t)$ for each term on the right hand side of equation (2.2). These subroutines are called in succession to advance $f(E, \mu, s, t)$ in time.

In many astrophysical situations, electrons have a power law energy distribution. Therefore, in order to study the energy distribution over the maximum number of decades without a prohibitive number of energy grid points, we use a logarithmic energy grid. The background plasma density also may vary by many orders of magnitude, so again we use varying step sizes in our position grid. The position grid has smaller step sizes where the density is higher since the distribution evolves more rapidly in these locations.

To run the program, we first specify the magnetic field $B(s)$, the background density $n(s)$, and the source term $S(E, \mu, s, t)$. The energy, position, and pitch angle grids are then set up and Δt is chosen to insure stability. At specified time intervals, the value of $f(E, \mu, s, t)$ at all grid points is written out to disk so that analysis can be performed at a later time. For example, given the electron distribution, magnetic field, and density, one can calculate the bremsstahlung emission, synchrotron emission, and the growth rate of kinetic plasma instabilities.

4.3 - Tests and Comparison With Analytic Results

To demonstrate the accuracy of the program we compare the numerical results to known analytic solutions for simplified cases. The three situations we check are homogeneous injection in space, injection into a converging magnetic field configuration with low plasma density,and injection in a small physical region of a distribution beamed along a constant magnetic field. In the first example, the pitch angle scattering term and the energy loss term are nonzero. In the second example, the transport and magnetic mirroring terms dominate, while in the third example all but the magnetic mirroring is included.

a) Homogeneous Injection

To test the accuracy of the pitch angle scattering term and the energy loss term, we inject an electron distribution everywhere in space in a homogeneous plasma of density 10^{12} cm^{-3} with a constant magnetic field. The initial electron pitch angle distribution is greatest at $\mu = \pm 1$, goes to zero at $\mu = \pm .5$ and has a local maximum at $\mu = 0$, and is a power law in energy, $f(E, \mu, s, t = 0) = E^{-3.5}(2\mu^4 - \mu^2 + 1/8)$. The analytic solution to equation (2.2) for homogeneous injection in a homogeneous plasma is given by equation (3.16). Both the analytic and the numerical pitch angle distributions have been plotted in Figures 4.1 through 4.3 for energies 20, 141, and 1000 keV at times 0.15 and 0.5 seconds. As expected, the lower energy electrons isotropize and lose energy faster than the higher energy electrons. Note that the results agree to within a few percent even though the value of f decreases by several orders of magnitude from its initial value.

b) Converging Magnetic Field

The magnetic field configuration in the solar corona and in planetary magnetospheres is often in the form of a loop with larger magnetic field at the footpoints than at the apex. The pitch angles of electrons accelerated in the loop therefore increase as they move toward the footpoints. Electrons having large enough pitch angle are trapped in the loop until they lose their energy or are scattered to lower pitch angle and escape. The dynamics of electrons in magnetic loops is essential to the study of microwave emission in solar flares and cyclotron maser emission from stellar coronae and planetary magnetospheres.

In order to demonstrate the accuracy of the magnetic converging scheme used in our code, we inject electrons impulsively (at t=0) at the apex (s=0) of a magnetic loop containg zero density plasma. The injected spectrum is monoenergetic (1 MeV) with a gaussian pitch angle distribution peaked at 40° with a width of 10°. Therefore, no Coulomb energy losses or scattering occurs and the evolution of the electron distribution can be determined analytically by following the trajectories of individual electrons in phase space. We take the magnetic field of the loop as

$$B(s) = B_o(1 + (r_m - 1)s^2/L_c^2) \tag{4.12}$$

where L_c is the half length of the loop and $r_m = B(L_c)/B(0)$ is the mirror ratio. This choice of magnetic field corresponds to the far field of a dipole. For this situation the electron distribution at later times and positions is related to the injected distribution by

$$f(E_o, \mu, s, t) = f_o(E_o, \mu_o(\mu, s, t)) \tag{4.13}$$

where $\mu_o(\mu, s, t)$ is the initial pitch angle cosine expressed as a function of the pitch angle cosine and position at a later time t of an individual electron orbit. An electron injected into the loop at $t = 0$ with velocity βc and initial pitch angle cosine μ_o moves along the loop according to

$$s/L_c = \mu_o \sin\left(\beta c t\sqrt{(r_m - 1)(1 - \mu_o^2)}/L_c\right)/\sqrt{(r_m - 1)(1 - \mu_o^2)} \tag{4.14}$$

The pitch angle cosine at this position is

$$\mu(s) = \pm\left(1 - B(s)(1 - \mu_o^2)/B_o\right)^{1/2} \tag{4.15}$$

where the ± depends on the number of bounces made by the electron. From equations (4.14) and (4.15) we see that the maximum distance reached is $s_{max} = \mu_o L_c/\sqrt{(r_m - 1)(1 - \mu_o^2)}$, and that the bounce period is

$$T_B = 2\pi L_c/\beta c\sqrt{(r_m - 1)(1 - \mu_o^2)}.$$

Inverting these equations to find μ_o in terms of μ, s, and t completes the solution for the distribution at later times.

In Figure 4.4, we show the distribution

$$f(E_o, s, t) = \int_{-1}^{1} f(E_o, \mu, s, t)d\mu \tag{4.16}$$

at different times for the injected distribution described above calculated using our numerical code with $L_c = 10^9$ cm and $r_m = 5$. Since particles having different intial pitch angles travel at different speeds and mirror at different positions the initial pulse spreads out in space as it advances. Table 4.1 lists the position and the pitch angle at this position determined using equations (4.14) and (4.15) of electrons with initial pitch angles of 30°, 40°, and 50° for the times shown in Figure 4.4. At early times, the peak of the pulse corresponds to the spatial position of the 40° electrons with the width given by the 10° envelope of the injected pulse.

By time t=0.05 seconds a fair fraction of the initial pulse has mirrored and the spread is substantial and not symmetric. The mirroring of particles is clearly seen in Figure 4.5 where the pitch angle distribution is shown at the position of the peaks in Figure 4.4. The pitch angle cosine decreases then goes through zero as the electrons are reflected.

c) Small Pitch Angle Beam Injection

We now compare our numerical solution with the analytic solution equation (3.51). The analytic solution is valid for constant magnetic field and plasma density in the limit that the pitch angle is small. A beam of electrons centered at $s = 10^8$cm is injected with an angular distribution of width $\alpha_0 = 20°$ about the magnetic field and a power law distribution in energy, $f \propto E^{-3.5}\exp(-\alpha^2/\alpha_0^2)$. The magnetic field and plasma density are both constant with the density equal to 10^{11} cm^{-3}. The pulse of electrons propagates down the field spreading in pitch angle and losing energy. The distribution, $f(E,s,t)$ obtained numerically and analytically, is shown in Figures 4.6 and 4.7 for different energies. The distributions are normalized to unity at the peak to provide a close comparison of the two solutions. The numerical solution propagates slightly slower and has larger spatial extent than the analytic solution since the analytic solution assumes $\mu = 1$ in the transport term which prevents the spatial dispersion of the beam. Numerical diffusion also contributes to this spreading. The numerical solution peaks at $s \sim \beta < \mu >$, where $< \mu >$ is the average pitch angle cosine in the pulse. The pitch angle distributions at the peaks of the pulses are shown in Figures 4.8 and 4.9 The higher energy electrons have a narrower distribution because they scatter less. The agreement is good for pitch angles less than $\sim 20°$ and moderate spreading. The analytic solution becomes inaccurate at larger pitch angles and high degrees of spreading due to the small pitch angle assumption.

4.4 - Summary

The evolution of an accelerated particle distribution in a magnetized plasma can be described using a Fokker-Planck equation. We have outlined a technique for numerically solving the time dependent equation, and have written a computer code which solves the equation for electrons undergoing both Coulomb collisions and magnetic mirroring. Other terms can be added to the equation such as inverse Compton, direct electric field, and scattering due to turbulence such as Langmuir and Alfvén waves. The Fokker-Planck terms for these processes are given in chapter 2.

In chapter 6, we use this program to investigate the relative timing of microwaves and hard X-rays in solar flares. Other possible applications include the study of particle acceleration by waves, and the evolution of X-ray spectra in X-ray bursts on neutron stars.

Chapter 4 Figure Captions

Figure 4.1. The analytic (lines) and numerical (circles) solutions evaluated at $E = 20$ keV at $t = 0.15$ s and $t = 0.5$ s for homogeneous injection in a plasma of density 10^{12} cm^{-3}. The initial distribution is $f(E, \mu, s, t = 0) = E^{-3.5}(2\mu^4 - \mu^2 + 1/8)$.

Figure 4.2. Same as Figure 4.1 except $E = 141$ keV.

Figure 4.3. Same as Figure 4.1 except $E = 1$ MeV.

Figure 4.4. The integrated over μ distribution $f(E, s, t)$ versus position for injection into a magnetic trap with magnetic field given by Equation (4.12). The initial distribution is monoenergetic ($E = 1$ MeV) and has pitch angle distribution $\exp(-(\alpha - \alpha_1)^2/\alpha_0^2)$ where α is the electron pitch angle, $\alpha_1 = 40°$, and $\alpha_0 = 10°$. The distribution is given at times t=0.01, 0.03, 0.05, 0.07, and 0.09 s.

Figure 4.5. The pitch angle distribution for injection into a magnetic trap evaluated at the spatial position of the peaks in Figure 4.4.

Figure 4.6. Small pitch angle injection into a plasma of density 10^{11} cm^{-3}. Electrons are injected at $s = 10^8$ cm with spectrum $E^{-3.5} \exp(-\alpha^2/\alpha_0^2)$ with $\alpha_0 = 20°$. The distribution integrated over μ is shown at energy 43 keV and at times t =0.01, 0.03, and 0.05 s.

Figure 4.7. Same as Figure 4.6 except evaluated at $E = 1$ MeV and times t =0.01, and 0.03 s.

Figure 4.8. The pitch angle distribution evaluated at the spatial position of the peak at t =.05 in Figure 4.6.

Figure 4.9. The pitch angle distribution evaluated at the spatial position of the peak at t =.03 in Figure 4.7.

Table 4.1

Electron Trajectories

	$\alpha_o = 30°$			$\alpha_o = 40°$			$\alpha_o = 50°$		
t (sec)	s	α	μ	s	α	μ	s	α	μ
0.00	0.00	30.0	0.866	0.00	40.0	0.766	0.00	50.0	0.642
0.01	2.41	33.7	0.832	2.11	44.3	0.716	1.76	54.3	0.584
0.03	6.48	55.0	0.574	5.28	69.2	0.355	4.04	80.0	0.174
0.05	8.55	82.0	0.139	5.79	100.6	-0.184	3.49	110.9	-0.357
0.07	7.97	109.9	-0.340	3.38	129.1	-0.631	0.49	129.7	-0.639
0.09	4.92	135.5	-0.713	-0.72	139.5	-0.760	-2.85	118.1	-0.471

s is in units of 10^8 cm.

Figure 4.1

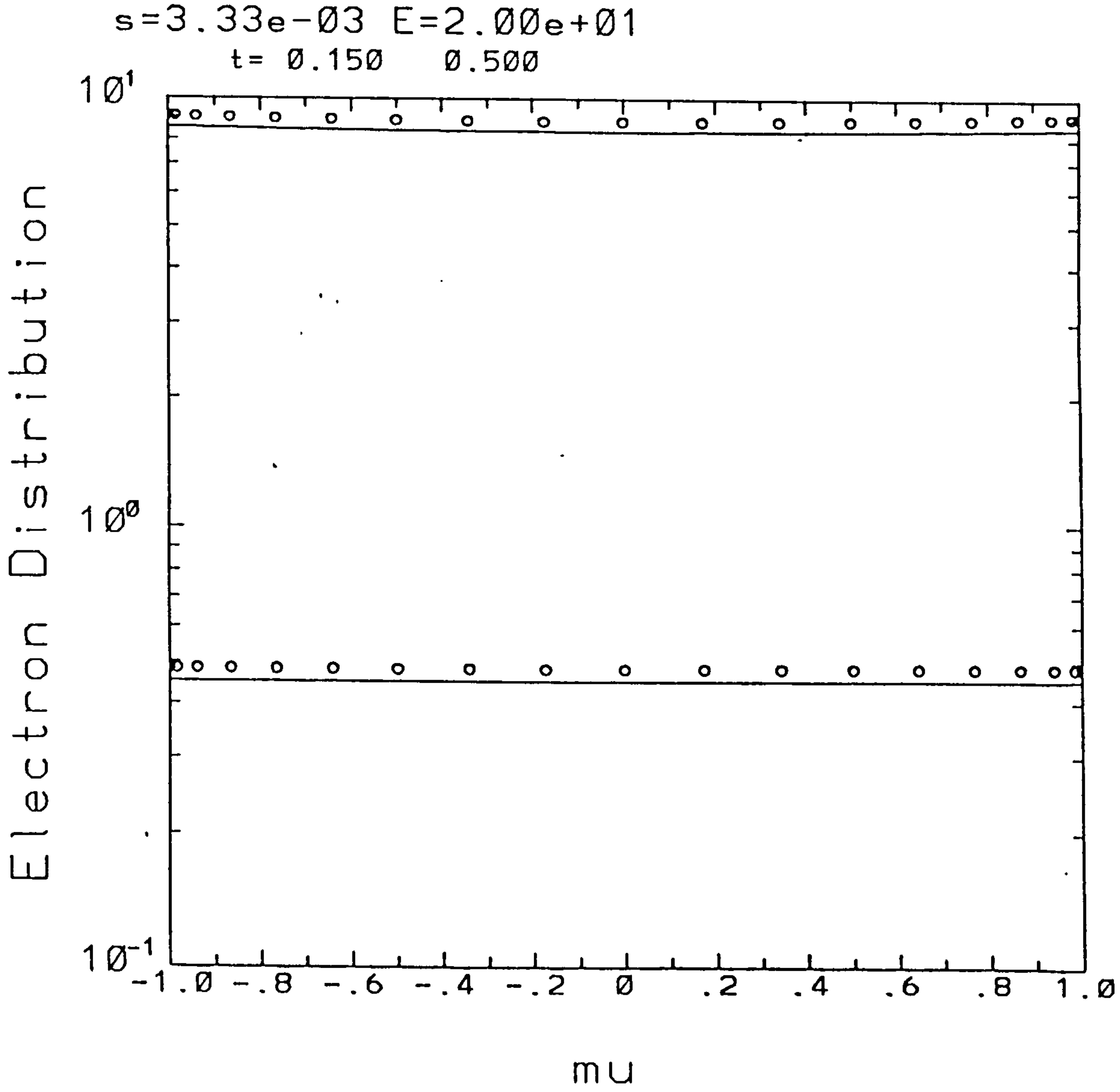
s=3.33e-03 E=2.00e+01
t= 0.150 0.500
10^1
10^0
10^{-1}
Electron Distribution
-1.0
-.8
-.6
-.4
-.2
0
.2
.4
.6
.8
1.0
mu

Figure 4.2

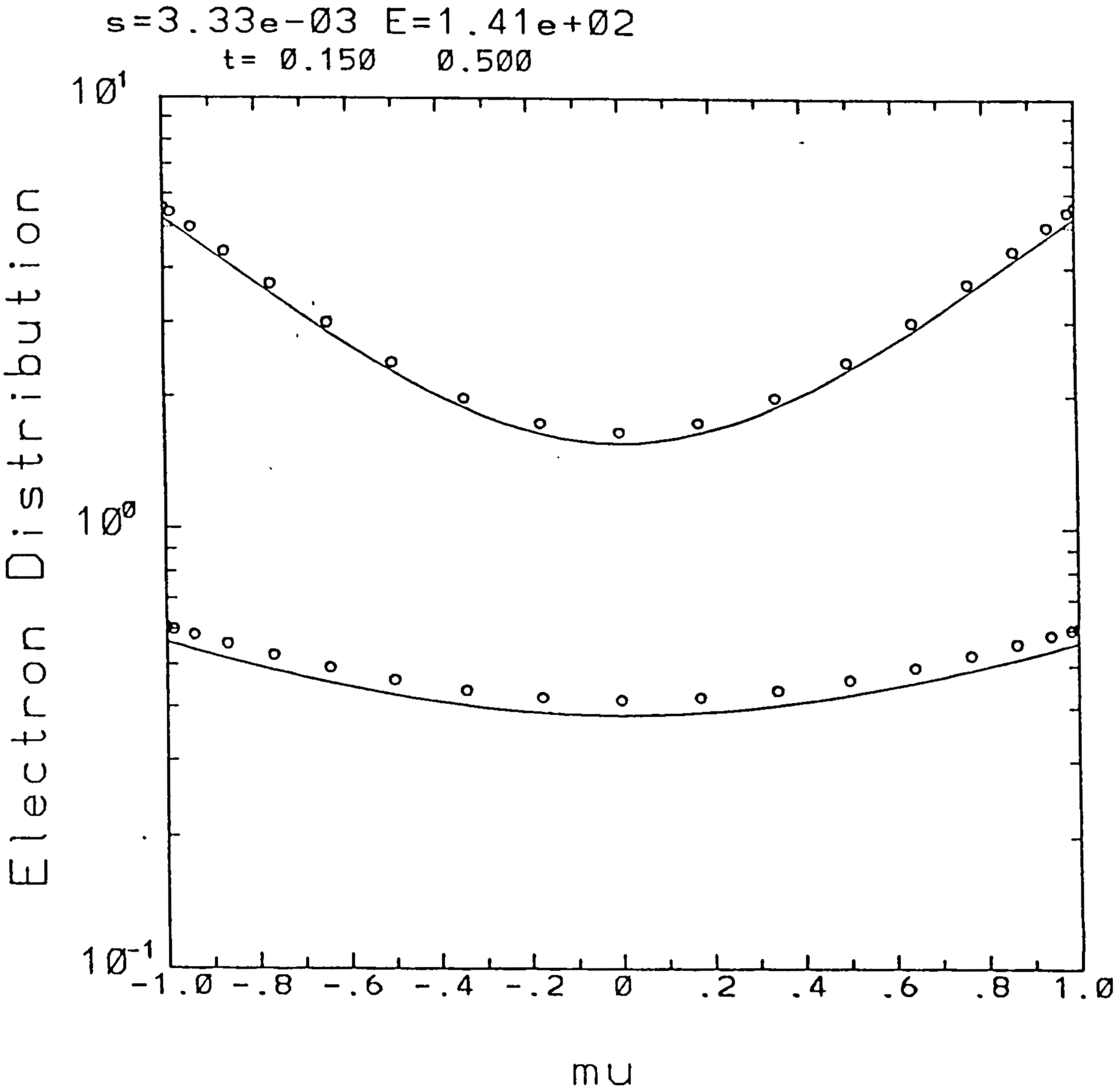
s=3.33e-03 E=1.41e+02
t= 0.150 0.500
10^1
10^0
10^-1
Electron Distribution
-1.0
-.8
-.6
-.4
-.2
0
.2
.4
.6
.8
1.0
mu

Figure 4.3

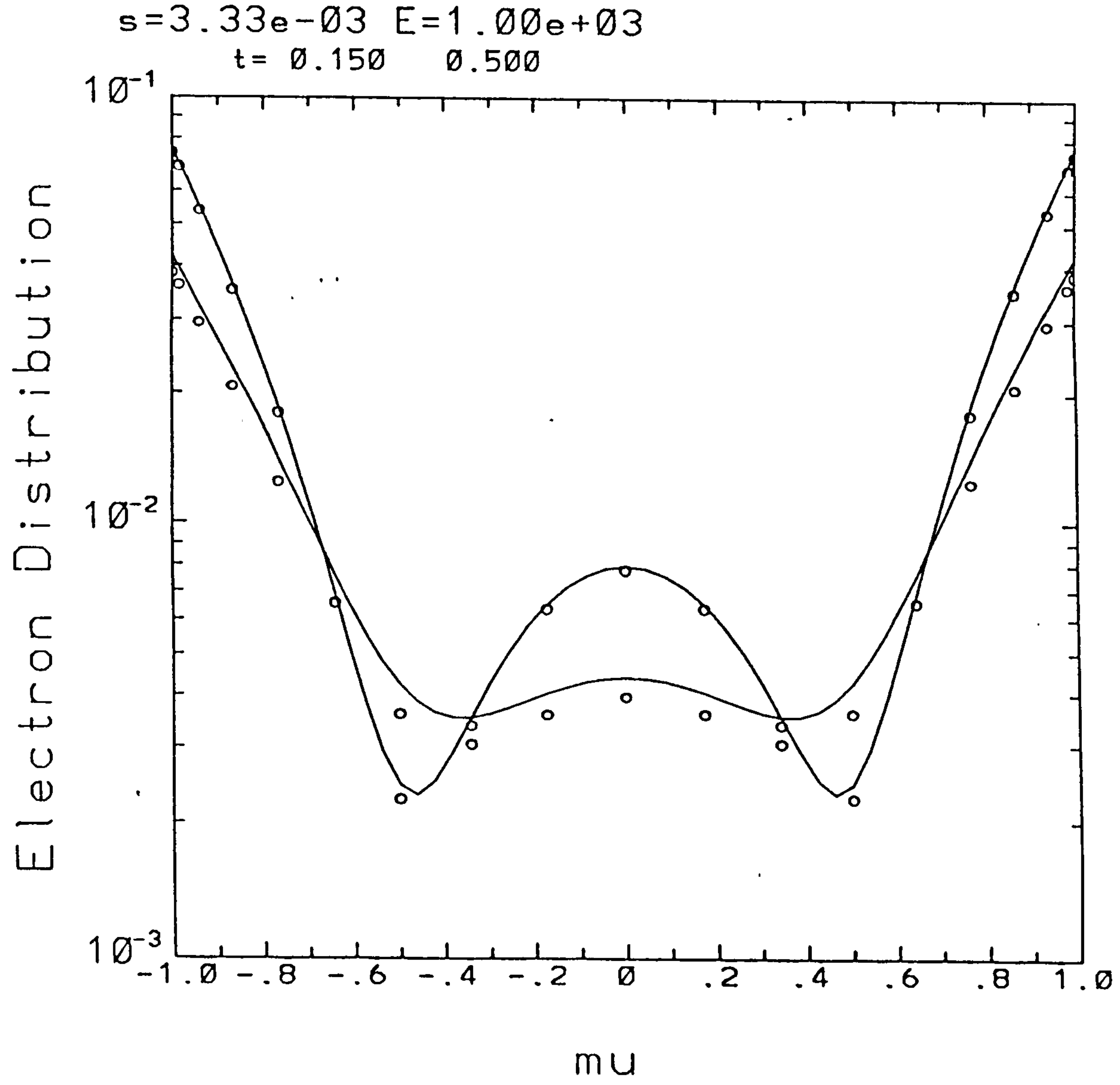
s=3.33e-03 E=1.00e+03
t= 0.150 0.500
10^{-1}
10^{-2}
10^{-3}
Electron Distribution
-1.0
-.8
-.6
-.4
-.2
0
.2
.4
.6
.8
1.0
mu

Figure 4.4

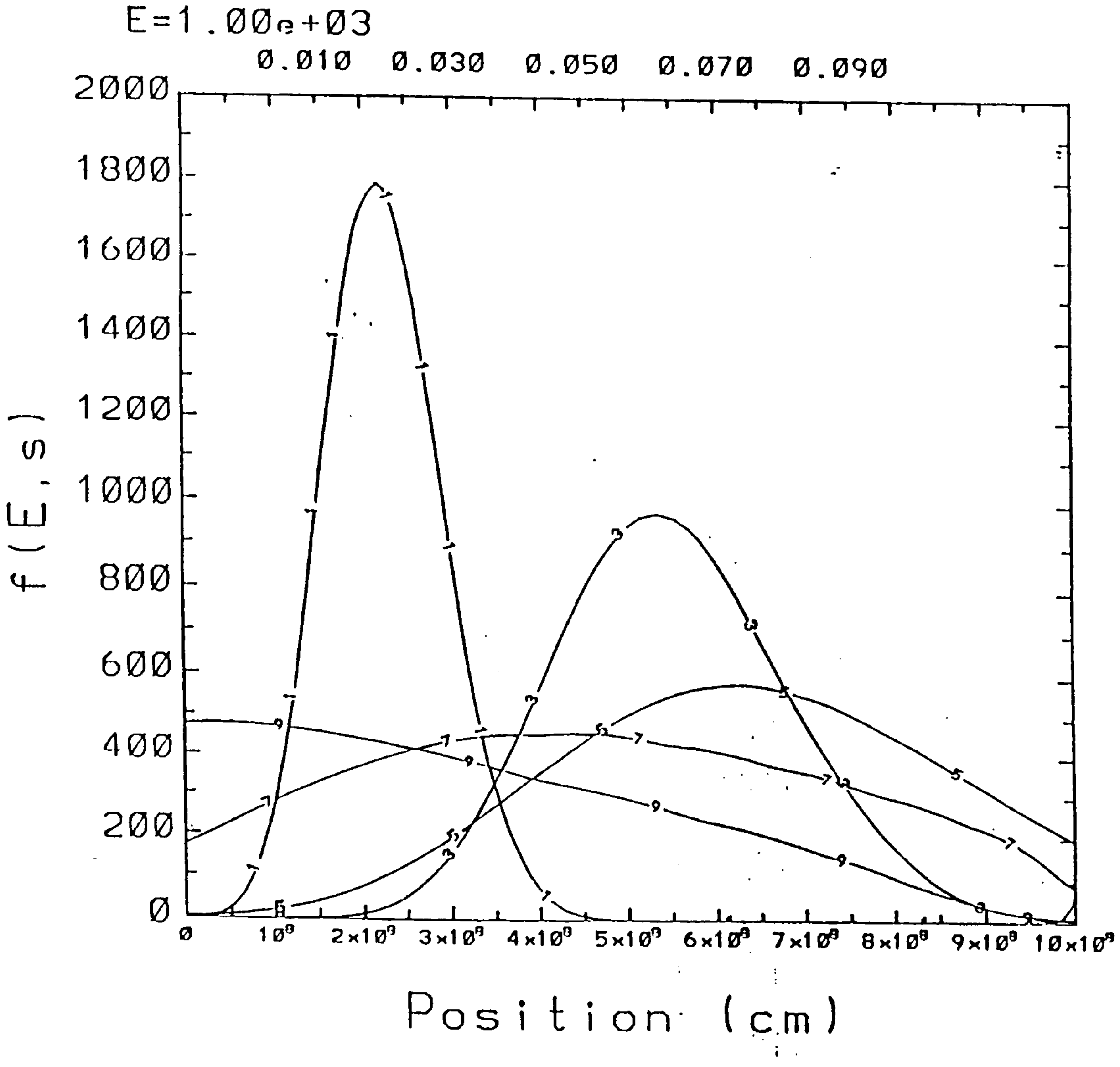
E=1.00e+03
0.010
0.030
0.050
0.070
0.090
f(E,s)
2000
1800
1600
1400
1200
1000
800
600
400
200
0
0
10^9
2×10^9
3×10^9
4×10^9
5×10^9
6×10^9
7×10^9
8×10^9
9×10^9
10×10^9
Position (cm)
1
3
5
7
9

Figure 4.5

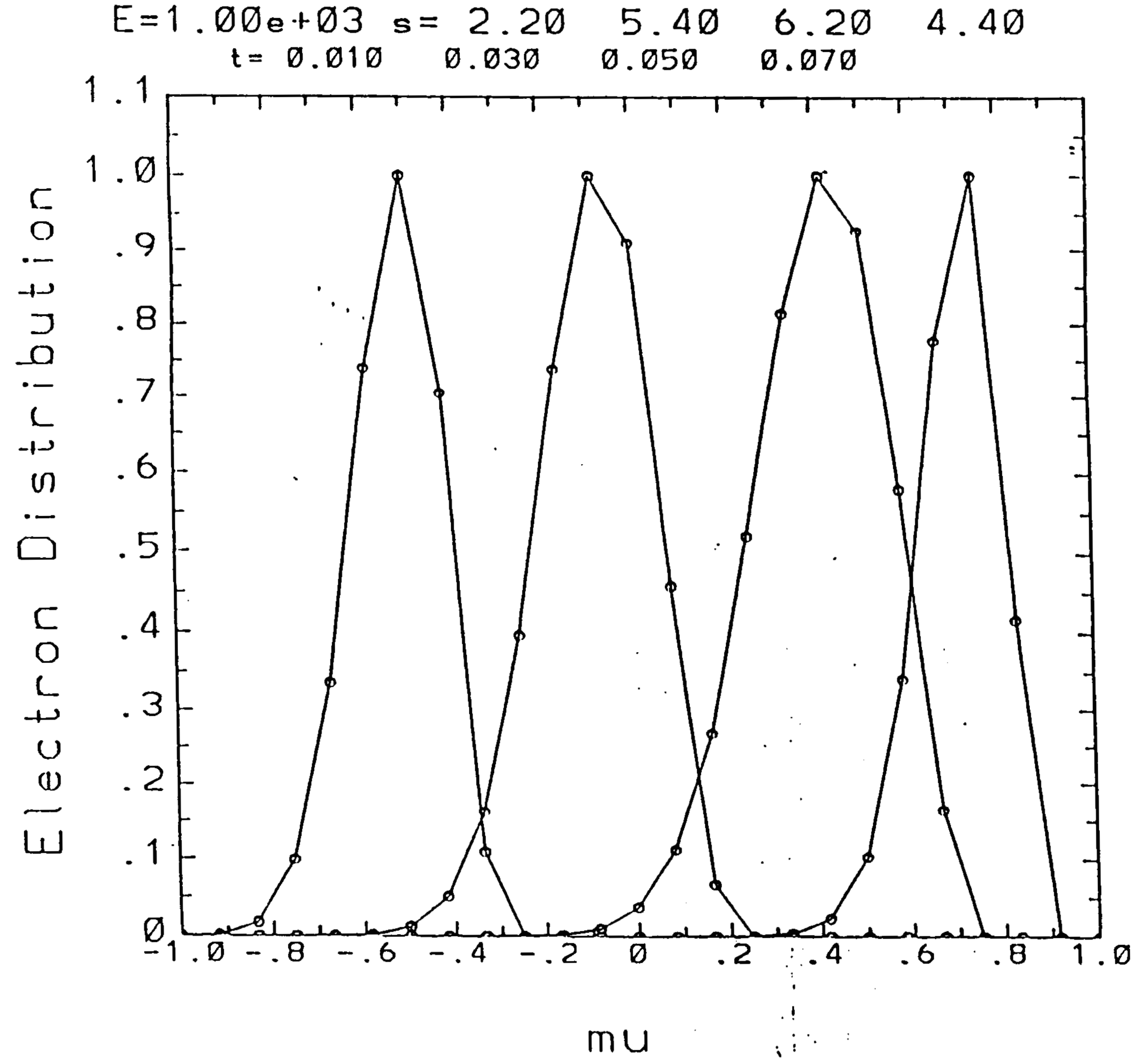
E=1.00e+03 s= 2.20 5.40 6.20 4.40
t= 0.010 0.030 0.050 0.070
1.1
1.0
.9
.8
.7
.6
.5
.4
.3
.2
.1
0
-1.0
-.8
-.6
-.4
-.2
0
.2
.4
.6
.8
1.0
Electron Distribution
mu

Figure 4.6

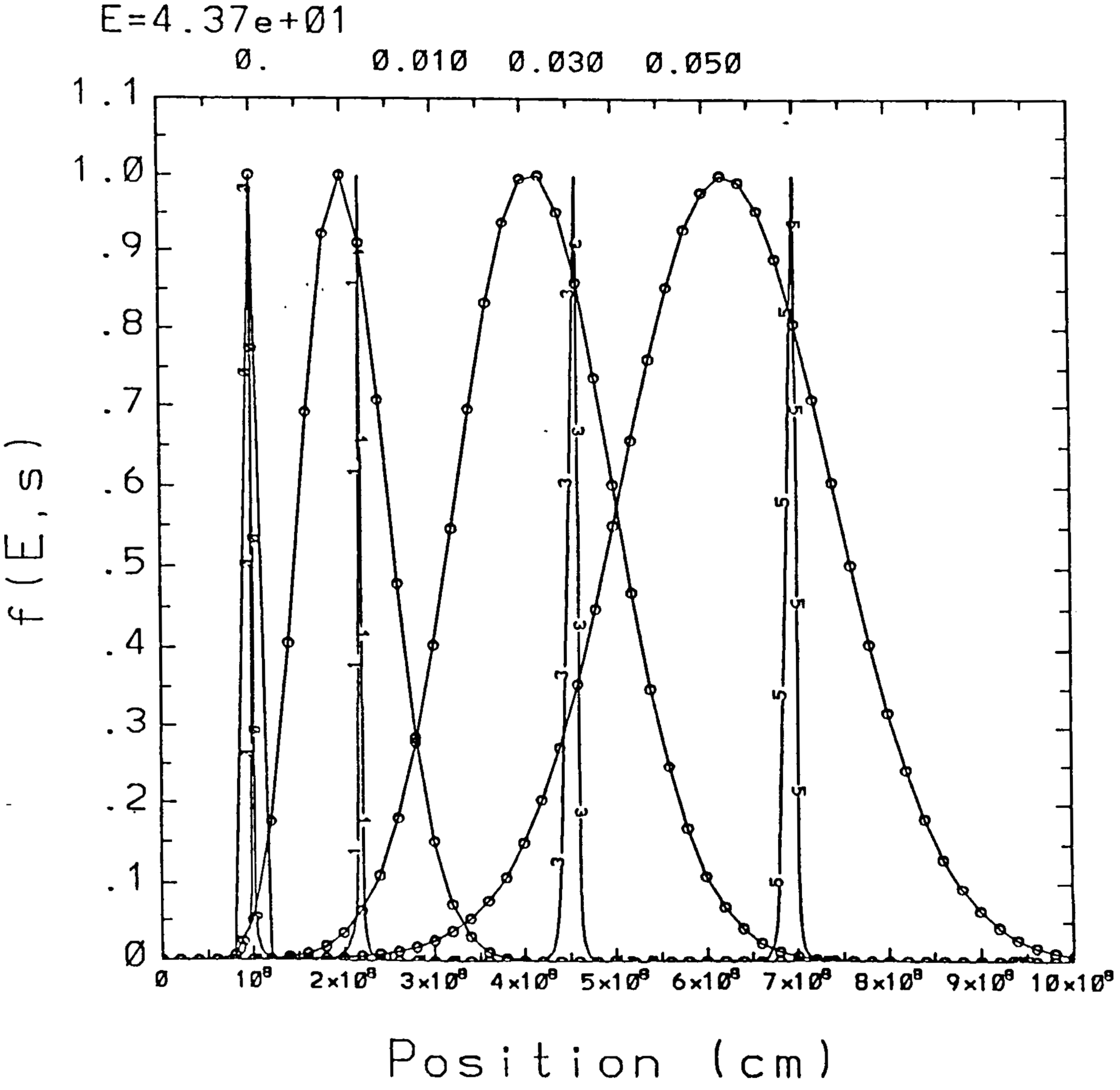

E=4.37e+01
0.
0.010
0.030
0.050
1.1
1.0
.9
.8
.7
.6
.5
.4
.3
.2
.1
0
f(E,s)
0
10⁸
2×10⁸
3×10⁸
4×10⁸
5×10⁸
6×10⁸
7×10⁸
8×10⁸
9×10⁸
10×10⁸
Position (cm)
1
3
5

Figure 4.7

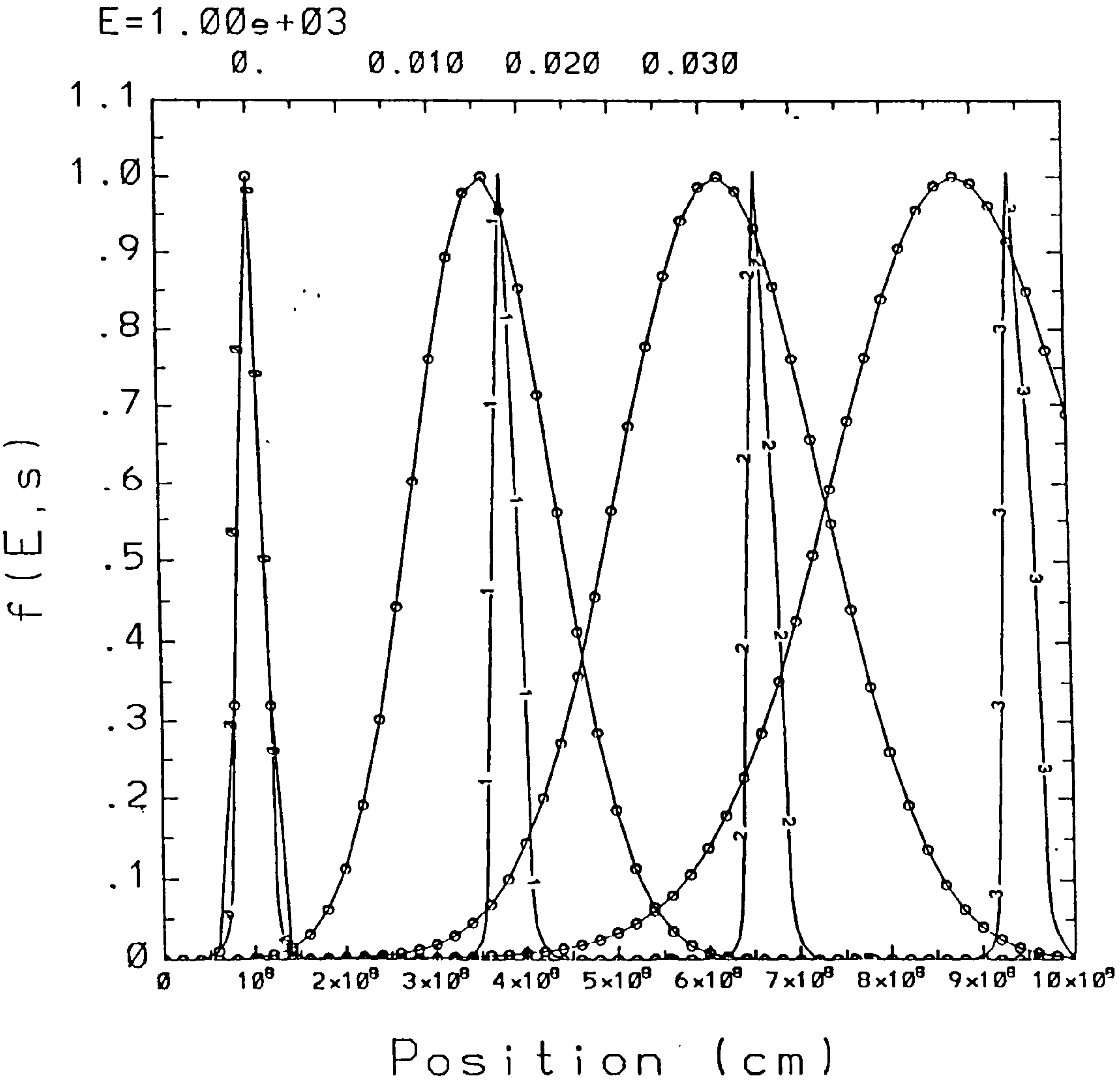
E=1.00e+03
0.
0.010
0.020
0.030
1.1
1.0
.9
.8
.7
.6
.5
.4
.3
.2
.1
0
f(E,s)
0
10^8
2×10^8
3×10^8
4×10^8
5×10^8
6×10^8
7×10^8
8×10^8
9×10^8
10×10^9
Position (cm)
1
2
3

Figure 4.8

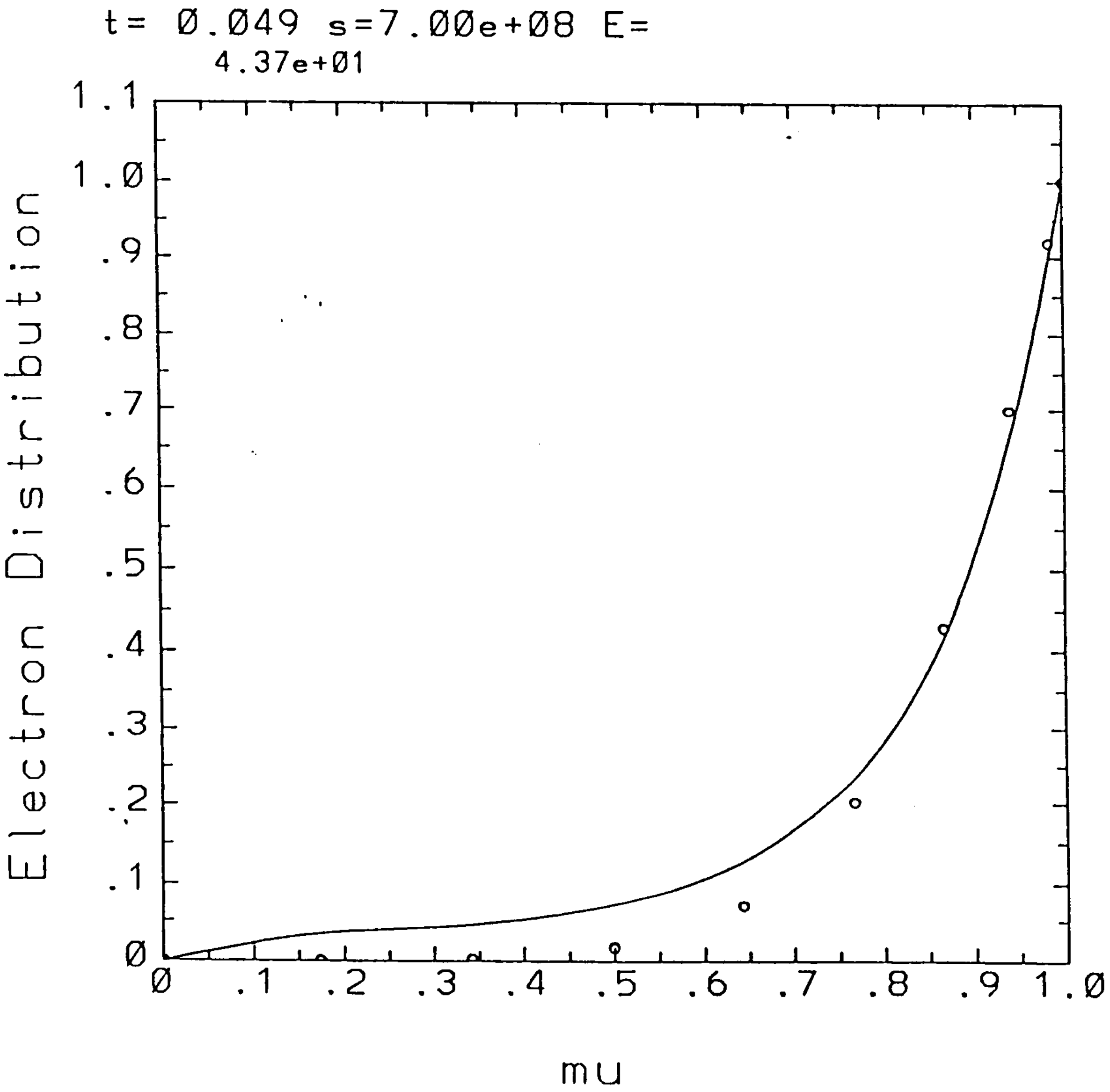
t= 0.049 s=7.00e+08 E=
4.37e+01
1.1
1.0
.9
.8
.7
.6
.5
.4
.3
.2
.1
0
Electron Distribution
0
.1
.2
.3
.4
.5
.6
.7
.8
.9
1.0
mu

Figure 4.9

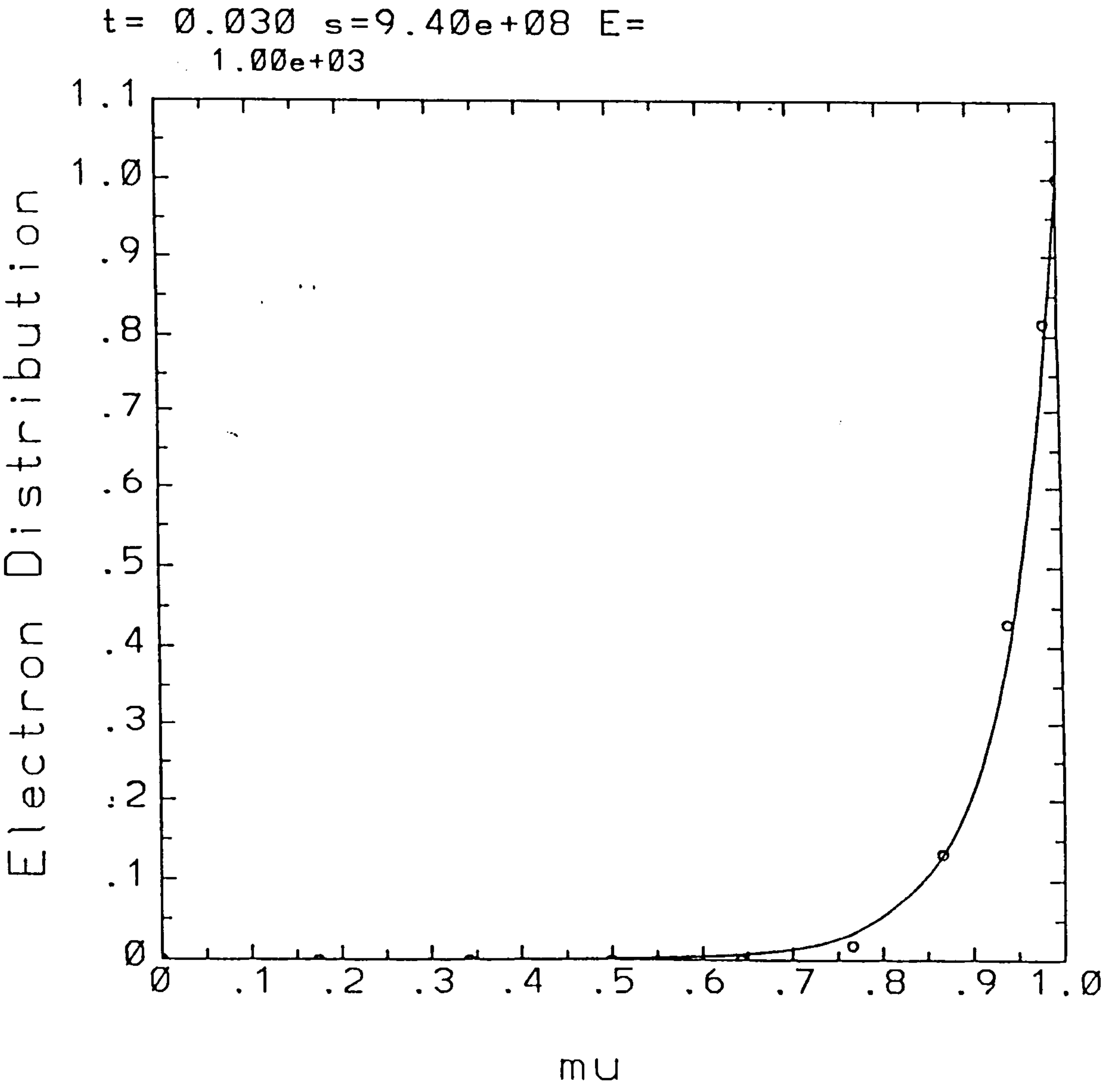
t= 0.030 s=9.40e+08 E=
1.00e+03
Electron Distribution
1.1
1.0
.9
.8
.7
.6
.5
.4
.3
.2
.1
0
0
.1
.2
.3
.4
.5
.6
.7
.8
.9
1.0
mu

CHAPTER 5. THE MICROWAVE TO X-RAY RATIO

5.1 - Introduction

We now turn our attention to the microwave and X-ray emission from accelerated electron distributions in flares. In this chapter we derive relations for the ratio of microwaves to X-rays produced by a population of electrons in thick target, thin target, and multithermal flare models. These calculations take into account the variation of the microwave to X-ray ratio with X-ray spectral index. We then compare the theoretical results with observed ratios of peak microwave and X-ray fluxes for a sample of 51 solar flares with well known spectral index. From this we are able to place constraints upon the geometry of the flaring region. The relations developed in this chapter will also be used in chapter 6 to describe the evolution of microwaves and X-rays from flares over timescales longer than the transport and collisional timescales.

In section 5.2 we define the microwave to X-ray ratio R and discuss the controversy over whether or not a single population of electrons is responsible for both emissions. In section 5.3 we describe the three models and derive the electron spectrum in each model for a given observed X-ray spectrum. Then in section 5.4 we derive the resulting synchrotron spectrum from this electron distribution and give analytic relations for R. Here we give some new formulae for synchrotron emission from semi-relativistic electrons. Finally, in section 5.5 we compare the theoretical microwave to X-ray ratios from these three models with that from 51 observed flares and discuss the implications of this comparison. Section 5.6 provides a summary of this chapter.

5.2 - The Microwave to X-ray Ratio

The similarity between the time profiles of the microwaves and X-rays from solar flares and the good correlation between their peak fluxes (see e.g. Cornell et al

1984, and Kai, Kosugi and Nitta 1985) are strong evidences that the two emissions are produced by the same or a very closely related population of electrons.

However, ever since the first simultaneous observations of microwaves and X-rays from solar flares (Peterson and Winckler 1959), there has been a controversy over the number of non-thermal electrons required to produce the X-ray and the microwave burst (see e.g. Takakura and Kai 1966; Holt and Ramaty 1969; Gary and Tang 1984). Several authors (Peterson and Winckler 1959; Schmahl, Kundu, and Dennis 1985) have claimed that the number of non-thermal electrons inferred from the X-ray burst is about $10^3 - 10^4$ times larger than the number of electrons needed for the production of the microwaves in a given flare. More recently, however, Gary (1985) and Kai (1986) showed that the numbers of electrons deduced from the two emissions are the same.

Some of the discrepancy can be attributed to the neglect of self absorption of the synchrotron radiation (Holt and Ramaty 1969), when the comparison is carried out at low microwave frequency ($< 10\,\mathrm{GHz}$). This still leaves the picture unclear for optically thin synchrotron emission. The problem with using the optically thick flux is that it is very sensitive to the area and spatial geometry of the source. On the other hand, the microwave flux in the optically thin regime is sensitive to the total number of emitting electrons and less so to the geometry of the source. The optically thin microwave flux should therefore be a more reliable source of information when trying to determine whether or not a single population of electrons is responsible for both the microwaves and X-rays. In this optically thin case most of the claims of discrepancy can be attributed to the fact that earlier authors had calculated the electron population from the observed X-ray spectrum using the thin target bremsstrahlung model as opposed to the thick target model (Gary 1985).

The thin target model used by these authors assumes that the high energy electrons responsible for the flare emit both bremsstrahlung X-rays and microwave synchrotron radiation in the same physical region. Thus, the same electron distribution is used when calculating both emissions. We would like to stress however that in a truly thin target situation the mean free path of the electrons is greater than the size of the region where emission takes place, which is very unlikely.

It is now widely agreed that the accelerated electrons find themselves mostly on closed magnetic loops so that they are eventually stopped in the chromospheric plasma. If the electrons are accelerated at substantially high altitudes above the chromosphere, they essentially travel freely along the field lines in the corona. Once in or below the high density chromosphere they quickly (in a short distance) lose their energy. For the same reason most of the bremsstrahlung X-rays are also emitted from the latter region while the microwaves come primarily from coronal regions where the electrons spend most of their lifetime. This will not be true if the magnetic field increases as rapidly as the density below the chromosphere. This, however, is not believed to be the case. Thus, while the same electron population is responsible for both X-rays and microwaves, the emissions come from different physical regions. The microwaves are produced in the coronal portion of the loop by a spectrum of electrons which is essentially the same as that of the accelerated electrons, while X-rays originate in the chromosphere from the harder thick target electron spectrum.

Multithermal models have also been proposed to explain the hard X-ray emission from flares (Brown 1974, Dulk and Dennis 1982). Here the X-rays come from thermal bremsstrahlung from a multitemperature plasma with temperatures above 10^8 K. The microwave emission is then the sum of many thermal synchrotron spectra. Dulk and Dennis (1982) have used such a model to explain hard X-rays and the optically thick part of the microwave spectrum.

In this chapter we compare the observed microwave and X-ray fluxes of flares with the theoretical expectations of the three models mentioned above in order to clarify the situation and set constraints on the model parameters such as plasma density, magnetic field and flaring loop sizes. We make this comparison for a statistical sample of flares instead of a single flare, which has been carried out frequently in the past. More importantly however, instead of just considering the correlation between X-ray and microwave fluxes, we consider the observed variation of the ratio of the fluxes with the X-ray spectral index, and compare this with the predictions of the models. It turns out that the inclusion of the spectral index information provides strong constraints because, as we shall see, the ratio of the fluxes is a sensitive function of the spectral index.

The X-ray observations we use will be the peak fluxes (all fluxes will be as measured at the source, not at the Earth) and spectral indices of flares with a well defined power law spectrum:

$$dJ_x(k) = \left(\frac{F_x(k_0)}{k_0^2}\right)(\gamma - 2)(k/k_o)^{-\gamma} dk \, \text{photon s}^{-1}, \tag{5.1}$$

where k is the photon energy and $F_x(k_0)$ is the total photon energy flux above energy k_0. Throughout this paper, all energies are given in units of $m_e c^2$ unless otherwise specified.

For each model, we invert the photon spectrum to obtain the spectrum of the bremsstrahlung radiating electrons. This inversion depends upon the angular distribution of the photons and the electrons. In the absence of knowledge of the spatial or angular distribution of the X-rays, we must assume an angular distribution for the radiating electrons. For $k_0 \ll 1$, the X-ray flux will be approximately isotropic. We will also assume that the electron distribution is isotropic. In general, a power law photon flux implies that the effective spectrum of the electrons is also a power law. Assuming the same spectrum extends to higher energies, we then calculate the expected optically thin synchrotron radiation at a specified frequency for each model and for various values of the magnetic field B. This extrapolation needs some scrutiny, especially for low values of B because the energy of the electrons producing the microwaves is much larger (possibly relativistic) than those (non-relativistic ones) producing the X-rays. We shall return to the observational evidence for or against this assumption and comment on its effects. Given the synchrotron flux $S(\nu)$, we then compute the dimensionless ratio

$$R(\gamma, B, \nu) = \frac{\nu S(\nu)}{F_x(k_0)}, \tag{5.2}$$

and compare it with observations.

5.3 - Electron Distributions

We believe, and it is widely accepted, that the most likely model for production of the power law impulsive X-ray flux of a flare is the non-thermal thick target model. The presence of the magnetic fields and their closed loop structures dictate this conclusion. Accelerated non-relativistic or semi-relativistic electrons in such a configuration will lose most of their energy via Coulomb collisions in the thick target high density chromosphere with a well-defined yield of bremsstrahlung X-rays. If the field lines are open to the interplanetary medium, electrons with pitch angles directed downward will behave as above. Those electrons directed outward will lose some energy due to collisions and radiate X-rays as in a thin target model, but escape with most of their energy and with their initial distribution intact. The thin target X-rays will be dominate only if the majority of the accelerated electrons are directed outward. This seems unlikely because i) it necessarily implies a much lower X-ray yield and much larger total energy for the accelerated electrons, and ii) the number of outgoing electrons observed directly near the Earth and that deduced from type III bursts is much less than those needed for production of the X-rays.

Nevertheless, for purposes of comparison we will also consider the thin target and thermal models. The thermal models we consider are multitemperature because of the power law spectrum of the X-rays. We should note at the outset that because there are many parameters in the models, any model can be brought into agreement with observations with proper adjustment of these parameters. The question is then which set of required parameters are reasonable and acceptable based on other observations or theoretical arguments. As we shall see, the thick target model implies a more reasonable set of flare plasma parameters than the other two models.

We note here that most of the equations cited below are not new and have been in the literature for some time now. But for completeness we present them here with the briefest descriptions. We will assume the electrons are non-relativistic in describing the X-ray emission. This is an excellent approximation as long as we restrict ourselves to X-ray energies less than ~ 100 keV.

(a) Non-thermal Thick Target Models

Here we assume that the accelerated electrons are injected at the top of a symmetric coronal loop at a steady rate (i.e., for a time longer than their lifetime) with the flux

$$dJ_e(E) = \frac{F_e(E_0)(\delta' - 1)}{E_0^2}(E/E_0)^{-\delta'-1} dE\,\mathrm{s}^{-1}, \tag{5.3}$$

where $F_e(E_0)$ is the total energy flux of electrons with energy greater than E_0.

For the purpose of calculation of spatially unresolved X-rays, it is unimportant where the X-rays are emitted. Following Petrosian (1973) we can write for the X-ray flux given in equation (5.1)

$$F_x(k_0) = F_e(E_0)Y(k_0), \tag{5.4}$$

where $Y(k_0)$ is the yield of X-rays with energies $> k_0$ by electrons with energies $> E_0$. In what follows we set $k_0 = E_0$. For the power law distribution of equation

(5.3)

$$Y(E_0) = \frac{16}{3}\left(\frac{\alpha}{4\pi \ln \Lambda}\right) E_0 \left(\frac{2}{\delta'}\right)^2 \left(\frac{1}{\delta' - 2}\right), \tag{5.5}$$

where $\delta' = \gamma$ the photon spectral index, α is the fine structure constant and $\ln \Lambda \approx 22$ is the Coulomb logarithm (note that our $\ln \Lambda$ here is defined to be one half of the definition used in Petrosian 1973). From equations (5.4) and (5.5), we find

$$F_e(E_0) = \frac{3}{64}\left(\frac{4\pi \ln \Lambda}{\alpha}\right)(\gamma - 2)\gamma^2 E_0^{-1} F_x(E_0), \tag{5.6}$$

which along with equation (5.3) relates the electron spectrum to the observed spectral index γ and flux $F_x(E_0)$ of the X-rays.

Electrons of energy E lose most of their energy after they have traversed a column depth $N(E) = 5 \times 10^{22}(E^2/(E+1))\,\mathrm{cm}^{-2}$ (see Leach and Petrosian 1981) and emit mainly X-rays of energy $k \lesssim E$. We are interested in particles with $E \gtrsim E_0 = 25$ keV which penetrate column depths greater than of order $10^{20}\,\mathrm{cm}^{-2}$. If the column depth of the coronal portion of the loop (from the top of the loop to the transition region) $N_{tr} < 10^{20}\,\mathrm{cm}^{-2}$, most of the X-rays will be radiated below the transition region. More importantly, however, the microwave producing electrons will have much larger energy (even $E \gtrsim 1$ for low fields, see below) and therefore will be completely unaffected by collisions in the corona. The spectrum of electrons above the transition region will then be given by

$$f(E)dE = \frac{L}{\beta c \bar{\mu}} dJ(E) = \left(\frac{3\pi L \ln \Lambda}{16 \alpha c \bar{\mu}}\right) \frac{F_x(E_0)}{\beta E_0^3}(\gamma - 2)(\gamma - 1)\gamma^2 \left(\frac{E}{E_0}\right)^{-\gamma-1} dE, \tag{5.7}$$

where L is the length of the loop above the transition region and $\bar{\mu}$ is the average pitch angle throughout the loop. Below the transition region the flux of the non-thermal particles decreases quickly (within a few density scale heights H_n) because of the rapid increase in plasma density (see e.g., Leach and Petrosian 1981).

The synchrotron flux could be related to the injected electron flux by calculating the thick target synchrotron yield. This, however, requires a knowledge of the variation of magnetic field and density along the loop and the geometry of the loop. In the absence of such detailed information we make the approximation that the total synchrotron flux is due to the electrons in the coronal portion of the loop since the number of particles above the transition region will be far larger than the number of particles below the transition region. Because the flux of particles below the transition region is less than that above it, the synchrotron contribution from that region will be less by a factor of $\sim (H_n/L) \ll 1$. This assumes a uniform B field. Although the B field is expected to be higher in the chromosphere than in the corona, this increase is not sufficient to affect the above inequality. Also, for an isotropic electron distribution, the synchrotron emission is peaked in a direction perpendicular to the magnetic field and decreases to zero in the direction parallel to the magnetic field. For loops not situated near the solar limb, the angle between the line of sight and the local magnetic field, and therefore the microwave emissivity is greatest at the top of the loop and smallest at the base of the loop. Consequently, we will ignore the synchrotron emission below the transition region and we use the distribution given in equation (7) to calculate the synchrotron emission from this model.

(b) Non-thermal Thin Target Models

In a thin target model the X-rays and microwaves are both produced by electrons of instantaneous energy spectrum $f(E)$. We will assume an isotropic electron momentum distribution. Using the well known thin target formula (see e.g. Brown 1971, Lin and Hudson 1976) one can relate the electron spectrum to the observed X-ray spectrum of equation (5.1). However, we follow the same procedure used in Petrosian (1973, equation 29) to calculate the thick target spectrum since this approximation leads to a simpler analytic expression without loss of much accuracy. From this we find for the thin target case in the non-relativistic limit

$$f(E) = \frac{3\sqrt{2}}{64} \frac{(\gamma-2)(\gamma-1)\gamma}{\alpha r_0^2 c n_0} \frac{F_x(E_0)}{E_0^{3/2}} \left(\frac{E}{E_0}\right)^{-\gamma+1/2} , \tag{5.8}$$

where r_0 is the classical electron radius and n_0 is the background plasma density. In this model the same distribution of electrons also produces the microwave radiation via synchrotron emission in a magnetic field of strength B. It should be noted that these thin target calculations are also applicable to thick target situations where the electrons lose energy in the same region where they emit both the microwaves and X-rays.

(c) Thermal Models

As mentioned above, a single temperature plasma does not give rise to a power law bremsstrahlung spectrum. However, as shown by Brown (1974), a multi-temperature plasma can produce a power law bremsstrahlung spectrum if the emission measure distribution $n^2(T_*)V(T_*)dT_*$ has a power law dependence on temperature parameter $T_* \equiv k_B T/m_e c^2$. Here n and V are the density and volume of a plasma element of temperature T and k_B is the Boltzmann constant. By integration of the thermal bremsstrahlung spectum over all temperature it can be shown that the X-ray spectrum of equation (5.1) can be produced by an emission measure distribution

$$n^2(T_*)V(T_*) = \frac{3\sqrt{6}}{32\sqrt{\pi}} \frac{1}{\alpha c r_0^2} \frac{(\gamma-2)}{\Gamma(\gamma-1)} \frac{F_x(E_0)}{E_0^{3/2}} \left(\frac{T_*}{E_0}\right)^{-\gamma+1/2} , \tag{5.9}$$

where Γ is the gamma function. The total electron energy spectrum is then the sum of many Maxwell-Boltzmann distributions weighted by the product nV.

$$f(E) = \frac{2}{\sqrt{\pi}} E^{1/2} \int_0^\infty T_*^{-3/2} e^{-E/T_*} n(T_*)V(T_*) dT_* \tag{5.10}$$

It is clear that some additional assumption is needed in order to relate the electron distribution to the observed X-ray spectrum. Two common assumptions are constant pressure $n(T_*) = n_0 E_0/T_*$ (Brown 1974) or constant density $n(T_*) = n_0$ (Dulk and Dennis 1982). Note that in the constant pressure case n_0 is the density at temperature $T_* = E_0$. From equations (5.9) and (5.10) we then obtain

$$f(E) = \frac{3\sqrt{6}}{16\pi}\left(\frac{\gamma-2}{\alpha c r_0^2 n_0}\right)\frac{\Gamma(\gamma-1/2\pm1/2)}{\Gamma(\gamma-1)}\frac{F_x(E_0)}{E_0^{3/2}}\left(\frac{E}{E_0}\right)^{-(\gamma-1\pm1/2)}, \tag{5.11}$$

with the (+) sign for the constant density case and the (−) sign for the constant pressure case.

In summary, the total electron distribution inferred from the X-ray spectrum of equation (5.1) in the three models can be written as

$$f(E) = \left(\frac{3\pi}{16\sqrt{2}}\right)\left(\frac{1}{\alpha c}\right)\left(\frac{F_x(E_0)}{E_0^{7/2}}\right)h(\gamma)\left(\frac{E}{E_0}\right)^{-\delta}, \tag{5.12}$$

where

$$\delta = \begin{cases} \gamma + 3/2 & \text{thick target} \\ \gamma - 1/2 & \text{thin target} \\ \gamma - 1 \pm 1/2 & \text{thermal} \end{cases} \tag{5.13}$$

and

$$h(\gamma) = \begin{cases} \left(\frac{L\ln\Lambda}{\bar{\mu}}\right)(\gamma-2)(\gamma-1)\gamma^2 & \text{thick target} \\ \left(\frac{1}{\pi}\right)\left(\frac{1}{n_0 r_0^2}\right)E_0^2(\gamma-2)(\gamma-1)\gamma & \text{thin target} \\ \left(\frac{2\sqrt{3}}{\pi^2}\right)\left(\frac{1}{n_0 r_0^2}\right)E_0^2\frac{\Gamma(\gamma-1/2\pm1/2)}{\Gamma(\gamma-1)}(\gamma-2) & \text{thermal} \end{cases} \tag{5.14}$$

Note that for the thick target case we have used the non-relativistic approximation $\beta = (2E)^{1/2}$. We will discuss the validity of this and other approximations in the next sections when we calculate the expected microwave emission from these models and compare them with observations.

5.4 - Microwave Emission

In evaluating the microwave spectrum the non-relativistic assumptions used so far are no longer applicable. The simple and well known ultra-relativistic synchrotron emissivity formula are also not accurate for the semi-relativistic regime we are concerned with here. We will make use of expressions derived by Petrosian (1981) for these energy ranges. In that paper various approximate expressions with varied complexity and accuracy are given for the synchrotron emissivity. These approximations are valid for high harmonics, i.e. at frequencies $\nu \gg \nu_b = eB/2\pi m_e c$. The most accurate result is obtained when the integration over the particle energies equation (P.8) is carried out numerically (equations preceeded by P refer to Petrosian 1981). We have compared the results of this integration with the detailed numerical evaluations using the sums over Bessel functions (cf. e.g. Bekefi 1966). We find excellent agreement.

The integration can also be carried out analytically using the method of steepest descent, leading to equation (P.11). This expression requires the solution of a transcendental equation and is too complicated for our purposes here. However, for high harmonics ($\nu \gg \nu_b$) an approximation similar to the ultra-relativistic approximation is possible. With this approximation, the synchrotron flux in the optically thin regime in $m_e c^2$ s^{-1} Hz^{-1} from an isotropic electron distribution $f(E)$ is given by

$$S(\nu) = \left(\frac{2\pi^2 r_0 \nu_b}{c}\right)\left(\frac{\nu \sin\theta}{\nu_b}\right)^{1/2} f(E_1) X \exp[d\ln(f/\gamma)/d\ln\gamma^2 \,|_{\gamma=E_1+1}] \quad (5.15)$$

where θ is the angle between the magnetic field and the line of sight, $\gamma = E + 1$ is the Lorentz factor, and E_1 is the energy of the electrons with the largest contribution to the emission at frequency ν. The function X depends upon the electron distribution and the harmonic number, but for the power law distribution we will consider, it takes on a particularly simple form. Equation (P.34) evaluates the flux for a power law electron spectrum of spectral index δ in the limit of high harmonics and relativistic electrons. However, it does not yield a very accurate expression at moderate harmonics, especially for steep spectra ($\delta \gtrsim 5$) such as are encountered in the present work. The principle error introduced in equation (P.34) is in assuming that $(\gamma_1 - 1) = E_1 \gg 1$ when substituting into equation (5.15). We have found that simply by not making this assumption when substituting into $f(E_1)$ in equation (5.15) but otherwise using (P.34), we obtain surprisingly good results in this intermediate regime. We therefore set

$$\gamma_1^2 = \frac{4\nu}{3\nu_b \delta \sin\theta} \text{ and, } X = (1+\delta)^{-1/2}, \tag{5.16}$$

in which case we find for the power law electron distribution of equation (5.12)

$$S(\nu) = \left(\frac{2\pi^2 r_0 \nu_b \sin\theta}{c}\right)\left(\frac{\nu}{\nu_b \sin\theta(\delta+1)}\right)^{1/2} \exp\left(-\frac{\delta+1}{2}\right) f(E_1). \tag{5.17}$$

Figure 5.1 shows a comparison of this expression with the numerically integrated emissivity equation (P.8). As can be seen (5.17) provides a satisfactory approximation. However, for steep spectra and at large B field such that $\nu/\nu_b\delta$ approaches unity, this approximation overestimates the emissivity. Because many authors have used and continue to use the empirical fits to the synchrotron emissivity by Dulk and Marsh (1982) we also plot the ratio of their expression to the numerical values. It is evident that even though their empirical expression provides a satisfactory approximation within the range of parameters tested by them, outside this range at low ν/ν_b and steep spectra it diverges away from the correct value faster than our result. The main purpose of figure (5.1) is to indicate that caution is needed when using either the simplest analytic formula of Petrosian or the empirical fits of Dulk and Marsh (1982).

Now finally the ratio R as defined in equation (5.2) becomes

$$R = \left(\frac{3\pi^3 r_0 \nu_b^2 \sin^2\theta(\delta+1)}{8\sqrt{2}\alpha c^2 E_0^{7/2}}\right)\left(\frac{\nu}{\nu_b \sin\theta(\delta+1)}\right)^{3/2} h(\gamma)\exp\left(-\frac{\delta+1}{2}\right)\left(\frac{E_1}{E_0}\right)^{-\delta}, \tag{5.18}$$

where $h(\gamma)$ and δ are as given in equations (5.13) and (5.14) and

$$E_1 = \left(\frac{4\nu}{3\nu_b\delta\sin\theta}\right)^{1/2} - 1 = 9.0\left(\frac{\nu}{17\,\mathrm{GHz}}\right)^{1/2}\left[\left(\frac{B}{100\,\mathrm{G}}\right)\delta\sin\theta\right]^{-1/2} - 1. \tag{5.19}$$

We will use a single value of θ when comparing expression (5.18) to the observations. However, in reality the angle θ will vary with position along the loop unless the magnetic field is straight. Thus, the value of θ we use will correspond to an average angle weighted by the emissivity at each point on the loop. Therefore there will be some δ dependence to θ which depends upon the geometry and orientation of the loop. We will not however include this dependence since the geometry of the loop is unknown and since the variation of the synchrotron flux due to the explicit dependence on δ is much greater.

5.5 - Comparison With Observations

We have analyzed a sample of 53 flares with observations in both hard X-rays and microwaves for which the X-ray spectral index is known. The flares were observed in X-rays by the Hard X-ray Burst Spectrometer (HXRBS) aboard the *SMM* satellite (Dennis et al 1985). From the HXRBS observations we obtain the integrated hard X-ray flux at distance D at the Earth, $F_x(25\,\text{keV})/4\pi D^2$ above 25 keV, and the photon spectral index γ (which were kindly provided by Brian Dennis). The microwave observations were made at 17 GHz by Nobeyama observatory (Kosugi and Shiomi 1983). These flares are all the flares for which we had the X-ray spectral index and which also appeared in the listing of microwave flares observed at Nobeyama. These data are summarized in Table 5.1. Included in this table is the *SMM* flare number, the integrated X-ray flux $F_x(25\,\text{keV})/4\pi\text{D}^2$ in ergs s^{-1} cm^{-2}, the microwave flux $S(17\,\text{GHz})/4\pi\text{D}^2$ in SFU= $10^{-19}\,\text{ergs}\,\text{s}^{-1}\,\text{cm}^{-2}\,\text{Hz}^{-1}$, and the value of the ratio R. We have plotted the ratio R for these flares versus the spectral index γ in Figure 5.2. We have excluded from this and following figures two of the flares with very steep spectra ($\gamma > 9$) such that a power law spectrum is questionable. On the same graph we have plotted the theoretical curves of R for magnetic field strengths of 350, 450, 550, and 650

G for the nonthermal thick target model with a loop length $L = 2 \times 10^9$ cm at a viewing angle of $\theta = 70°$. We have assumed isotropic injection in the downward hemisphere so that $\bar{\mu} = 0.5$. From VLA imaging observations (Schmahl, Kundu, and Dennis 1985) and from theoretical arguments (Lu and Petrosian 1988), a loop length of order 10^9 cm is a reasonable value for L. As can be seen, the thick target model explains the data very well with these parameters for a small range of magnetic field strengths between 350 and 650 Gauss. Note though that the data could also be explained with a single value of magnetic field ($\sim 550\,\mathrm{G}$) but with varying loop length and viewing angle.

For comparison, in figure 5.2 we have also plotted R where we have numerically integrated equation (P.8) for the distribution given in equation (5.7). Note that R actually increases with γ at large γ and large B. This is because for very steep spectra the X-ray yield decreases rapidly with γ since many of the bremsstrahlung photons will be emitted at energies below E_0. On the other hand for large δ and B, the synchrotron flux becomes less dependent upon δ because more of the emission comes from lower harmonics.

We can see the effect of having replaced a factor of β in equation (5.7) by $(2E)^{1/2}$ when calculating the electron distribution in the loop for the thick target model. We underestimate the value of R in equation (5.18) when the characteristic energy of the microwave emitting electrons E_1 becomes relativistic. As is evident from equation (5.19), the value of E_1 increases with decreasing B and γ; $E_1 \approx 1.3$ at $B = 400$ G and $\gamma = 3$. We therefore make an error of a factor of ~ 1.5 in β. As can be seen in figure 5.2, the analytic expression underestimates R at low values of spectral index. This error however, decreases for larger B and steeper spectra.

At steeper spectra, the error is due to the analytic approximation to the synchrotron emissivity we have used. As can be seen from figure 5.1 and figure 5.2, our approximation overestimates the emissivity at large B and steep spectra.

At 650 G and $\delta = 8$, corresponding to $\gamma = 6.5$, the analytic expression is too large by a factor of 4. However, for our purposes the analytic expression will suffice. As can be seen from figure 5.2, the analytic expression equation (5.18) provides a satisfactory approximation to R. The errors introduced are within the uncertainties associated with the loop length, the viewing angle, and the magnetic field.

In figure 5.3, along with the same observations we show the theoretical values of R for the thin target case with density $n_0 = 10^{11}\,\mathrm{cm}^{-3}$. The curves of R for the multithermal constant density case are almost identical to those of the thin target case. This is because the thin target model and the multithermal constant density model both describe the same physical situation. Both models have a population of electrons emitting bremsstrahlung radiation in a constant density plasma. Not surprisingly then, they result in similar values for R. The slight difference in the two expressions is due to approximations made in integrating over the bremsstrahlung cross section in the calculation of the thin target X-ray spectrum. As can be seen, a large range of magnetic field strengths is required, ranging from less than 50 G to more than 400 G. Thus the field strengths must vary by an order of magnitude in order to match the observations. A problem with this large range of magnetic fields is that the observed values of R vary over only two orders of magnitude. There is a lack of flares with extremely high (> 10), or extremely low ($< 10^{-3}$) values of R which would be expected for flares with high field and flat spectra or for flares with low field and steep spectra. Another serious problem is the high density which must be assumed in order to match the observations. The thin target assumption breaks down for $n_0 = 10^{11}\,\mathrm{cm}^{-3}$ for source size of order 10^9 cm. A more realistic density would be of order $10^9\,\mathrm{cm}^{-3}$, but this would lead to very large values of R which would be inconsistent with the observations, as earlier authors had found.

In figure 5.4 we plot R for the multithermal constant pressure model with $n_0 = nT_*/E_0 = 3.44 \times 10^{10}\,\mathrm{cm}^{-3}$. This corresponds to a gas pressure of 1.38×10^3 dynes cm^{-2}. Again, as in the thin target case, a large range of magnetic fields is required to match the observations. The constant pressure multithermal model however leads to even higher values of R than the thin target model for reasonable parameters. Note that a magnetic field of order 200 G is needed in order to magnetically confine such a plasma. Clearly there is a problem since the predicted field strength for some flares is less than 50 G.

5.6 - Summary

We therefore conclude that the observed microwave to X-ray ratios of solar flares are consistent with a single population of electrons producing both emissions. The thick target model with a reasonable set of flare parameters ($350\,\mathrm{G} \lesssim \mathrm{B} \lesssim 650\,\mathrm{G}$ and $L \approx 2 \times 10^9$ cm) explains the data quite well. The thin target and thermal models, however, have more difficulty in explaining the observations. A more rigid criteria for inclusion of flares in the sample such as limiting it to short, impulsive flares may lead to a smaller dispersion in parameters.

We will now examine the assumptions used arriving at these results. First of all we have assumed that the power law spectrum observed in X-rays extends to higher energies. There is some evidence from observations of gamma-rays (photon energies from 300 keV to 1 MeV) that the bremsstrahlung spectrum flattens at higher energies (Vestrand et al 1987) perhaps indicating a flattening of the electron energy spectrum. An even more complicated spectrum which again flattens at higher energies has been reported by Schmahl, Kundu, and Dennis (1985). Thus, the assumption of a single power law electron spectrum may be suspect. If the spectrum does flatten such that there are more electrons at higher energies than expected from the X-ray observations, the value of magnetic field required to match the observations decreases. This is acceptable for the thick target model but presents a further problem for the thin target and thermal models. However as pointed out above, for the thick target model the value of the critical energy E_1 rarely exceeds 500 KeV. Thus, the above mentioned changes in the electron spectral index will not have a large effect so that the thick target result remains accurate to the degree discussed earlier.

Another assumption we have made is that the synchrotron emission is optically thin. Since we do not have microwave spectral information we cannot be certain that the observed emission is optically thin for each of the flares, but the large majority of them probably are optically thin at 17 GHz since typical microwave bursts have turnover frequencies of order 10 GHz.

However from theoretical considerations, the optically thin assumption sets a lower limit to the area A of the microwave emitting region. Using the well known relativistic approximation for the optically thick part of the synchrotron spectrum it can be shown that

$$A > \frac{S_{\text{observed}}(\nu)c^2}{2\nu^2 E_1(\nu, B, \gamma)}. \tag{5.20}$$

For example, an observed burst of $S(17\,\text{GHz})/4\pi\text{D}^2 = 500$ SFU, with an X-ray spectral index of 4 and an assumed magnetic field of 550 G, leads to the condition that the area be greater than 3.5×10^{17} cm^2, which is a smaller area than estimates of the cross sections of flaring loops. Consequently, we feel the emission at 17 GHz will be optically thin for the majority of flares in table 1.

Finally we have assumed that no substantial trapping occurs in the loop in the thick target model. The effect of trapping would be to increase the number of particles in the loop and thus increase the microwave flux. The electrons in the loop emit microwaves and X-rays as in the thin target model since both emissions come from the same physical region. Thus a substantial amount of trapping the will give a value of R higher than that calculated for the thick target model with no trapping. This would mean that the value of magnetic field needed to match the observations will be smaller.

Chapter 5 Figure Captions

Figure 5.1 - The ratio of the analytic emissivity equation (5.17) at ν=17GHz and at a viewing angle of $\theta = 60°$ to the numerically calculated emissivity equation (P.8) for B=350, 500, and 650 G (dash-dot lines). Also for comparison purposes the ratio of the empirical expression of Dulk and Marsh (1982) to (P.8) is also plotted (dashed lines). For clarity, the curves for B=500 G and 350 G have been shifted upwards by factors of 10 and 100 respectively.

Figure 5.2 - The microwave to X-ray ratio R versus X-ray spectral index γ for the observed flares from Table 5.1 (squares) and theoretical curves (solid lines) for the thick target model, equation (5.18). The loop length $L = 2 \times 10^9$ cm, $\bar{\mu} = 0.5$, and the viewing angle $\theta = 70°$. The four curves are for B=650, 550, 450, and 350 G, from top to bottom. For comparison we also plot R (dashed lines) for the same parameters where we have numerically integrated (P.8) for the distribution in equation (5.7).

Figure 5.3 - Same as figure 5.2 for the isotropic thin target model, equation (5.18). The density $n_0 = 10^{11}$ cm^{-3} and $\theta = 70°$. The curves are for B=450, 350, 250, 150, and 50 G, from top to bottom.

Figure 5.4 - Same as figure 5.2 for the multithermal constant pressure model, equation (5.18). The parameter $n_0 = 3.44 \times 10^{10}\,\mathrm{cm}^{-3}$, corresponding to the product of density and temperature $nT = 10^{19}\,\mathrm{cm}^{-3}\,°\mathrm{K}$ or a constant pressure of 1.38×10^3 dynes cm^{-2}. The viewing angle $\theta = 70°$. The curves are for 400, 250, 150, and 50 G, from top to bottom.

Table 5.1: **Flare X-ray and Microwave Data**

Flare	$F_x(25\,\mathrm{keV})$	F_μ (SFU)	γ	R
40	1.2×10^{-5}	145	4.4	2.09×10^{-2}
58	1.3×10^{-6}	53	3.3	6.94×10^{-2}
77	8.3×10^{-6}	203	3.4	4.15×10^{-2}
85	1.0×10^{-6}	49	4.5	8.33×10^{-2}
127	5.4×10^{-6}	330	3.9	1.04×10^{-1}
150	6.1×10^{-6}	208	4.4	5.80×10^{-2}
160	5.5×10^{-7}	42	3.8	1.30×10^{-1}
165	5.1×10^{-6}	73	8.0	2.43×10^{-2}
187	1.3×10^{-5}	45	6.9	5.88×10^{-3}
261	1.6×10^{-6}	19	6.0	2.02×10^{-2}
386	5.0×10^{-7}	36	4.0	1.22×10^{-1}
428	6.9×10^{-6}	36	5.7	8.87×10^{-3}
458	8.4×10^{-6}	168	2.7	3.40×10^{-2}
466	1.1×10^{-5}	124	4.8	1.92×10^{-2}
479	3.1×10^{-5}	275	4.3	1.51×10^{-2}
634	9.2×10^{-5}	940	4.2	1.73×10^{-2}
651	5.6×10^{-7}	28	5.3	8.50×10^{-2}
679	7.7×10^{-6}	51	3.2	1.13×10^{-2}
683	2.6×10^{-5}	549	3.4	3.59×10^{-2}
688	1.2×10^{-4}	953	2.8	1.35×10^{-2}
716	5.0×10^{-6}	33	5.4	1.12×10^{-2}
761	6.3×10^{-7}	31	4.3	8.36×10^{-2}
766	9.8×10^{-7}	46	3.3	7.97×10^{-2}
841	4.2×10^{-6}	66	5.0	2.67×10^{-2}
842	5.2×10^{-7}	57	4.1	1.87×10^{-1}
851	1.6×10^{-5}	174	4.9	1.85×10^{-2}
879	6.7×10^{-6}	47	4.5	1.19×10^{-2}
1210	4.2×10^{-5}	526	4.6	2.13×10^{-2}
1215	5.4×10^{-6}	36	6.2	1.13×10^{-2}
1220	9.3×10^{-6}	130	3.8	2.38×10^{-2}
1266	8.4×10^{-7}	39	3.7	7.89×10^{-2}
1372	9.0×10^{-7}	31	4.1	5.85×10^{-2}
1424	5.8×10^{-7}	35	5.5	1.03×10^{-1}
1466	1.3×10^{-5}	249	4.4	3.26×10^{-2}
1504	2.1×10^{-6}	77	4.8	6.24×10^{-2}
1533	7.0×10^{-6}	214	3.7	5.20×10^{-2}
1534	3.2×10^{-5}	3420	3.9	1.82×10^{-1}
1541	2.9×10^{-6}	36	9.4	2.11×10^{-2}
1559	4.2×10^{-6}	50	10.2	2.02×10^{-2}
1563	2.9×10^{-4}	2490	4.8	1.46×10^{-2}
1565	4.8×10^{-7}	18	8.0	6.38×10^{-2}
1624	4.0×10^{-6}	61	5.4	2.60×10^{-2}
1636	1.0×10^{-6}	37	8.1	6.29×10^{-2}
1656	1.9×10^{-6}	55	6.3	4.91×10^{-2}
1696	3.5×10^{-6}	168	6.0	8.16×10^{-2}
1895	1.2×10^{-6}	25	3.7	3.54×10^{-2}
2061	2.2×10^{-6}	33	2.9	2.55×10^{-2}
2104	2.6×10^{-6}	779	3.9	5.10×10^{-1}
2293	3.2×10^{-5}	2065	3.5	1.10×10^{-1}
2628	1.0×10^{-5}	294	4.7	5.00×10^{-2}
2662	9.9×10^{-6}	> 660	3.7	1.13×10^{-1}
3485	1.9×10^{-5}	1920	3.3	1.72×10^{-1}
3503	6.5×10^{-7}	53	4.1	1.39×10^{-1}

Figure 5.1

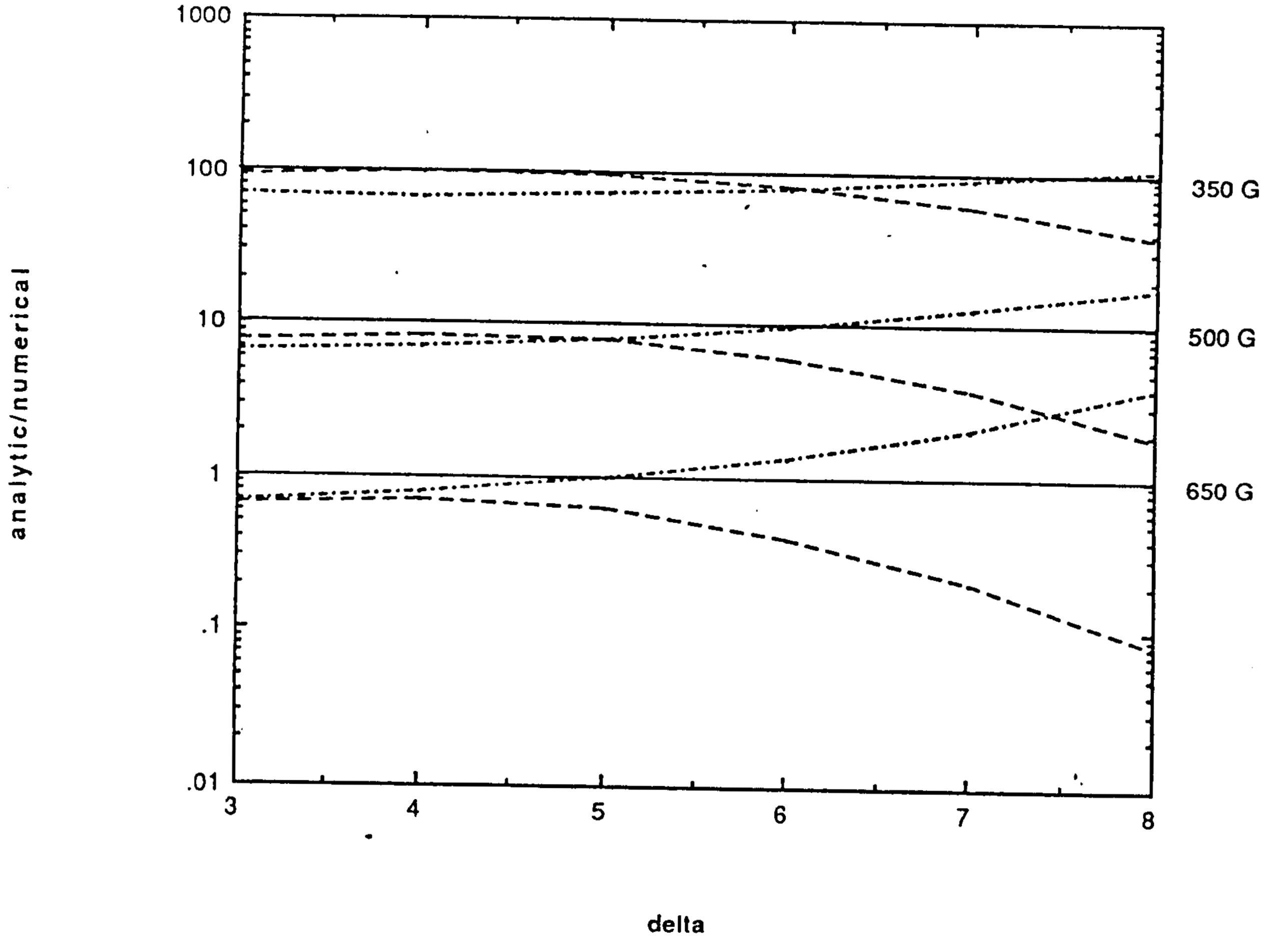
1000
100
10
1
.1
.01
3
4
5
6
7
8
analytic/numerical
delta
350 G
500 G
650 G

Figure 5.2

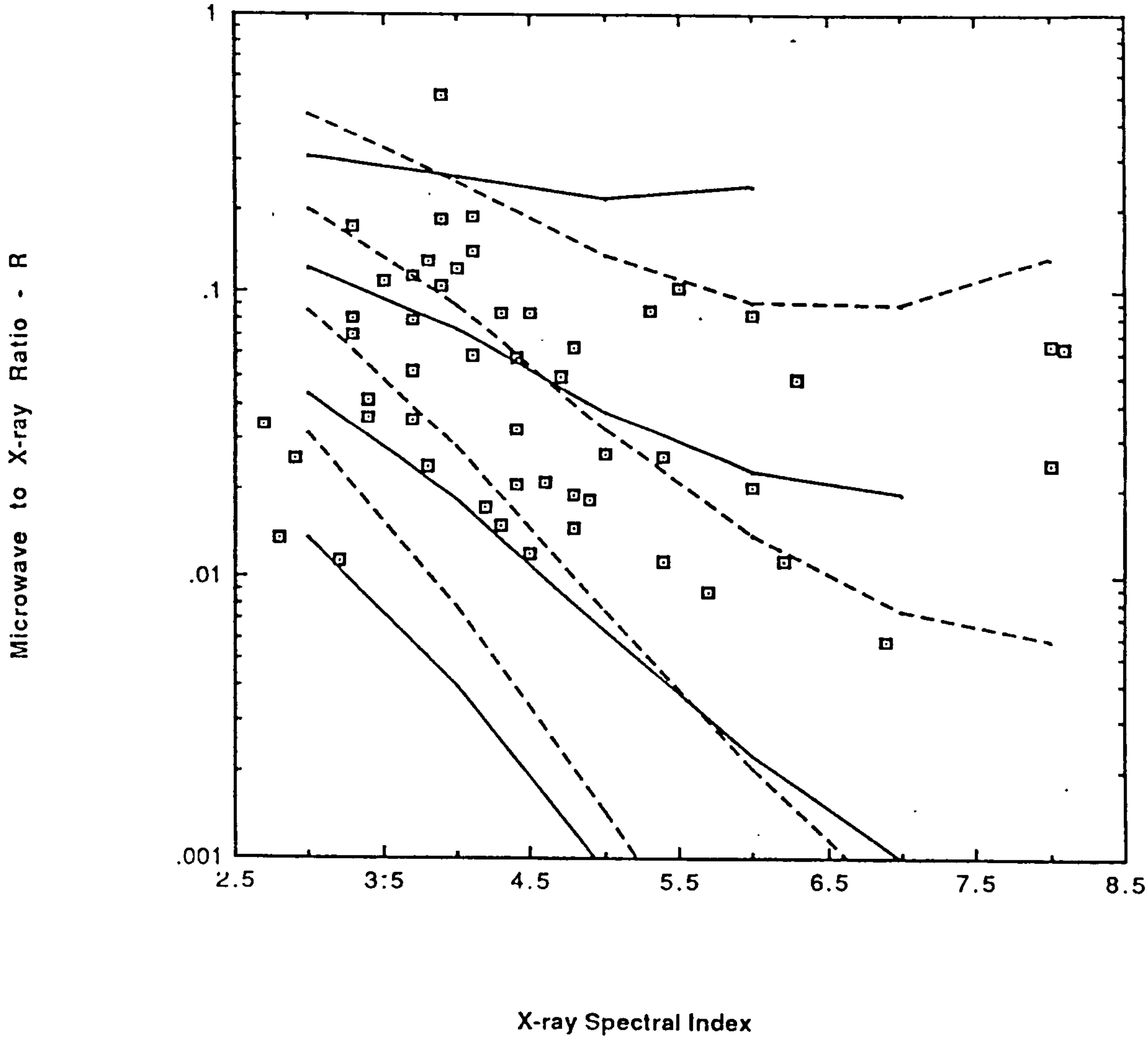
1
.1
.01
.001
2.5
3:5
4.5
5.5
6.5
7.5
8.5
Microwave to X-ray Ratio - R
X-ray Spectral Index

Figure 5.3

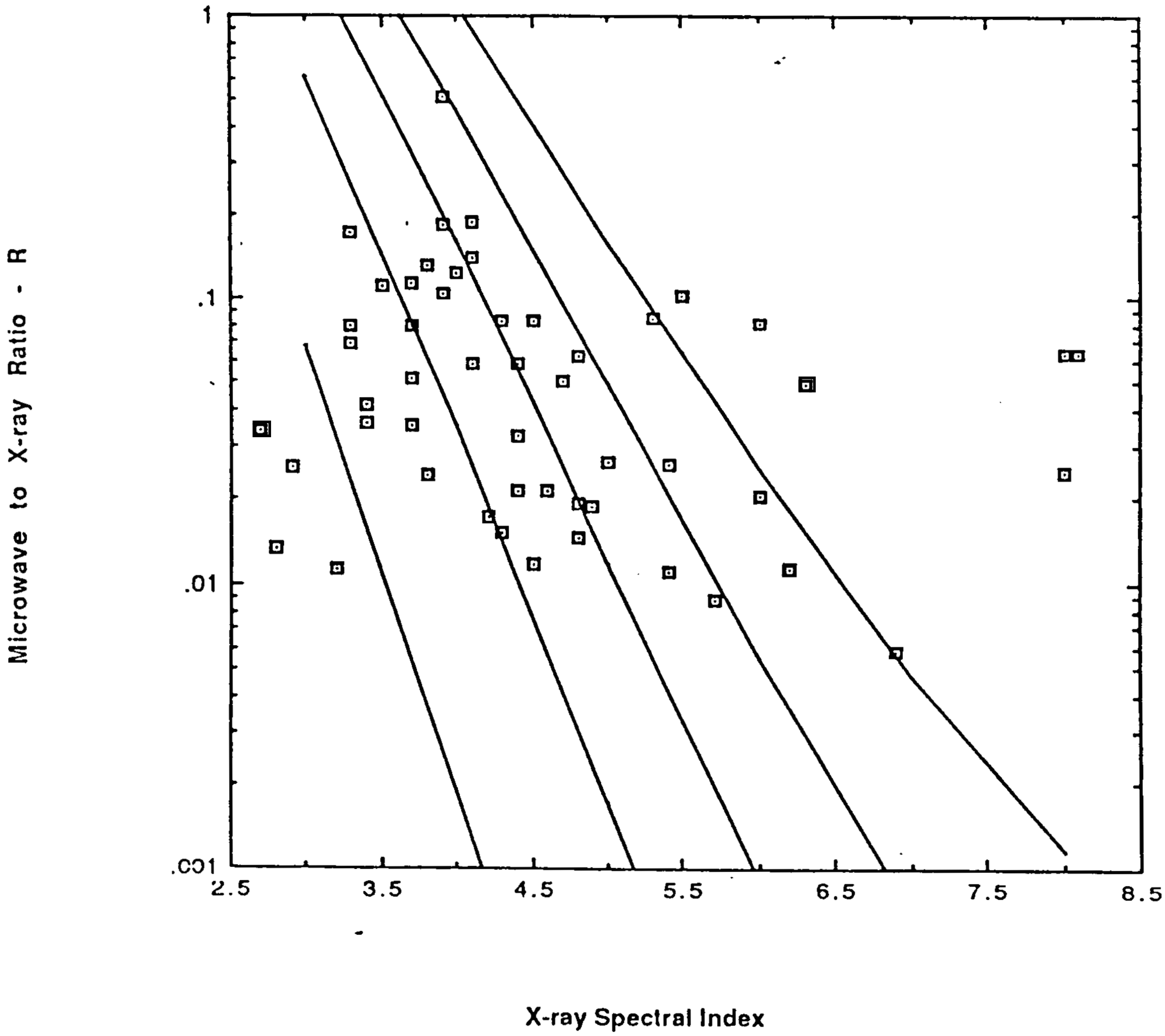

1
.1
.01
.001
2.5
3.5
4.5
5.5
6.5
7.5
8.5
Microwave to X-ray Ratio - R
X-ray Spectral Index

Figure 5.4

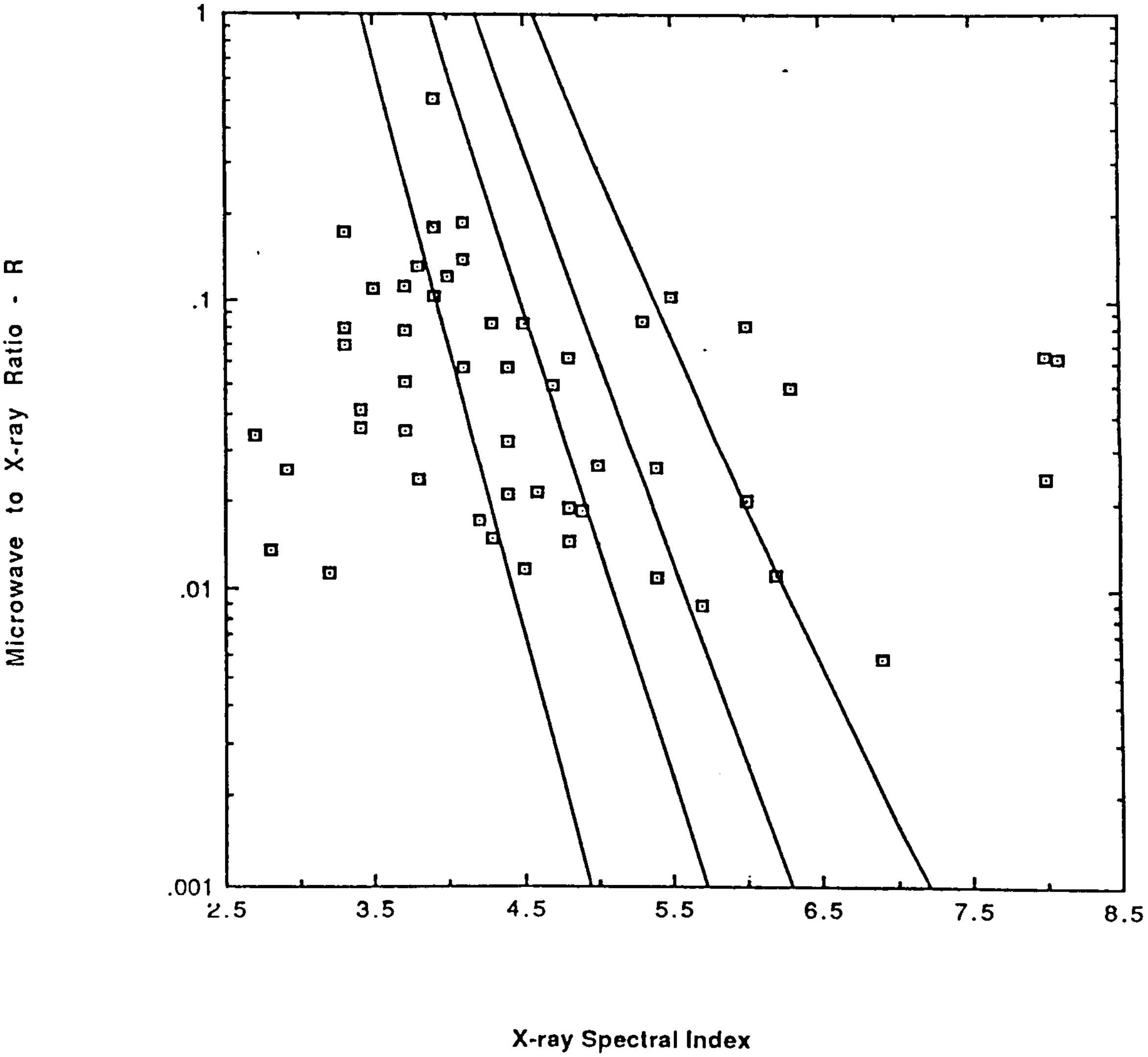
1
.1
.01
.001
2.5
3.5
4.5
5.5
6.5
7.5
8.5
Microwave to X-ray Ratio - R
X-ray Spectral Index

CHAPTER 6 - MICROWAVE AND X-RAY TIMING

6.1 - Introduction

We have now developed all the necessary tools to analyze the time evolution of microwaves and X-rays from flares. In this chapter we make use of the numerical Fokker-Planck code developed in chapter 4, and the analytic relations for the microwave to X-ray ratio developed in chapter 5 to investigate the relative timing of microwaves and X-rays. Although the microwaves and hard X-rays exhibit a very similar time structure, indicating a common origin for both, the microwave time profile seems to lag behind the X-ray time profile for most impulsive flares. This is opposite to what would be naively expected for simple nonthermal thick target models. In these models, high energy electrons are accelerated in the corona and stream downwards along a closed magnetic loop and are collisionally stopped when they reach the transition region. The microwaves are produced by synchrotron radiation while hard X-rays are produced by bremsstrahlung radiation primarily at the base of the loop where the plasma density is highest. For magnetic field strength $\sim 300-700$ G, the bulk of the microwave emission at 17 GHz is produced by electrons with energy $E \gtrsim 200$ keV, while most of the hard X-rays are produced by lower energy electrons ($E \lesssim 100$ keV). Thus, assuming all the electrons are energized at the same time, the microwaves would start to be produced as soon as the electrons are accelerated, while the X-rays would be produced about 0.1 seconds later when the electrons reach the base of the loop (length $l \sim 10^9$ cm). In addition, higher energy electrons are expected to lose energy more quickly since they propagate to higher density regions faster, as was shown in chapter 3 (cf Petrosian 1973).

One commonly suggested mechanism to explain the observed delay of microwaves is magnetic trapping, which would trap electrons in a converging magnetic field in the low density corona (see e.g. Dennis 1988, Cornell et al 1984, Kauffman et al 1983). The higher energy electrons responsible for the microwaves have a longer lifetime in the constant density trap, thus making the microwave emission last longer than the X-ray emission, and delaying the microwave peak time. Of course, the microwave emission could by delayed simply by accelerating the higher energy electrons later, or with greater pitch angle than the lower energy electrons primarily responsible for the hard X-rays.

There are actually two different sets of observations and two different types of microwave delays which must be explained. In the first set of observations, cross correlations of the X-rays and microwaves from flares which show rapid time variation have a maximum at microwaves lagging X-rays by ~ 0.25 seconds (see Cornell et al 1984, Kaufmann et al 1983). In the second set of observations, the peak flux time for simple impulsive spikes is observed to occur about 1 to 3 seconds earlier in X-rays than in microwaves (see Starr et al 1988). While these two observations may be related, they occur on different timescales, thus requiring different approaches. Since the timescale of the first problem is of order the collisional time for the electrons, a time dependent formulation is needed. The timescales in the second problem are much larger so that a steady state approach can be used. In attacking the first problem, we make use of the numerical code described in chapter 4 which solves the time dependent Fokker-Planck equation. We calculate the evolution of distributions of electrons in various solar flare models, and from this determine the expected microwave and X-ray emission. These results are presented in section 6.2. The second problem is dealt with in section 6.3 using the results of chapter 5 for steady state emission. Finally we provide a summary in section 6.4.

6.2 - Short Timescale Correlations

Observations with time resolution comparable to the collisional time or the time taken for accelerated electrons to reach the higher density chromosphere have become available only recently. An example of this is the HXRBS observation of spectral softening of the hard X-ray spectrum during the course of short timescale impulsive spikes (Kiplinger et al 1983). We have analyzed this phenomenon in chapter 3. Here we treat the relative timing of microwaves and X-rays, which is related to the emission by electrons with now widely seperated energies.

Kauffman et al 1983 have found for one flare that the microwaves at 22 GHz lag the X-ray photon flux at energies above 28 keV by about 200 to 300 ms. The microwaves from this flare have a rise and fall time of order 1 second and have smaller amplitude variations superimposed on the main pulse with timescale $\lesssim 0.2$ s. The X-rays have the same general time profile but also show much faster variation on timescales down to the 50 ms time resolution of the detector. A similar lag of microwaves behind X-rays is found when both emission profiles are filtered to eliminate the slowly varying component of the flare. Cornell et al 1984 report similar findings for a flare observed at 17 GHz in microwaves.

The structure of the magnetic field plays a more significant role in the emission of microwaves than the X-rays. In particular the field convergence and possible trapping of the higher energy electrons responsible for the microwave emission are important in determining the evolution of the microwave emission. Such a configuration requires a numerical solution of the transport equation for the electrons. In this section we describe results from such numerical solutions. We make use of the numerical Fokker-Planck code described in chapter 4 to calculate the evolution of distributions of electrons injected into various solar loop models. The resulting microwave and hard X-ray time profiles are then determined. In particular, we investigate what effect magnetic trapping has on these time profiles, and whether or not it is a viable mechanism for delaying the microwave flux behind the X-ray flux. As was mentioned earlier, the microwave emission can be delayed simply by injecting the higher energy electrons later than the lower energy electrons. The question we would like to address is whether trapping alone can account for the observed microwave delay for a simple injection with all electrons accelerated at the same location, at the same time, and with the same pitch angle distribution.

For each model, we specify the magnetic field, plasma density, and injection spectrum and time profile, then numerically calculate the evolution of the electron distribution using the Fokker-Planck code. The electrons change pitch angle and lose energy due to Coulomb collisions and magnetic mirroring so that the electron distribution evolves according to equation 2.2. This means we ignore effects due to reverse currents and plasma waves such as Langmuir turbulence. Given the electron distribution, the X-ray flux is determined by integrating over the isotropic bremsstrahlung cross section. The assumption of isotropic emission is reasonable because the effect of forward beaming of the bremsstrahlung photons is not severe at low energies, and because photospheric backscatter tends to isotropize the emission (see chapter 3). The synchrotron flux is calculated following the method of Petrosian 1981. The integral over electron pitch angles of the product of the electron distribution and the synchrotron emissivity is evaluated analytically using the method of steepest descent. This is a good approximation since the emissivity is a very sharply peaked function of electron pitch angle for harmonic number $\nu/\nu_b > 10$ which is the regime we are concerned with. For electron distributions which do not vary rapidly in pitch angle, the synchrotron flux in a direction at angle θ with respect to the magnetic field, due to electrons of a given energy is dominated by electrons with pitch angle cosine

$$\mu_{\max} \approx \beta \cos\theta \tag{6.1}$$

$c\beta$ is the electron velocity. Since most of the emission comes from electrons with

$\beta \approx 1$, the emission will be dependant on the number of electrons with pitch angle close to the viewing angle θ. The integration over electron energies (Petrosian 1981, equation 11) is done numerically, which gives higher accuracy than the analytic expressions.

We assume a model where electrons are accelerated high in a coronal loop. The loop is semicircular and symmetric about the loop top ($s = 0$), with the field being perpendicular to the chromosphere at the bases ($s < -10^9$ cm or $s > 10^9$ cm). The viewing direction is specified by polar angles ψ and ϕ (see figure 6.2.1). Since the angle the viewing direction makes with the magnetic field varies with position on the loop, the spatial distribution of the emitted microwaves and the time profile of the spatially integrated microwave flux will be dependant on viewing direction. For $\phi = 90°$, the viewing angle with respect to the magnetic field is $\theta = 90°$ at all points on the loop for loops on the limb ($\psi = 90°$), while for loops at the center of the disk ($\psi = 0°$) the viewing direction is perpendicular to the magnetic field at the loop top but parallel to the field at the bases.

The coronal density is $10^{10}\,\mathrm{cm}^{-3}$ for $0 < s < 7.5 \times 10^8$ cm. Collisions in the corona are therefore relatively unimportant when there is no trapping. The density then rises exponentially with scale height h. The total column depth from the top of the loop to the end of the grid is $1.5 \times 10^{22}\ \mathrm{cm}^{-2}$, which is sufficient to stop the electrons of energy below 350 keV which are responsible for nearly all of the hard X-rays. Since we end the spatial grid at a particular value of column depth, the maximum density on the grid increases with decreasing density scale height h. Higher energy electrons responsible for the microwaves can penetrate to larger depth. But since they emit most of the microwave radiation in the corona, we allow those electrons which reach the end of the spatial grid to simply run off the end, effectively being stopped instantaneously. We end the spatial grid at this point because the time step size is set by the maximum value of density on the grid, so that to continue the grid further would make the computing time prohibitively long without significant gain in accuracy. The spatial grid has 76 grid points spaced approximately equally in position s. The energy grid has 11 grid points spaced logarithmically from 25 keV up to 2 MeV, and the pitch angle grid has 29 grid points equally spaced in pitch angle cosine μ.

A. *Constant Magnetic Field*

We first investigate models with constant magnetic field strength. Since there is no magnetic convergence and the effect of collisions within the corona is small, an electron accelerated with some initial pitch angle will maintain that pitch angle as it traverses the loop. We inject electrons at rate S at the top of the loop with a power law energy distribution and a Gaussian distribution in pitch angle α of width α_0 (see equation 2 of Paper I).

$$S(E,\mu,s,t) = h(s)Q(t)E^{-\delta}\exp(-\alpha^2/\alpha_0^2) \tag{6.2}$$

The results we present are not sensitive to the spectral index δ or to the shape of $h(s)$ as long as its width is much less than the loop length. Consequently, in what follows we use $\delta = 4.5$ and $h(s) = \delta(s)$.

There are two factors which determine when the microwave emission will be peaked. First, synchrotron emission is generally greater in directions closer to perpendicular to the field. Also, as mentioned before, the emission in a given viewing direction is dominated by electrons of pitch angle cosine $\mu = \mu_{\mathbf{max}}$. Qualitatively then the microwave emission will be at a maximum when the combination of these two factors is greatest, i.e. when the electrons reach the position on the loop such that the viewing angle $\theta \approx 90°$ and the number of electrons at $\mu = \mu_{\mathbf{max}}(s)$ is maximized. For highly anisotropic electron distributions the second factor is dominant while for fairly isotropic distributions the first factor is more important.

In Figure 6.2.2 we show the X-ray and microwave emission at viewing direction $\psi = 60°$ and $\phi = 90°$, from a model with a constant magnetic field of 500 G, $Q(t) = \delta(t)$, and $\alpha_0 = 90°$. In Figure 6.2.3 we show the emission at $\psi = 60°$ and $\phi = 0°$. In this model we assume a density scale height $h = 1.5 \times 10^8$ cm, so that the maximum spatial grid point is at $s = 2.1 \times 10^9$ cm, where the density is 10^{14} cm^{-3}. We choose this fairly long value of density scale height to shorten the computing time necessary. The X-ray emission in any case is fairly insensitive to the scale height h because the X-ray emitting electrons are stopped quickly in the rising density plasma.

As can be seen, the X-ray emission peaks at $t \approx .1$ s which is approximately the propagation time for the electrons to reach the high density footpoints. The microwave emission however is greatest at $t = 0$ for $\phi = 90°$, while at $\phi = 0°$ the emission peaks just after $t = 0$. The microwave emission then decreases due to the increase in angle between the viewing direction and the magnetic field as the electrons move towards the footpoint.

For a more realistic shorter value of the density scale height, the X-ray peak will shift to slightly earlier time but by an insignificant amount. The microwave emission will also be unaffected because most of the microwaves are emitted in thke corona. Thus as expected, the simple thick target model with no magnetic field convergence and delta function in time injection has a microwave time profile which leads the X-ray time profile. The microwave to X-ray ratio R for continuous injection of an electron spectrum of equation (6.2) can be calculated by integrating over time the microwaves and X-rays from the delta function in time injection. Note that this will give a lower limit to R because the microwave flux had not completely decayed away at $t = 0.6$ s when the simulation was ended. The spectral index of the integrated X-rays is 3.9 and the steady state ratio $R > 0.13$ at $\phi = 90°$ and $R > 0.052$ at $\phi = 0°$.

For an arbitrary injection time profile $Q(t)$, the microwave and X-ray time profiles will simply be the curves in figures 6.2.2 or 6.2.3 convolved with $Q(t)$. This has the effect of delaying the microwaves because the microwave decay time is longer than the X-ray decay time. However, in order to have X-ray or microwave emission which varies on times of order 0.2 s, $Q(t)$ must also vary on timescales of this order. For $Q(t)$ which does vary on this timescale, the X-rays will still lead the microwaves.

B. *Converging Magnetic Field*

Next we investigate models with converging magnetic field. Another factor must now be considered in determining the time of maximum synchrotron emission, namely that synchrotron emission is a strongly increasing function of magnetic field strength. The X-ray emission however is not sensitive to the degree of convergence of the magnetic field. This is due to the fact that most of the X-rays at the peak are produced by electrons with small pitch angle which are relatively unaffected by the magnetic field convergence.

In Figure 6.2.4 we show the emission from a model where the magnetic field increases exponentially with scale height 2×10^9 cm up to a mirror ratio of 1.5. The field strength is 360 G at the top of the loop and increases to 540 G at the footpoints, then remains constant below that. The injected electron distribution is identical to that for the model with no convergence, i.e. $Q(t) = \delta(t)$ and $\alpha_0 = 90°$. The magnetic field convergence traps electrons with initial pitch angle greater than 55°, or 59% of the injected electrons. Here the peak in microwaves occurs 0.1 s after the X-rays. This delay is due to the fact that almost all the X-rays at the peak are produced by the electrons with small pitch angle which escape directly to the footpoint, while the microwaves are primarily due to the higher pitch angle electrons which propagate along the field slower. The peak in the microwaves occurs when the high pitch angle electrons mirror and begin moving back upwards. The synchrotron emission is greater at this point both because the magnetic field is strongest at the bases and because the emission in the upwards direction is dominated by electrons moving in the upwards direction. Although the lower energy electrons have smaller velocity, the higher pitch angle of the microwave producing electrons allows them to propagate down the loop slower. Making the magnetic field increase further does not push the microwave peak further back because this only serves to mirror back the lower pitch angle electrons which propagate down the loop faster, and which do not contribute much to the microwave emission anyway.

We end the simulation at $t = 1.2$ s because the computing time becomes prohibitive. However, at this point, the microwave emission due to trapped electrons in the loop has not yet decayed away because the microwave producing electrons have lifetimes of many seconds in the low density coronal plasma. The steady state value of R is increased greatly by trapping of electrons. For the model run shown in figure 6.2.4, we have $R > .15$ at $\phi = 90°$. For an injection which varies on the timescale of seconds, the value of R will be given by this steady state value. Thus, for a given observed value of R, the inferred magnetic field will be lower for a model with trapping.

In figure (6.2.5) we show the emission for the same model but with an extended injection $Q(t) = \exp(-((t - .3)/.2)^2)$. In this case we see that the microwaves lag the X-rays by 0.15 s, which is still smaller than the observed delay. Thus, for magnetic convergence which occurs in the corona, the delay of microwaves is not large enough to match observations.

We have found however that it is possible to produce a larger microwave delay although we must assume an unrealistic model to do so. In this model the magnetic convergence occurs both in the corona and below the transition region. The density scale height h must be large enough so that the microwave producing electrons ($E \sim 500$ keV) can penetrate to substantially greater depths before mirroring back than the X-ray producing electrons with $E \sim 100$ keV. In figure 6.2.6 we show the microwave and X-ray emission from a model with $h = 1.5 \times 10^8$ cm, and magnetic field which increases exponentially with scale height 5×10^8 cm from 400 G at the top of the loop. However at other viewing directions the microwave time profile looks considerably different. In fact at $\psi = 60°$, $\phi = 60°$, the microwave flux is as large at $t = 0$ as it is at $t = 0.3$ s (see figure 6.2.7). For more realistic shorter density scale height h, the microwave delay is reduced because less of the microwave producing electrons are able to penetrate deep enough to mirror back without being collisionally stopped.

In figure 6.2.8 we show the microwave emission from a model where the convergence occurs below the transition region, as opposed to in the corona. We assume a magnetic field which is proportional to the 0.2 power of the density, and a more realistic value for the density scale height $h = 5 \times 10^7$ cm. The magnetic field is constant at 400 G from $0 < s < 7.5 \times 10^8$ cm. The field then rises as the 0.2 power of the density (in other words with scale height 2.5×10^8 cm) until it reaches 600 G. The field is constant below that. To reduce the computing time the minimum energy grid point was set at 100 keV, which does not allow us to calculate the X-ray emission. The X-ray peak will occur at $t \approx 0.1$ s as before since the stopping time once the electrons reach the footpoint is short compared to the time of flight through the corona. In this case the microwaves again do not lag the X-rays by long enough to match observations. In fact the microwave delay is even less than for the case where the convergence all occurred in the corona (see figure 6.2.4). This is because the the time it takes for electrons of initial pitch angle cosine μ_0 to mirror back is essentially $L/c\beta\mu_0$ where L is the half length of the loop. If the convergence takes place throughout the loop the then the electrons spend more time at higher pitch angle so the time it takes to mirror back is longer than the $L/c\beta\mu_0$ (see e.g. equation 4.14).

Thus, the peak time of the microwaves does indeed lag behind that of the X-rays in a converging magnetic field. This delay is caused by the fact that the time it takes for the high pitch angle, high energy electrons to mirror back upwards can exceed the time it takes for the low energy, low pitch angle electrons to propagate to the footpoint. In order to match the observed .25 s delay, we must assume a fairly slowly rising density in the transition region, a slowly rising magnetic field so that electrons with high pitch angles can mirror at depths $\sim 5 \times 10^8$ cm below where the X-rays are produced, and a long loop length. However, this 0.25 s delay will not be observed in all directions, and will also be strongly dependent on the geometry of the loop (we have assumed a semicircular loop).

We can however simply inject the higher energy electrons slightly later than lower energy electrons to delay the microwave peak. In figure 6.2.9 we show the emission with $Q(t) = \exp(-((t+.1-.3\beta)/.07)^2)$ and $\alpha_0 = 45°$, in other words with higher energy electrons accelerated later. The peak injection time for electrons of energy 50 keV is at $t = .033$ s while the peak injection time for electrons of energy 500 keV is at $t = .16$ s. The magnetic field converges by a factor of 1.3 in the corona. The X-rays now lead the microwaves by ~ 0.3 s. Note that the difference in injection times of the microwave and X-ray producing electrons is comparable to the width of the injected pulse itself.

Since we only have observations of two individual flares we cannot be sure that this observed delay of microwaves behind X-rays by ~ 0.25 s occurs in all, or even most flares with short timescale variations. If it does, it is hard to see how magnetic trapping can account for all of the observed delay because it is difficult to produce delays of this magnitude and because of the fact that the delay is very dependent on viewing direction. More likely then is the explanation that at least some of the delay is due to later acceleration of higher energy electrons since this would not be as dependent on viewing direction or loop geometry.

6.3 - Longer Timescale Correlations

Our discussions in the previous section were limited to the relative timing between the microwave and hard X-ray emission for timescales comparable to the transport timescale of the accelerated electrons. We did not consider the relative strengths of the two emissions. While the first aspect of the problem is sensitive to the geometry of the magnetic field and the pitch angle distribution of the electrons, the second aspect depends on the strength of the magnetic field and on the injected spectrum of electrons. We now consider the second aspect of the problem and investigate the microwave and X-ray emission over times ~ 1 s which is much larger than the transport timescale. Consequently, we need not solve the time dependent kinetic equation and can instead rely on steady state solutions. In particular, we will use the procedure developed in chapter 5 which dealt with the ratio of microwave to X-ray fluxes of impulsive flares. We apply this procedure now to the evolution of individual flares.

Electrons injected into a loop of length $\sim 10^9$ cm with no trapping have a lifetime of a few tenths of a second, which is shorter than the 1 second integration time of the observations which we will make use of. We can therefore use the analytic relations derived in Lu and Petrosian 1988 for the steady state ratio of microwaves to X-rays from the thick target beam and thin target models when dealing with microwave delays of order seconds. In chapter 5, we defined the dimensionless ratio of microwaves to X-rays R and it was shown that the observed values of R evaluated at the flare peaks were most consistent with the nonthermal thick target beam model. The ratio R for the multithermal model and the thin target models is substantially higher, and is a much stronger function of the X-ray spectral index than it is for the thick target model. The reason the thick

C-2

target model has much lower microwave emission is that the microwaves come primarily from the loop, before the electron distribution has been substantially affected by collisions. Most of the X-rays are emitted at the base of the loop where the electron spectrum has been hardened by collisions. The thin target and multithermal models, on the other hand, have both microwaves and X-rays coming from the same physical region so that the same distribution of electrons is used in calculating both emissions.

In this section we investigate the relative timing of microwaves and X-rays from solar flares with well known X-ray spectral indices throughout the course of the the flare. These flares were observed in X-rays by the HXRBS instrument aboard the SMM spacecraft and simultaneously in microwaves by the 17 GHz polarimeter at Nobeyama. Most of these flares have a simple time structure with rise and fall times $\sim$ 10 s. The data are integrated over 1 second bins, which is longer than the propagation time down the loop for an electron which is not trapped. In figure 6.3.1 we plot the 17 GHz flux and total X-ray flux for a typical flare. Note that the microwave peak is delayed by $\sim$ 2 seconds. In only one of the 6 flares for which we have data for does the X-ray peak occur after the microwave peak.

In figure 6.3.2 we plot for the same flare the observed microwave flux, and the expected microwave flux for the thick target model given the observed X-ray flux and spectral index (calculated using equation 5.18). Also plotted is the difference between the observed microwave flux and the calculated flux. As can be seen, the fit on the rising part of the flare is very good, while during the decay phase the observed microwave flux is considerably greater than the calculated value. Figure 6.3.3 is the same as Figure 6.3.2 except that the calculated flux assumes thin target emission in a plasma of density 10^{11} cm^{-3} with magnetic field strength 100 G. The predicted microwaves do not match the observed microwaves nearly as well as the thick target model owing to the much stronger dependance on spectral index γ.

Thus, although the microwaves and X-rays match the predictions of the single power law nonthermal thick target model very well during the burst rise, there is an excess of microwaves during the decay phase which must be explained. The fact that the microwave peak occurs after the X-ray peak can be interpreted as being due to the appearance of this additional microwave component. During the decay, the ratio $R_{\text{observed}}/R_{\text{thick target}}$ rises from ~ 1 to ~ 10. We explore a number of possibilites to explain the microwave excess below.

Flattening in Spectrum: In figure 6.3.2, we have assumed an injected electron spectrum which is a single power law in energy. The microwave production will however be greater if the injected electron spectrum is not a single power law, but flattens at energies above the energy of the hard X-ray emitting electrons and below that of the electrons responsible for the bulk of the microwaves. This flattening in the electron spectrum would also be visible as a flattening in the X-ray spectrum at higher energies. The power law fit to the observed hard X-ray spectra for the flare in Figure 6.3.1 was fit to the count rates for energy channels from 37 keV up to $\sim$ 300 keV (*HXRBS* energy channels 2 through 10 ± 1), depending upon the count rate. The count rates for energy channels above 300 keV, especially on the decay phase, was for the most part too low to get reliable statistics. Thus, if the X-ray spectrum does harden at higher energies, it does so above $\sim$ 300 keV.

To determine if a flattening in the injected electron spectrum can be responsible for the microwave excess, we assume the X-ray spectrum is the sum of two power laws. Besides the low energy X-ray spectrum observed by *HXRBS*, we add a high energy power law with energy flux $F_h(E_B)$ above break energy E_B, and with spectral index $\gamma_h < \gamma$. We assume the two power laws have equal contribution at energy E_B so that the low energy power law with spectral index γ dominates for $E << E_B$, while the high energy power law dominates for $E >> E_B$. This condition gives us for the energy flux $F_h(E_B)$ in the high energy power law

$$F_h(E_B) = \left(\frac{E_B}{E_0}\right)^{-\gamma+2} \left(\frac{\gamma-2}{\gamma_h-2}\right) F_x(E_0) \tag{6.3}$$

Furthermore we assume that $E_B > 300$ keV so that the HXRBS does not observe the high energy power law. The observed microwave to X-ray flux ratio for the two power law model R_2 is then

$$R_2 = R(E_0,\gamma) + \left(\frac{E_B}{E_0}\right)^{-\gamma+2} \left(\frac{\gamma-2}{\gamma_h-2}\right) R(E_B,\gamma_h). \tag{6.4}$$

For magnetic fields of order 500 G, and for $\gamma \lesssim 3$, the energy of the electrons responsible for most of the microwave radiation becomes relativistic so we must modify equation 5.18 since in that equation we assumed nonrelativistic electrons in calculating the length of time a particle spends in the loop.

During the burst decay when the excess microwave flux is at a maximum, the low energy spectral index $\gamma \approx 3$. The calculated value of $R(E_0 = 25\,\text{keV}, \gamma = 3)$ for the simple one power law thick target model with loop length 2×10^9 cm, magnetic field strength 500 G, at viewing angle 60° is $R = .06$, while the observed value of R increases to $\sim .5$ during the burst decay. Thus the high energy power law must account for most of the microwave flux. For $\gamma_h = 2$ and $E_B = 300$ keV, we find $R_2 = .6$. Thus it is possible for a change in the spectral index of order 1 at energy above 300 keV to account for the microwave excess. This flattening in the spectrum must occur only in the later stages of the flare since the emission during the rising phase matches a single power law very well. Stochastic acceleration by turbulence could account for this. As the flare proceeds, turbulence builds up in the corona so that the higher energy component only appears in the later part of the flare. Other evidence in support of spectral flattening at high energies has been given by Vestrand et al 1987 who reported that gamma-ray spectral indices of flares are on the average smaller by about 1 than the hard X-ray spectral indices.

Thermal Synchrotron: Next we consider the possibility that the microwave excess is due to synchrotron emission from a thermal plasma with $T \sim 5 \times 10^7\,^\circ\mathrm{K}$. Lin et al 1981 have reported the observation of a superhot $3.4 \times 10^7\,^\circ\mathrm{K}$ thermal component of the hard X-rays which appeared during the decay phase of a flare. The emission measure of this plasma was a few times $10^{48}\,\mathrm{cm}^{-3}$. This thermal plasma is distinct from and has much smaller emission measure than the much cooler $2 \times 10^7\,^\circ\mathrm{K}$ thermal plasma observed from flares in soft X-rays by the GOES satellite. Nitta et al 1989 also report an observation of a super hot thermal plasma with $T \sim 7 \times 10^7\,^\circ\mathrm{K}$ and emission measure $\sim 10^{47}\,\mathrm{cm}^{-3}$.

Making use of expressions for optically thin thermal synchrotron emission from Petrosian 1981, we find that it is possible to produce the observed microwave excess of $\sim$ 300 SFU with a thermal plasma of temperature $T = 5 \times 10^7\,^\circ\mathrm{K}$, magnetic field $B = 550$ G, and total number of particles $nV = 10^{39}$. The total thermal energy in this plasma is $(3/2)NkT = 9 \times 10^{30}$ ergs. If we assume a density of $10^9\,\mathrm{cm}^{-3}$ we obtain an emission measure of $10^{48}\,\mathrm{cm}^{-3}$ which is consistent with the observed emission measures of Lin et al and Nitta et al. This possibility is easily can be easily checked given microwave observations several different frequencies both higher and lower than 17 GHz. Thermal microwave emission falls off very rapidly with frequency, as approximately the 8th power of frequency. However, emission by a nonthermal power law distribution of electrons falls off much more slowly, as approximately the $(\delta - 1)/2$ power of frequency.

Nitta et al 1989 considered the possibility that thermal synchrotron could account for the observed microwave radiation. They however discount any kind of thermal emission as being responsible for all the microwave flux because the emission would have exceeded the Rayleigh-Jeans emissivity. This was based upon the observed area of the thermal plasma imaged in hard X-rays and on a temperature of $7 \times 10^7\,^\circ\mathrm{K}$ estimated from the hard X-ray spectrum.

Thermal Free-Free Emission: Thermal free-free emission is dominated by thermal synchrotron emission for densities

$$n < (3.9 \times 10^{13}) \left(\frac{T}{10^8\,{}^\circ\mathrm{K}}\right)^{8.5} \left(\frac{B}{500\,\mathrm{G}}\right)^{9} \left(\frac{\nu}{17\,\mathrm{GHz}}\right)^{-8} \sin^6\theta, \qquad (6.5)$$

where θ is the viewing angle with respect to the magnetic field. Here we have used the empirical thermal synchrotron emissivity relations of Dulk and Marsh (1982). Thus, for magnetic field strength 500 G, and temperatures high enough to make thermal synchrotron significant ($T \gtrsim 3 \times 10^7\,{}^\circ\mathrm{K}$), free-free emission will be insignificant compared to thermal synchrotron for density equal to $10^9\ \mathrm{cm}^{-3}$.

Trapping: Another possibility is that during the decay phase, some of the emission is nonthermal thin target. This could occur if some of the electrons are magnetically trapped in the corona. These trapped electrons must must be responsible for most of the microwave flux, but not contribute significantly to the X-ray emission. As Figure 6.3.3 shows, the microwave emission does not match the predictions of the thin target model very well. In addition, in order to reduce the thin target R down to the observed value, we had to assume a fairly high density of $10^{11}\ \mathrm{cm}^{-3}$ and a very low magnetic field of 100 G. This field strength is obviously inconsistent with the 500 G value inferred from the burst rise. Thus, it is unlikely that all of the microwave and X-ray emission is thin target, meaning that the microwave and X-rays are not cospatial. However, if the X-ray emission is still thick target so that the electrons are eventually stopped at the footpoints, but the electron lifetime in the loop is increased due to trapping, then R will also be increased because the effective loop length will be larger. Thus in order to match the observations during the decay of the burst, the effective loop length must increase to of order 2×10^{10} cm, or in other words the electrons must on the average traverse the loop ~ 10 times before escaping to the footpoints. It is possible then that the amount of trapping increases in the later part of the flare, therefore increasing the value of R.

6.4 - Summary and Discussion

We have investigated the observed delay of microwaves behind X-rays from solar flares. The observations show a lag of $\sim .25$ s for short timescale variations, while the peak times of flares of duration ~ 30 s show a microwave lag of ~ 2 s. To investigate the small timescale delay, we use the numerical code described in chapter 4 to numerically solve the time dependent Fokker-Planck equation for electrons injected into various solar flare models. We have found that as expected, the microwaves lead the X-rays in a constant magnetic field loop with all electrons injected at the same time with the same pitch angle distribution. However, in a converging magnetic field, the microwave time profile can be delayed behind the X-rays. In order to produce a delay large enough to match observations, the loop must be fairly long and the density must increase fairly slowly in the transition region. The magnetic field must also increase fairly slowly so that high pitch electrons can mirror back below the depth where the X-rays originate. This delay is however strongly dependent on viewing direction and on the spatial geometry of the loop. Only in some viewing directions is the delay as large as 0.25 s. We therefore consider it unlikely that all of the observed delay is due to magnetic convergence, but rather some of the delay is due to later acceleration of higher energy or higher pitch angle particles. One possible mechanism for this to occur is stochastic acceleration by plasma turbulence such as Langmuir waves. The electrons would then be initally accelerated by some other process such as magnetic reconnection. Higher energy electrons could then be further accelerated by Langmuir waves.

For longer timescale bursts, we find that the microwaves and X-rays during the rising phase of the flare match the predictions of the thick target model very well. However, during the decay the microwave emission is far larger than the calculated emission. We interpret the delay of the microwave peak as due to an excess of microwaves above the thick target emission. Possible explanations include a flattening in the electron spectrum at energies above the hard X-rays, a contribution from thermal synchrotron to the microwave flux, trapping of electrons in the loop, or some combination of these factors. Again, some form of stochastic acceleration could provide a mechanism whereby higher energy electrons are further accelerated.

Chapter 6 Figure Captions

Figure 6.2.1 - Geometry of the loop. Electrons are accelerated at the top of a semicircular loop. The magnetic field at the footpoints is perpendicular to the photosphere. The viewing direction is given by angles ψ and ϕ.

Figure 6.2.2 - Constant magnetic field. Injection of $Q(t) = \delta(t)$ and $\alpha_0 = 90°$ into a magnetic field of 500 G. Viewing direction is $\psi = 60°$, $\phi = 90°$. Density scale height $h = 1.5 \times 10^8$ cm. The microwave flux density at 17 GHZ is given by the dashed line and is in units of $\mathrm{ergs\,s^{-1}\,cm^{-2}}$. The X-ray photon number flux above 25 keV is given by the dashed line. The time is given in seconds.

Figure 6.2.3 - Constant magnetic field. The same as Figure 6.2.2 except $\psi = 60°$, $\phi = 0°$.

Figure 6.2.4 - Convergence in the corona. The magnetic field increases exponentially with scale height 2×10^9 cm from 360 G at the top of the loop to 540 G at $s = 8.1 \times 10^8$ cm. The field is constant below that. Injection of $Q(t) = \delta(t)$ and $\alpha_0 = 90°$. Density scale height $h = 1.5 \times 10^8$ cm. Viewing direction is $\psi = 60°$, $\phi = 90°$. Microwaves are given by the dashed line, X-rays by the solid line.

Figure 6.2.5 - Convergence in the corona. Same as Figure 6.2.4 except $Q(t) = \exp(-((t - .2)/.2)^2)$.

Figure 6.2.6 - Convergence both in the corona and below the transition region. The magnetic field increases from 400 G to 600 G with scale height 5×10^9 cm. Injection of $Q(t) = \delta(t)$ and $\alpha_0 = 60°$. Density scale height $h = 1.5 \times 10^8$ cm. Viewing direction is $\psi = 60°$, $\phi = 90°$. Microwaves are given by the dashed line, X-rays by the solid line.

Figure 6.2.7 - Convergence both in the corona and below the transition region. Same as Figure 6.2.6 except $\psi = 60°$, $\phi = 0°$.

Figure 6.2.8 - Microwave emission for convergence in the transition region. Rapidly rising density. The magnetic field is constant at 400 G up to $s = 7.5 \times 10^8$ cm. It increases with scale height 2.5×10^8 cm to 600 G, then is constant below that. Density scale height $h = 5 \times 10^7$ cm.

Figure 6.2.9 - Later acceleration of higher energy electrons. Injection of $Q(t) = \exp(-((t + .1 - .3\beta)/.07)^2)$ with $\alpha_0 = 45°$. Magnetic field increases exponentially from 400 G to 520 G with scale height 4×10^9 cm. Density scale height $h = 1.5 \times 10^8$ cm. Viewing direction is $\psi = 60°$, $\phi = 90°$. Microwaves are given by the dashed line, X-rays by the solid line.

Figure 6.3.1 - Microwave and X-ray emission from a flare occurring on November 25, 1982 (SMM flare number 6738). The microwave flux density at 17 GHz in SFU is given by the dashed line. ($1\,\mathrm{SFU} = 10^{-19}\,\mathrm{erg\,s^{-1}\,cm^{-2}\,Hz^{-1}}$). The X-ray energy flux above 25 keV is given by the solid line. The times are given in seconds from an arbitrary $t = 0$.

Figure 6.3.2 - Comparison of the expected thick target microwave emission and observed microwave emission. The calculated emission assumes a loop length of 2×10^9 cm, magnetic field of 500 G, and viewing angle $\theta = 60°$. The calculated emission is given by the solid line, the observed emission is given by the dashed line, and the difference is given by the dash-dot line.

Figure 6.3.3 - Comparison of the expected thin target microwave emission and observed microwave emission. The calculated emission assumes magnetic field of 100 G, density 10^{11} cm^{-3}, and viewing angle $\theta = 60°$.

Figure 6.2.1

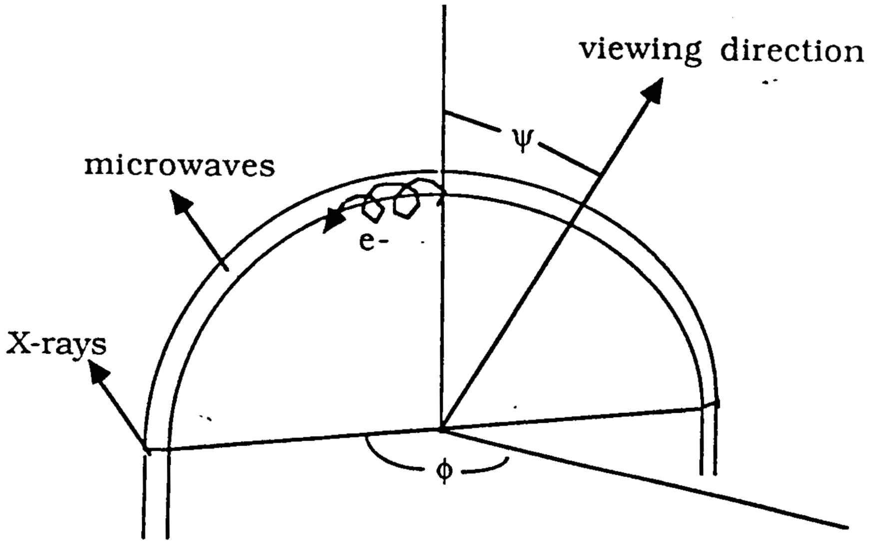

Figure 6.2.2

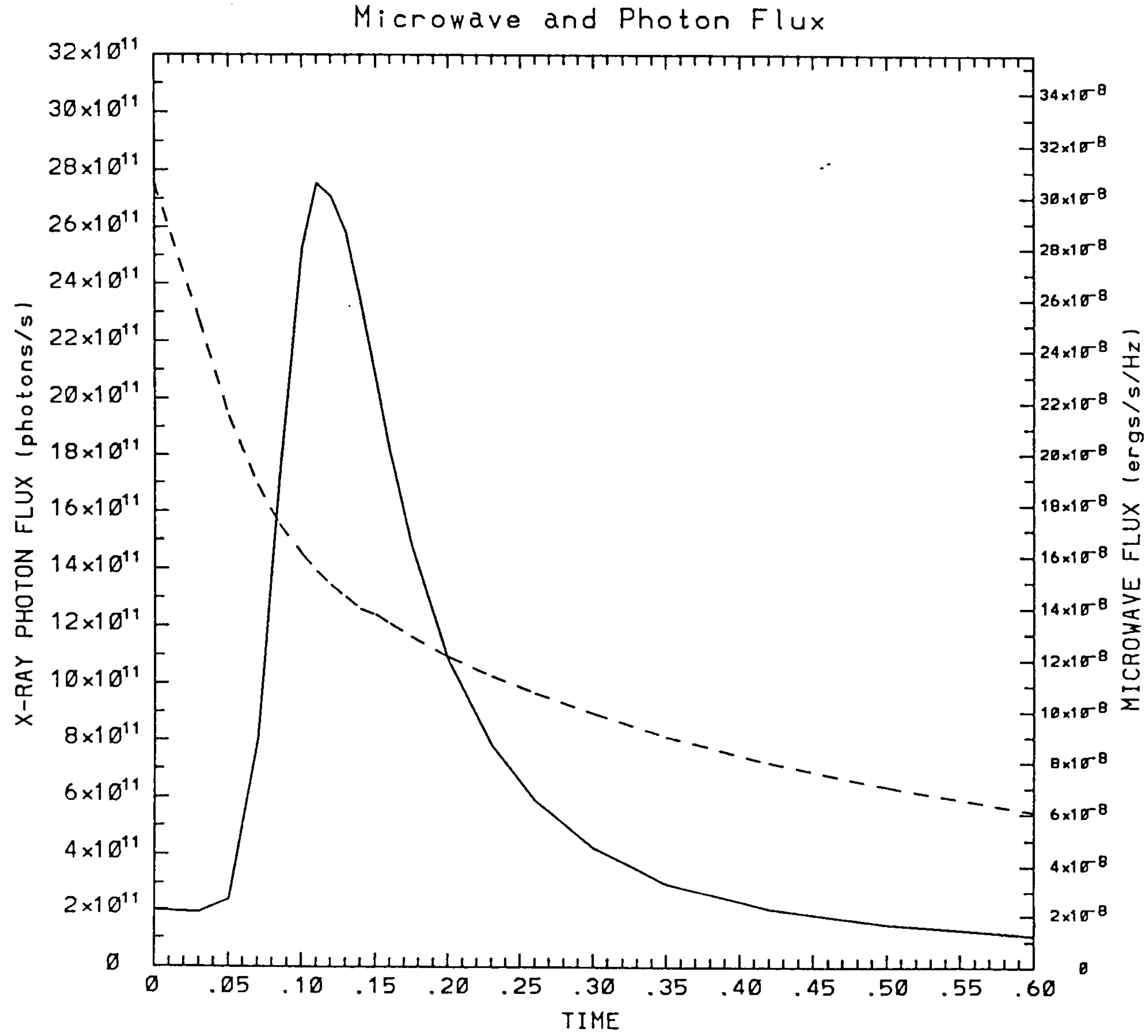
Microwave and Photon Flux
X-RAY PHOTON FLUX (photons/s)
32x10^11
30x10^11
28x10^11
26x10^11
24x10^11
22x10^11
20x10^11
18x10^11
16x10^11
14x10^11
12x10^11
10x10^11
8x10^11
6x10^11
4x10^11
2x10^11
0
MICROWAVE FLUX (ergs/s/Hz)
34x10^-8
32x10^-8
30x10^-8
28x10^-8
26x10^-8
24x10^-8
22x10^-8
20x10^-8
18x10^-8
16x10^-8
14x10^-8
12x10^-8
10x10^-8
8x10^-8
6x10^-8
4x10^-8
2x10^-8
0
0
.05
.10
.15
.20
.25
.30
.35
.40
.45
.50
.55
.60
TIME

Figure 6.2.3

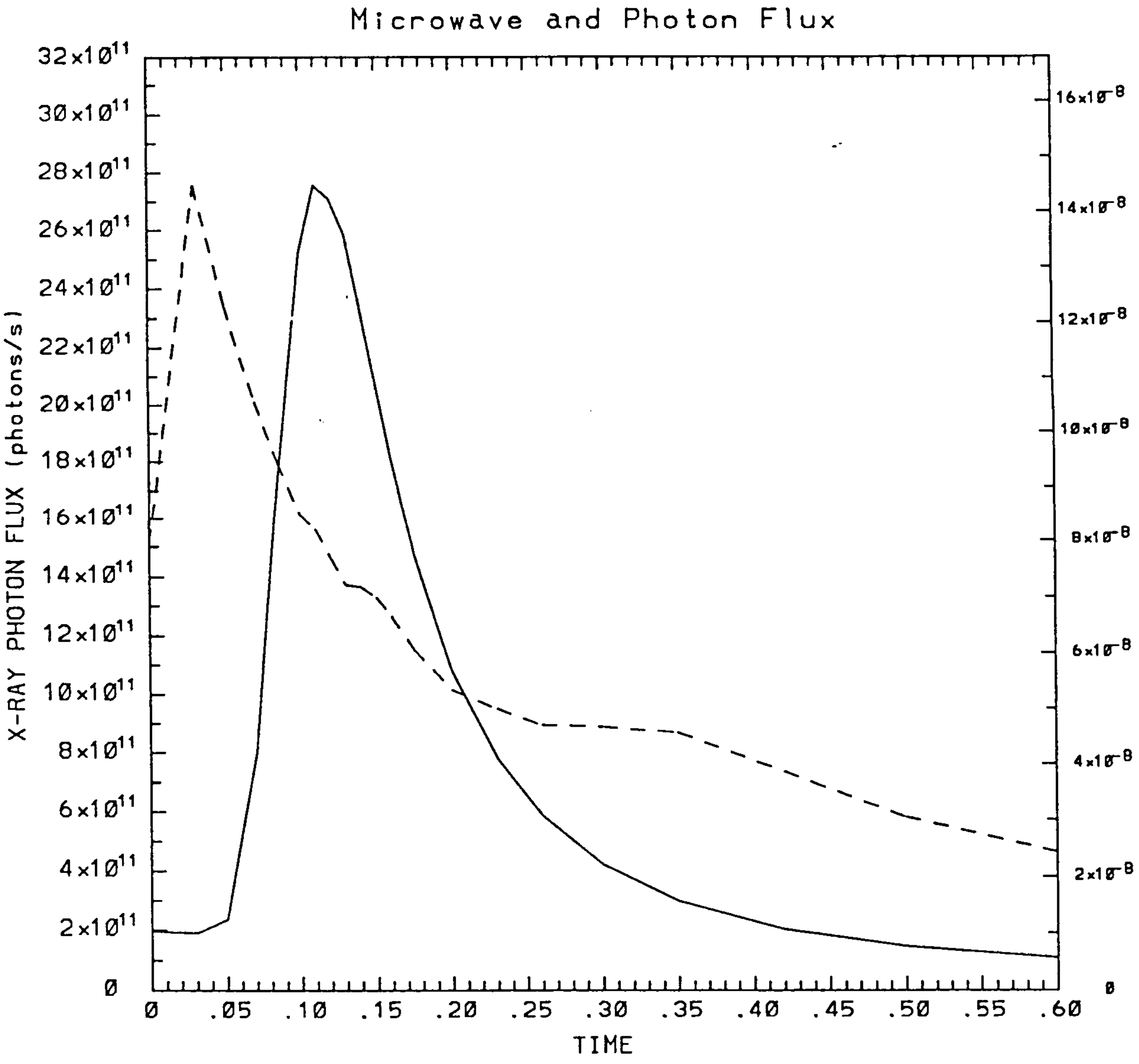
Microwave and Photon Flux
32x10^11
30x10^11
28x10^11
26x10^11
24x10^11
22x10^11
20x10^11
18x10^11
16x10^11
14x10^11
12x10^11
10x10^11
8x10^11
6x10^11
4x10^11
2x10^11
0
X-RAY PHOTON FLUX (photons/s)
16x10^-8
14x10^-8
12x10^-8
10x10^-8
8x10^-8
6x10^-8
4x10^-8
2x10^-8
0
MICROWAVE FLUX (ergs/s/Hz)
0
.05
.10
.15
.20
.25
.30
.35
.40
.45
.50
.55
.60
TIME

Figure 6.2.4

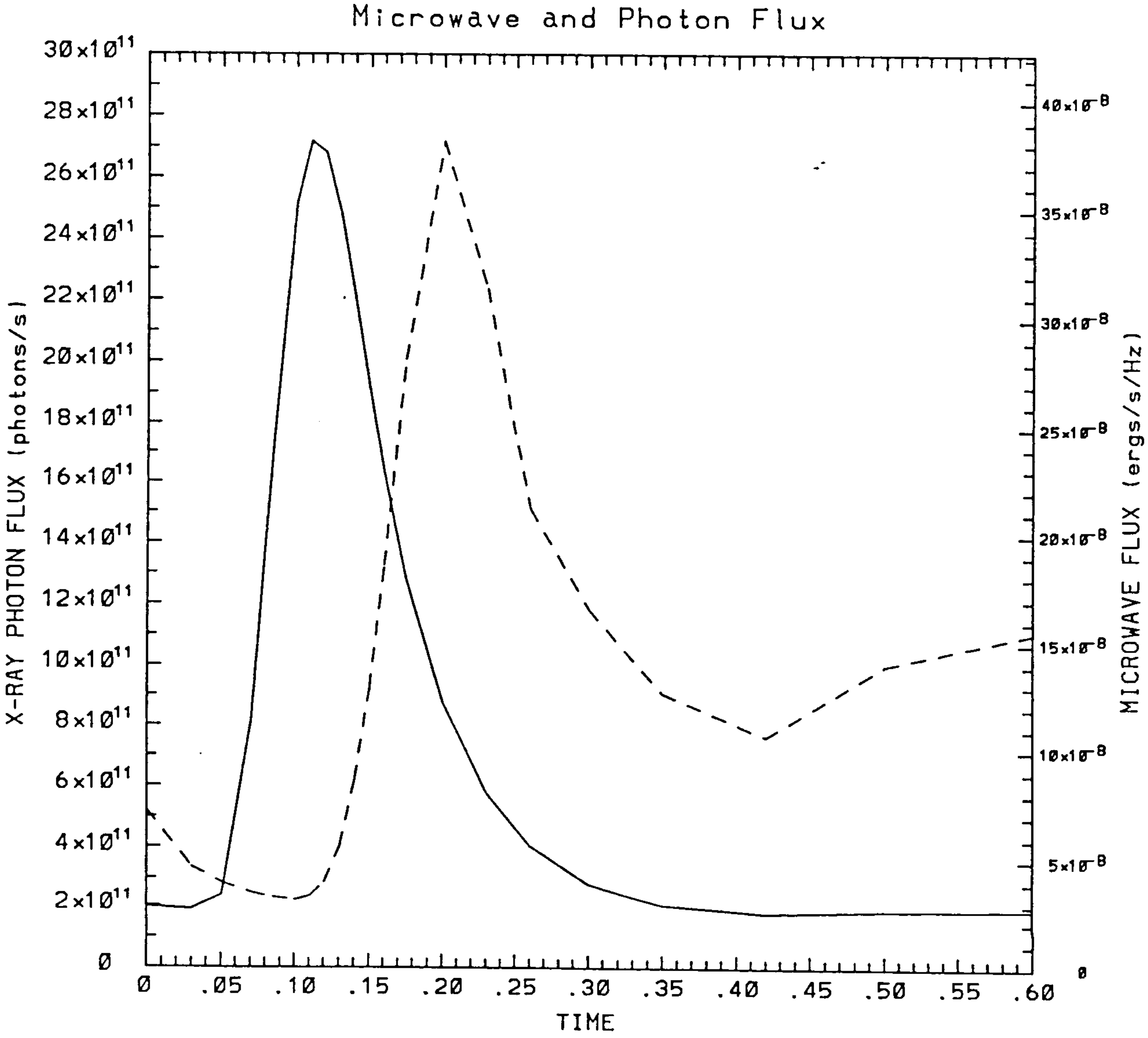
Microwave and Photon Flux
30x10^11
28x10^11
26x10^11
24x10^11
22x10^11
20x10^11
18x10^11
16x10^11
14x10^11
12x10^11
10x10^11
8x10^11
6x10^11
4x10^11
2x10^11
0
X-RAY PHOTON FLUX (photons/s)
0
.05
.10
.15
.20
.25
.30
.35
.40
.45
.50
.55
.60
TIME
40x10^-8
35x10^-8
30x10^-8
25x10^-8
20x10^-8
15x10^-8
10x10^-8
5x10^-8
0
MICROWAVE FLUX (ergs/s/Hz)

Figure 6.2.5

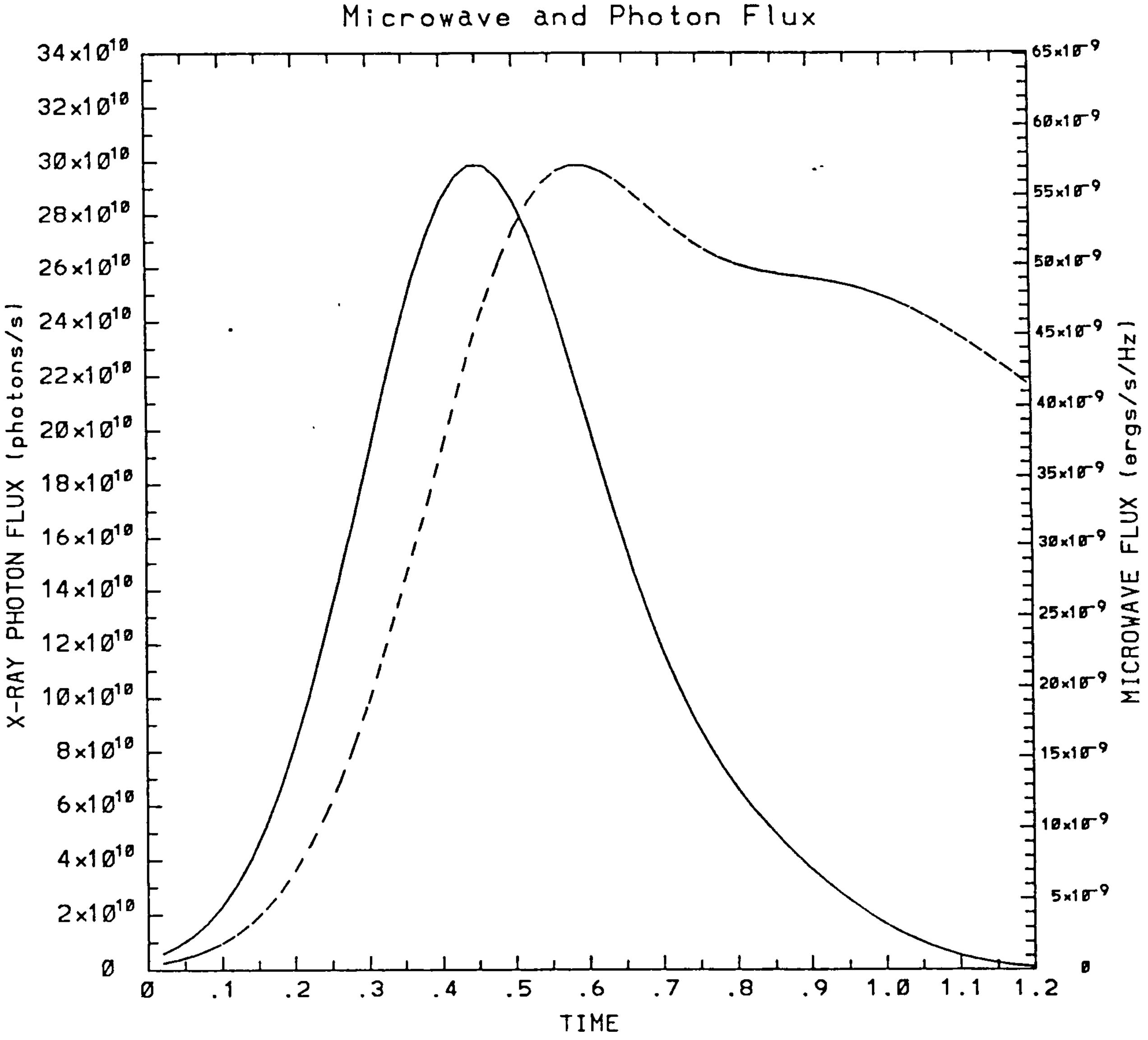

Microwave and Photon Flux
X-RAY PHOTON FLUX (photons/s)
34x10^10
32x10^10
30x10^10
28x10^10
26x10^10
24x10^10
22x10^10
20x10^10
18x10^10
16x10^10
14x10^10
12x10^10
10x10^10
8x10^10
6x10^10
4x10^10
2x10^10
0
MICROWAVE FLUX (ergs/s/Hz)
65x10^-9
60x10^-9
55x10^-9
50x10^-9
45x10^-9
40x10^-9
35x10^-9
30x10^-9
25x10^-9
20x10^-9
15x10^-9
10x10^-9
5x10^-9
0
0
.1
.2
.3
.4
.5
.6
.7
.8
.9
1.0
1.1
1.2
TIME

Figure 6.2.6

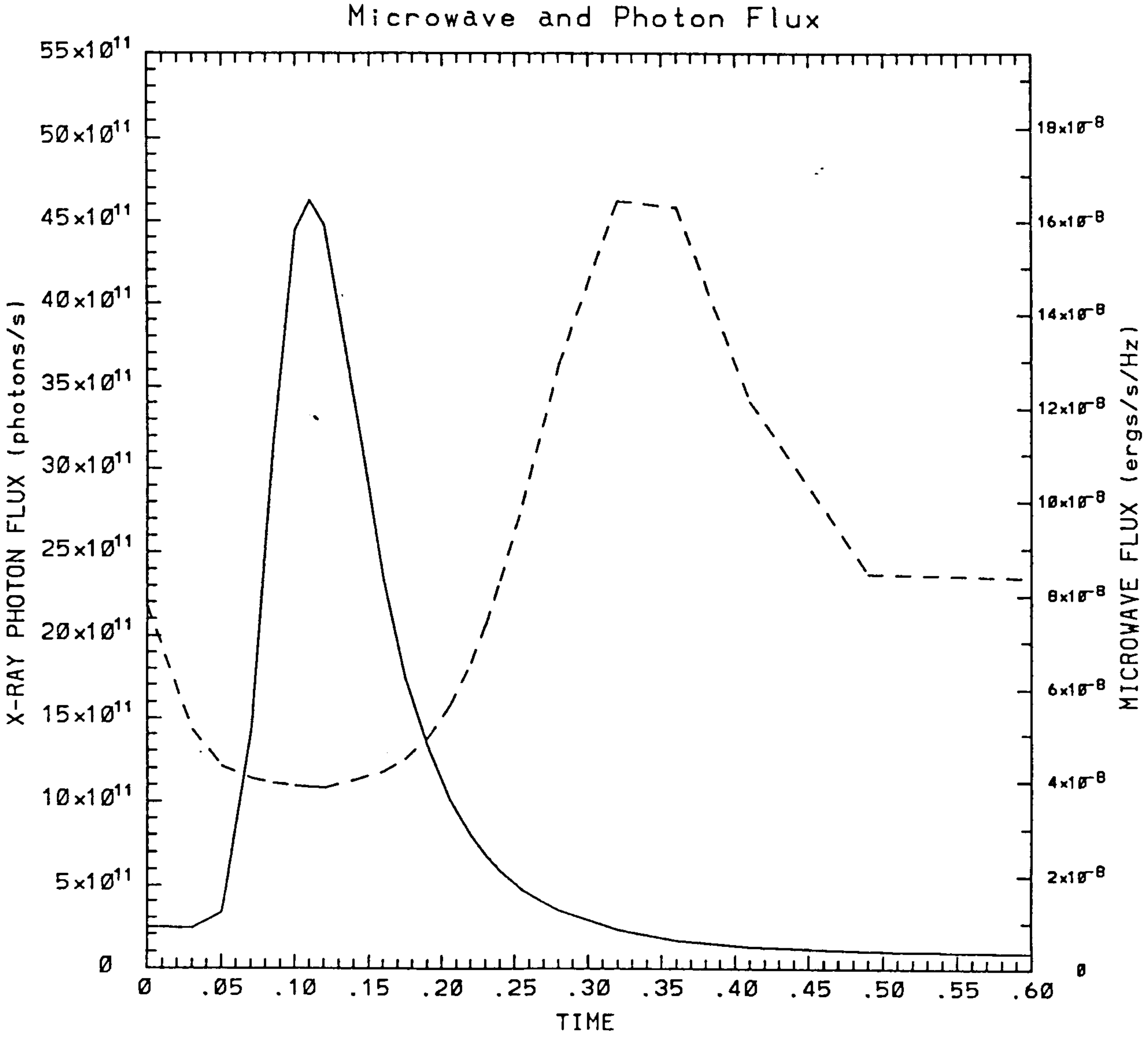

Microwave and Photon Flux
X-RAY PHOTON FLUX (photons/s)
55x10^11
50x10^11
45x10^11
40x10^11
35x10^11
30x10^11
25x10^11
20x10^11
15x10^11
10x10^11
5x10^11
0
MICROWAVE FLUX (ergs/s/Hz)
18x10^-8
16x10^-8
14x10^-8
12x10^-8
10x10^-8
8x10^-8
6x10^-8
4x10^-8
2x10^-8
0
0
.05
.10
.15
.20
.25
.30
.35
.40
.45
.50
.55
.60
TIME

Figure 6.2.7

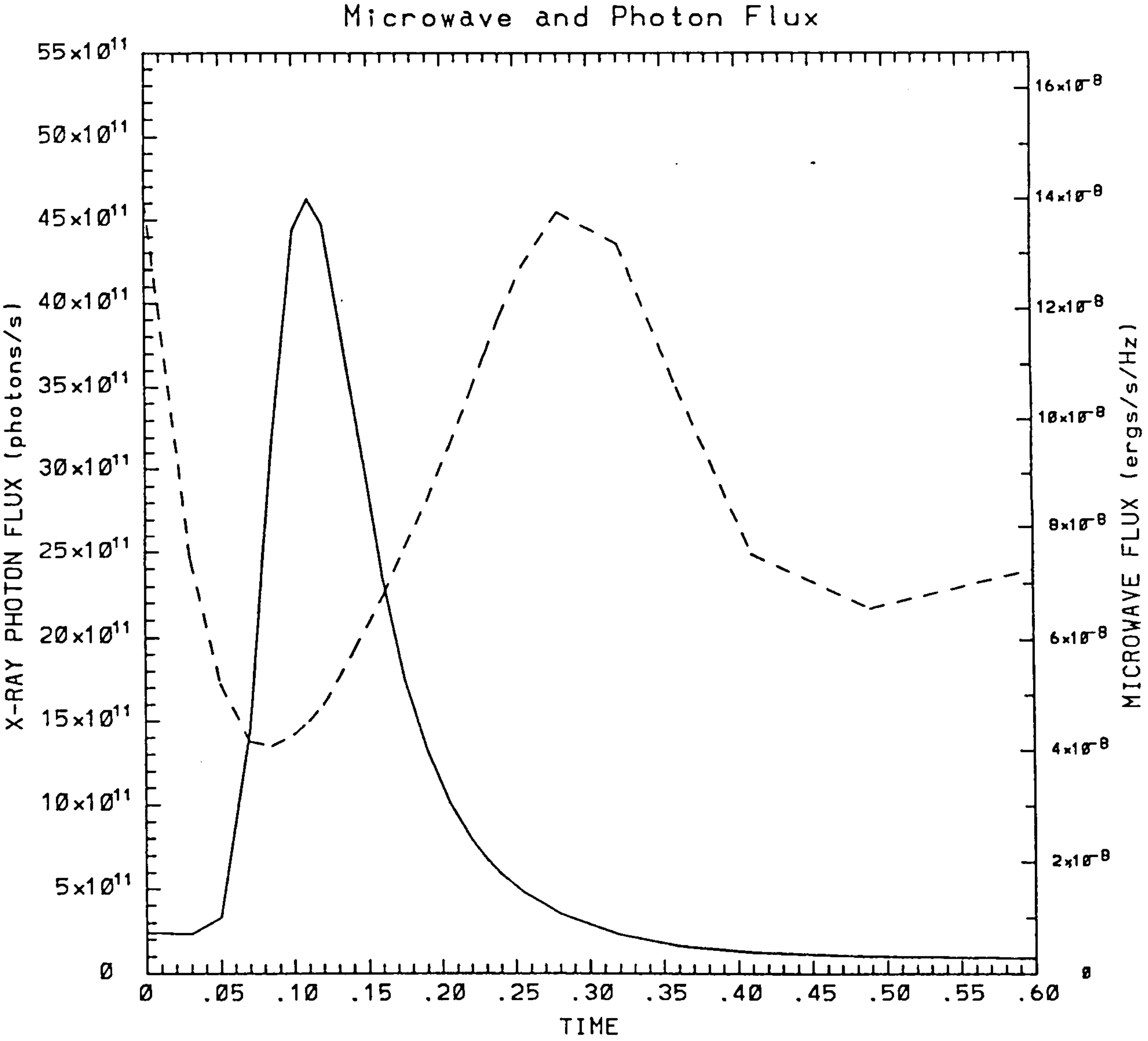
Microwave and Photon Flux
X-RAY PHOTON FLUX (photons/s)
55x10^11
50x10^11
45x10^11
40x10^11
35x10^11
30x10^11
25x10^11
20x10^11
15x10^11
10x10^11
5x10^11
0
MICROWAVE FLUX (ergs/s/Hz)
16x10^-8
14x10^-8
12x10^-8
10x10^-8
8x10^-8
6x10^-8
4x10^-8
2x10^-8
0
0
.05
.10
.15
.20
.25
.30
.35
.40
.45
.50
.55
.60
TIME

Figure 6.2.8

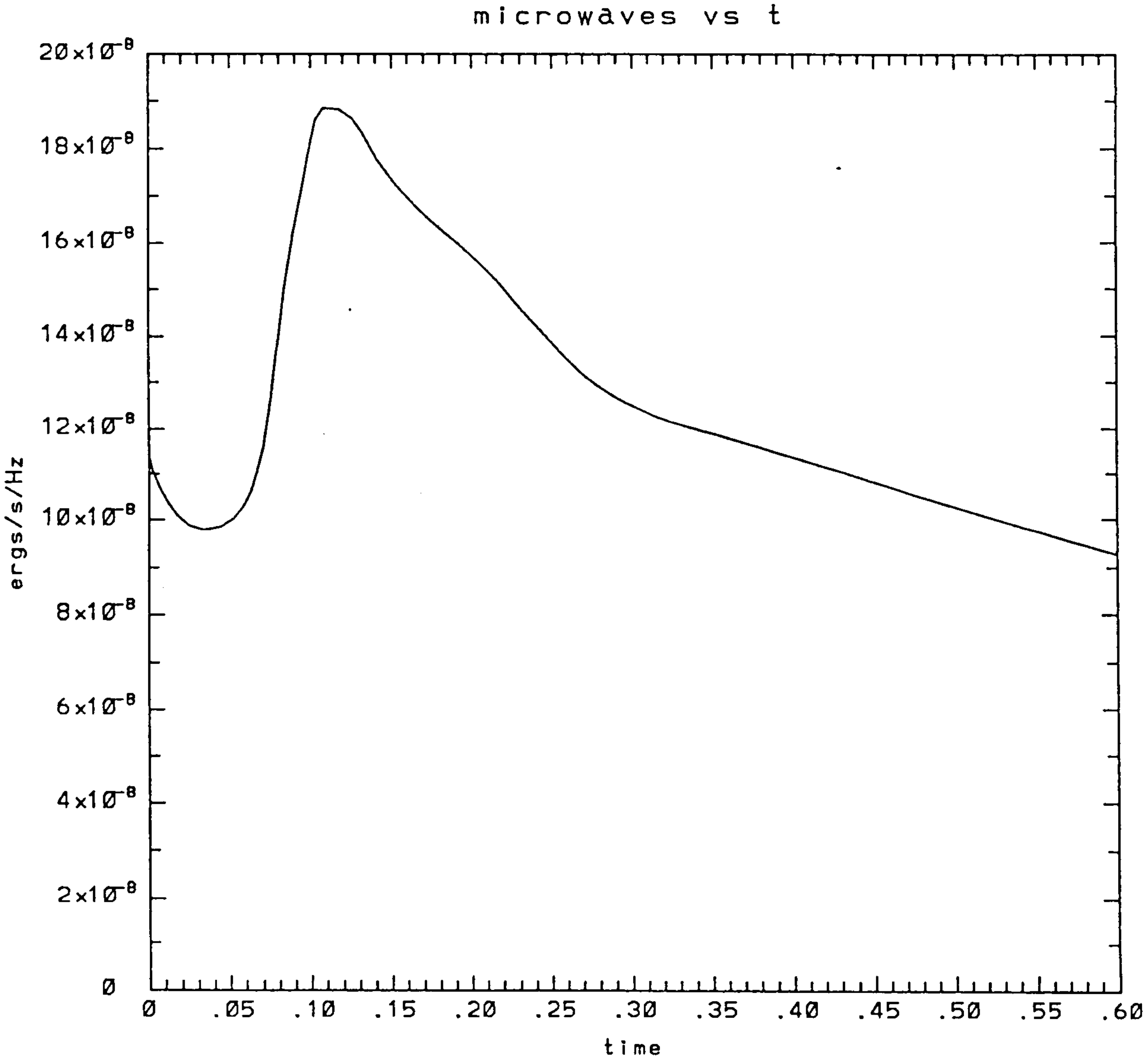
microwaves vs t
ergs/s/Hz
20x10^-8
18x10^-8
16x10^-8
14x10^-8
12x10^-8
10x10^-8
8x10^-8
6x10^-8
4x10^-8
2x10^-8
0
0
.05
.10
.15
.20
.25
.30
.35
.40
.45
.50
.55
.60
time

Figure 6.2.9

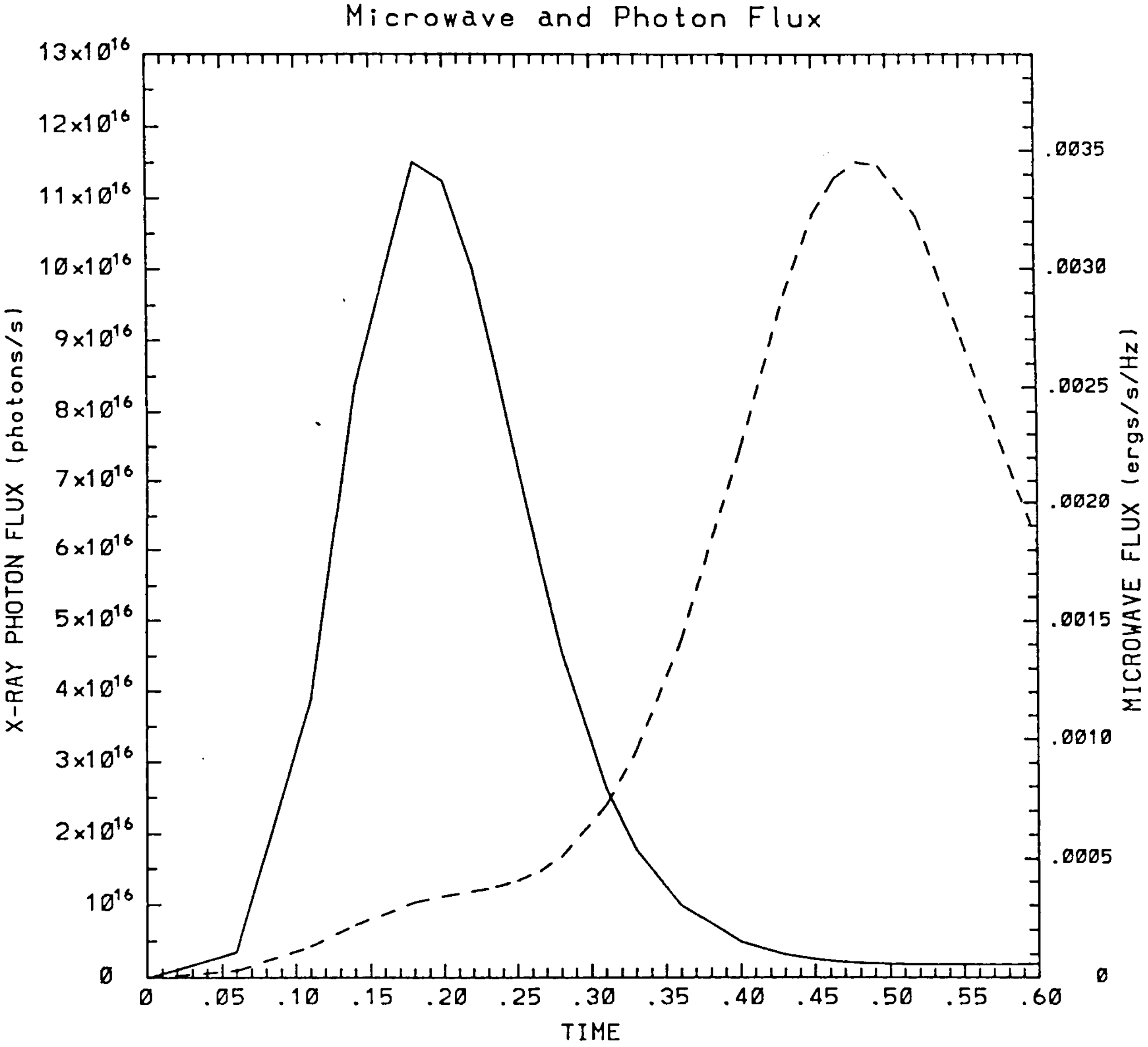
Microwave and Photon Flux
X-RAY PHOTON FLUX (photons/s)
13x10^16
12x10^16
11x10^16
10x10^16
9x10^16
8x10^16
7x10^16
6x10^16
5x10^16
4x10^16
3x10^16
2x10^16
10^16
0
MICROWAVE FLUX (ergs/s/Hz)
.0035
.0030
.0025
.0020
.0015
.0010
.0005
0
0
.05
.10
.15
.20
.25
.30
.35
.40
.45
.50
.55
.60
TIME

Figure 6.3.1

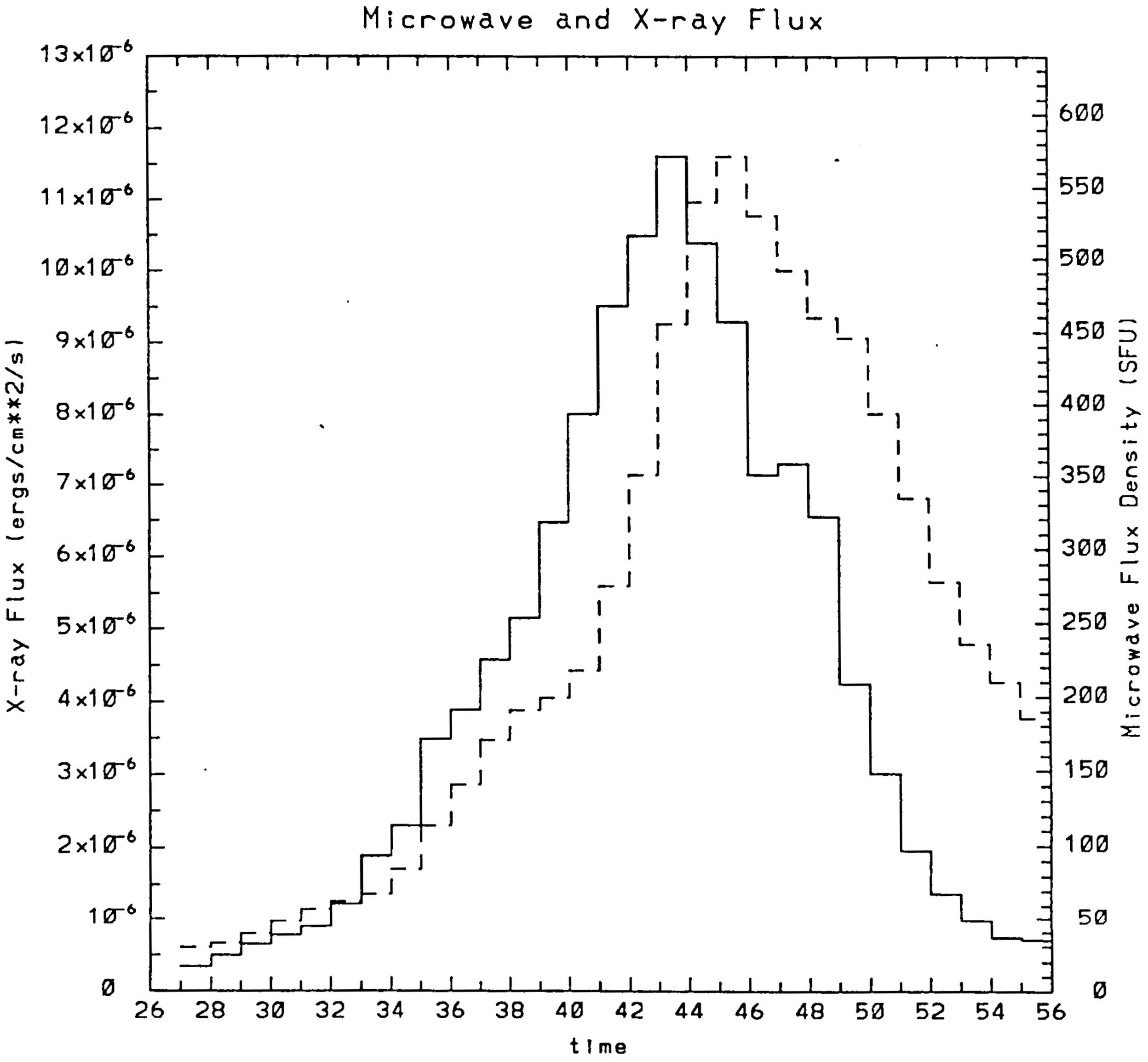
Microwave and X-ray Flux
X-ray Flux (ergs/cm**2/s)
Microwave Flux Density (SFU)
time
13×10^-6
12×10^-6
11×10^-6
10×10^-6
9×10^-6
8×10^-6
7×10^-6
6×10^-6
5×10^-6
4×10^-6
3×10^-6
2×10^-6
10^-6
0
600
550
500
450
400
350
300
250
200
150
100
50
0
26
28
30
32
34
36
38
40
42
44
46
48
50
52
54
56

Figure 6.3.2

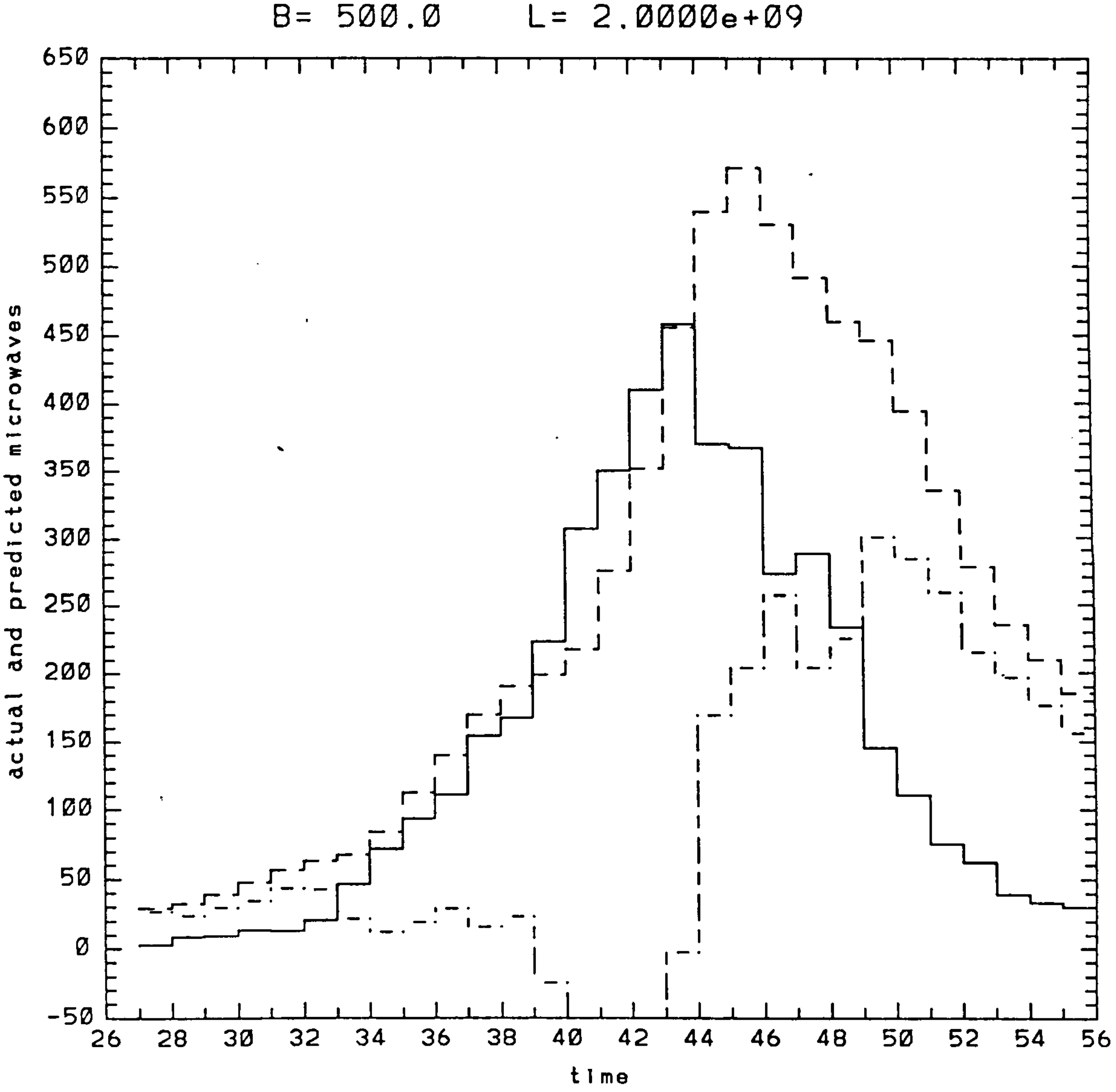
B= 500.0 L= 2.0000e+09
actual and predicted microwaves
650
600
550
500
450
400
350
300
250
200
150
100
50
0
-50
26
28
30
32
34
36
38
40
42
44
46
48
50
52
54
56
time

Figure C.3.3

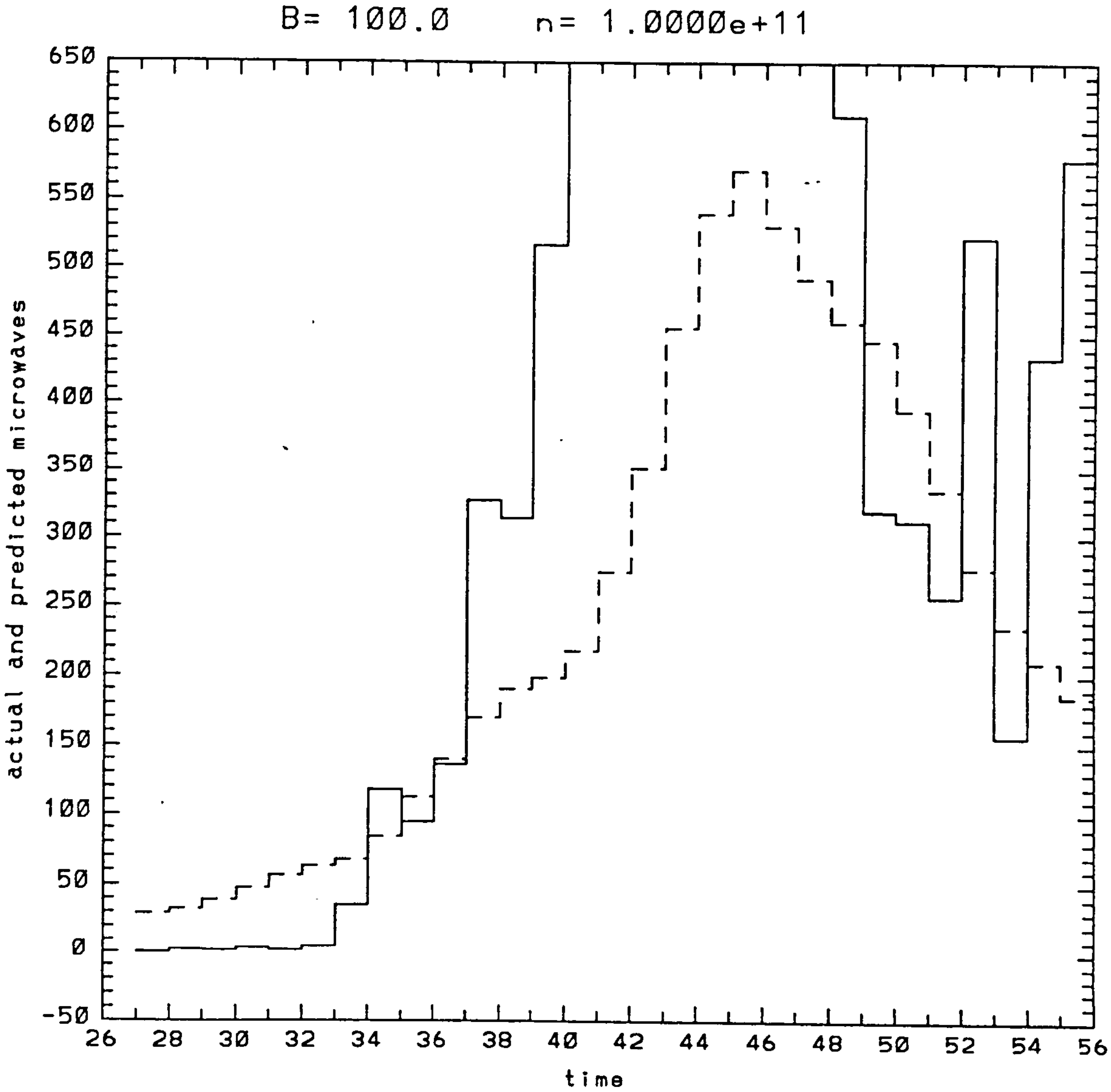
B= 100.0 n= 1.0000e+11
actual and predicted microwaves
650
600
550
500
450
400
350
300
250
200
150
100
50
0
-50
26
28
30
32
34
36
38
40
42
44
46
48
50
52
54
56
time

CHAPTER 7. THE FINAL CHAPTER - A SUMMARY

Since many astrophysical objects emit radiation with rapid time variation, we set out to analyze the time dependence of the emission from astrophysical plasmas. To do this, we analyzed the evolution of energetic particle distributions in magnetized plasmas and the time dependence of the resulting radiation. We then applied these results to the study of the time dependence of the microwave and hard X-ray emission from solar flares. For studying the emission on short timescales of the order of the particle propagation and collision times, we made use of the time dependent Fokker-Planck equation including magnetic mirroring and Coulomb collisions to calculate the evolution of accelerated electron distributions. However, on longer timescales, we developed relations for the steady state ratio of microwaves to X-rays for nonthermal thin and thick target, and multithermal solar flare models. We have found that it is possible to explain many of the observations of solar flares in the context of the simple nonthermal thick target model.

For a homogeneous plasma we have found an exact analytic solution to the time dependent Fokker-Planck equation describing the evolution of the distribution of particles in energy and pitch angles (with respect to the magnetic field). For an inhomogenous plasma, analytic solutions are possible only for particles with small pitch angles (namely, beams collimated along the field lines). We then compared the bremsstrahlung x-ray spectrum from a short burst of accelerated electrons with the high temporal resolution hard x-ray solar flare spectra observed by HXRBS on SMM.

The observed softening with time of the x-ray spectra rules out the homogeneous solution, which means that electrons do not lose most of their energy in the uniform density coronal portion of the flaring loop. Most of the x-ray emission then occurs at the base of the loop below the transition region. Consequently, the decay time and the degree of spectral softening are primarily determined by the spread in arrival time of the electron beam at the base of the loop. The more the particles are spaced out when they reach the transition region, the longer the burst decay time; and the greater the spread in arrival times between high and low energy particles, the higher the degree of spectral softening. The particles are spread out by a combination of the time of flight difference from the acceleration region to the chromosphere, and the initial injection time width. The pitch angle, the energy, and the distance from the acceleration region to the transition region determine the time of flight to the transition region. Since the effect of collisions in the corona is small, the time of flight over the distance s_t is $s_t/c\beta\mu$. The difference in time of flight between electrons of different energies is therefore proportional to s_t. Thus, smaller s_t leads to less spectral softening . Therefore, injection of the accelerated particles near or below the transition region is ruled out for such bursts.

Furthermore, the larger the range of pitch angles, the smaller the injection time t_0 has to be in order to reproduce the observations. The small pitch angle assumption basically amounts to ignoring the difference in path length between particles of different pitch angles. Thus the time of flight difference from the acceleration region to the thick target is determined solely by the difference in particle energies. This is why our assumption of small pitch angle requires that the injection time t_0 be greater than .1 s. Otherwise, the decay of the burst would be too short. We have found that under the assumption that the pitch angles are small and that the injection distribution is seperable in time and energy, the flare parameters must satisfy the constraints given in Table 3.1.

In order to analyze the effects of converging magnetic field, spatial inhomogeneities, and large pitch angles, together with Russell Hamilton, we developed a numerical code to solve the Fokker-Planck equation. We have given the form of the equation including magnetic mirroring, Coulomb collisions, synchrotron losses, Alfvén waves, Langmuir turbulence, and direct electric fields. The code which we have written only includes the terms in the equation due to magnetic mirroring, and Coulomb collisions. However, the numerical method of solution easily allows these other terms to be added, and we have outlined the method for doing so. This code has other possible astrophysical applications besides just solar flares, especially since it can be expanded to include other processes such as scattering by plasma waves and synchrotron losses. Some of these areas include stochastic particle acceleration by waves and generation of kinetic instabilities.

We next turned our attention to the relationship between X-ray and microwave emission from flares. Over timescales longer than the particle propagation and collisional times, steady state relations are applicable. We derived analytic relations for the ratio of microwave to X-ray flux from thin target, thick target, and multithermal solar flare models, and used these to show that the peak X-ray and microwave fluxes were most consistent with the thick target model. In these models, most of the microwaves are produced in the loop while most of the X-rays are produced at the footpoints. In the thin target model, the X-rays and microwaves are produced in the same physical region, while in the multithermal model the emission is produced by a multitemperature thermal plasma.

We analyzed a sample of 51 flares with observations in both hard X-rays and microwaves for which the X-ray spectral index is known. These data are summarized in Table 5.1. We define the dimensionless ratio of microwave to X-ray flux R, and plot R evaluated at peak emission for these flares versus the spectral index γ, and compared these to the expected R for the thick target, thin target, and multithermal models (see figures 5.2, 5.3, and 5.4).

We find that the observed microwave to X-ray ratios are consistent with a single population of electrons producing both emissions. The thick target model with a reasonable set of flare parameters ($350\,\mathrm{G} \lesssim \mathrm{B} \lesssim 650\,\mathrm{G}$ and $L \approx 2 \times 10^9\,\mathrm{cm}$) explains the data quite well. The thin target and thermal models, however, have more difficulty in explaining the observations. They both predicted a far too large value of R for reasonable values of magnetic field strength and density. The fact that previous authors had assumed a thin target geometry was the origin of the controversy surrounding whether a single power law population of nonthermal electrons could be responsible for both microwaves and X-rays.

Finally, we investigated the relative timing of the microwave and X-ray emission from flares. Using the Fokker-Planck code, we show that it is unlikely that the observed delay of microwaves behind X-rays in flares with subsecond time structure is completely caused by magnetic trapping. Rather, the higher energy electrons responsible for most of the microwaves must be accelerated slightly later than the lower energy electrons responsible for most of the X-rays. We also showed that the microwaves and X-rays during the rising phase of longer flares matched very well the predictions of the thick target model. However, the observed delay of the microwave peak can be interpreted as being due to another component of the microwave emission which peaks during the decay phase of the flare. Again, this could be explained by later acceleration of higher energy electrons together with magnetic trapping in the corona. Further study along these lines await better time resolution spectral and imaging observations in both microwaves and X-rays.

References

Bai, T. 1982, *Ap. J.*, **259**, 341.

Bai, T. and Ramaty, R., 1978, *Ap. J.*, **219**, 705.

Bekefi, G. 1966, *Radiation Processes in Plasmas*, (New York: Wiley).

Blumenthal, G.R., and Gould, R.J. 1970, *Rev. Mod. Phys.*, **42**, 237.

Brown, J.C., 1971, *Solar Phys.*, **18**, 489.

Brown, J.C., 1973, *Solar Phys.*, **31**, 143.

Brown, J.C., 1974, *IAU symposium 57, Coronal Disturbances*, ed. G.A. Newkirk (Dordrecht: Reidel), p. 395.

Centrella, J., and Wilson, J.R. 1984, *Ap. J. Suppl.*, **54**, 229.

Cornell, M., Hurford, G., Kiplinger, A., Dennis, B. 1984, *Ap.J.*, **279**, 875.

Dennis, B.R. 1988, *Solar Phys.*, **118**, 49.

Dennis, B.R., Orwig, L.E., Kiplinger, A.L., Gibson, B.R., Kennard, G.S., and Tolbert, A.K. 1985, *The Hard X-ray Burst Spectrometer Event Listing 1980 - 1985*, Technical Memorandum 86236, GSFC.

Dulk, G. and Dennis, B. 1982, *Ap.J.*, **260**, 875.

Dulk, G. and Marsh, K. 1982, *Ap.J.*, **259**, 350.

Emslie, A.G., 1983, *Ap. J.*, **271**, 367.

Gary, D. 1985, *Ap.J.*, **297**, 799.

Gary, D. and Tang, F. 1984, *Ap.J.*, **288**, 385.

Harding, A.K., Petrosian, V., and Teegarden, B.J. 1986, in E.P. Liang and V. Petrosian (eds.), *Gamma-Ray Bursts, AIP Conference Proceedings 141*, p. 75.

Holt, S. and Ramaty, R. 1969. *Solar Phys.*, **8**, 119.

Hawley, J.F., Smarr, L.L., and Wilson, J.R. 1984, *Ap. J. Suppl.*, **55**, 211.

Kai K. 1986, *Solar Phys.*, **104**, 235.

Kai, K., Kosugi, T., and Nitta, N. 1984, *Publ. Astron. Soc. Japan*, **37**, 155.

Kane, S.R. and Anderson, K.A., 1970, *Ap. J.*, **162**, 1003.

Kaufmann, P., Strauss, F.M., Costa, J.E.R., Dennis, B.R., Kiplilnger, A., Frost, K.J., and Orwig, L.E. 1983, *Solar Phys.*, **84**, 311.

Kiplinger, A.L., Dennis, B.R., Emslie, A.G., Frost, K.J. and Orwig, L.E., 1983, *Ap. J. Letters*, **265**, L99.

Kiplinger, A.L., Dennis, B.R., Frost, K.J. and Orwig, K.J., 1984, *Ap. J. Letters*, **287**, L105.

Kosugi, T. and Shiomi, Y. 1983, *Solar Radio Activities Recorded by the Nobeyama Solar Radio observatory in 1978 - 1982*, (Nagano, Japan).

Lifshitz,E.M. and Pitaevskii, L.P. 1981, *Physical Kinetics*, (Oxford, Pergamon), chapter 2.

Lin, R.P. and Hudson, H.S. 1976, *Solar Phys.*, **50**, 153.

Lin, R.P., Schwartz, R.A., Pelling, R.M., and Hurley, K.C. 1981, *Ap. J.*, **251**, L109.

Langer, S.H. and Petrosian, V., 1977, *Ap. J.*, **215**, 666.

Leach, J., 1984, Ph.D. Thesis, Stanford University.

Leach, J. and Petrosian, V. 1981, *Ap.J.*, **251**, 781.

Lu, E. and Petrosian, V. 1988, *Ap.J.*, **327**, 405.

Lu, E.T., and Petrosian, V. 1989, *Ap. J.*, **338**, 1122.

McTiernan, J.M. and Petrosian, V., 1989, in preparation, Stanford University, Stanford.

Melrose, D.B. 1980, *Plasma Astrophysics: Nonthermal Processes in Diffuse Magnetized Plasmas, Vol. 1*, (New York, Gordon and Breach)

Nitta, N., Kiplinger, A.L., and Kai, K. 1989, *Ap. J.*, **337**, 1003.

Peterson, L. and Winckler J. 1959, *J.G.R.*, **64**, 697.

Petrosian V. 1973, *Ap.J.*, **186**, 291.

Petrosian V. 1981, *Ap.J.*, **251**, 727.

Petrosian, V. 1985, *Ap. J.*, **299**, 987.

Press, W.H., Flannery, B.P., Teukolsky, S.A., and Vetterling, W.T. 1986, *Numerical Recipes, The Art of Scientific Computing*, (New York, Cambridge University Press).

Schlickeiser, R. 1989a, *Ap. J.*, **336**, 243.

Schlickeiser, R. 1989b, *Ap. J.*, **336**, 264.

Schmahl, E., Kundu, M., and Dennis, B. 1985, *Ap.J.*, **299**, 1017.

Smith, G.D. 1978, *Numerical Solution of Partial Differential Equations*, (Oxford: Clarendon Press).

Starr, R., Heindl, W.A., Crannel, C.J., Thomas, R.J., Batchelor, D.A., and Magun, A., 1988, *Ap. J.*, **329**, 967.

Takakura, T. and Kai, K. 1966, *Publ. Astron. Soc. Japan*, **18**, 57.

Vestrand, W.T., Forrest, D.J., Chupp, E.L., Rieger, E., and Share, G.H., 1987, *Ap.J.*, **322**, 1010.